Exciton Dynamics in Organic Semiconducting Materials

A DISSERTATION

SUBMITTED TO THE FACULTY OF THE GRADUATE SCHOOL

OF THE UNIVERSITY OF MINNESOTA

BY

Philip Craig Goff

IN PARTIAL FULFILLMENT OF THE REQUIREMENTS

FOR THE DEGREE OF

Doctor of Philosophy

David A. Blank

April, 2017

Acknowledgements

There are far too many people to count to thank for their contributions to my graduate career. To my friends and family, thank you for your continuous support throughout this time.

I would like to specifically thank my collaborators who helped make the work in this thesis possible. Joshua Speros, of the Hillmyer group, for synthesizing the statistical copolymers studied in Chapter 3. From the Chemical Engineering Department, I would like to thank Ian Curtin and Matt Menke from the Holmes group for preparing the mixed subphthalocyanine and subnaphthalocyanine thin films studied in Chapters 4 and 5. Finally, I would like to thank the many members of the research group of Victor Nemykin for synthesizing the various BODIPY derivatives studied in Chapter 6.

I also want to thank all of my fellow Blank Group members, past and present, including Jon Hinke, Benj Fitzpatrick, Toni Sanchez-Diaz, Eric Nordland, Erin Mulholand, Yefeng Wang, Richard Okeke, Francesc Domenesch, Andy Healy, and Rachel Swedin. To Emily Pelton, thank you for our many coffee breaks and conversations about TAs and general

chemistry students, as well as all your help troubleshooting the glovebox and helping it to stay oxygen-free. I'd like to thank our former undergraduate, Matthew Hauwiller, not only for his help on the statistical copolymer project in Chapter 3, but for being a good spot about the group's teasing of him. I want to thank Ben Caplins for all of the stimulating intellectual discussions we had, as well as his help maintaining and improving the laser. Meghan Knudtzon, thank you for being a true friend and making my last few years of graduate school the most enjoyable.

A special thanks needs to be given to Tom Pundsack, whose encouragement was responsible for getting me through some of the lower points in my graduate career. You were a role model for me throughout my time in graduate school, and I will be forever grateful for all your help and support.

Finally, I want to acknowledge my advisor David Blank, without whom none of this would have been possible. Thank you David for all your support, your always open door, and your incredible patience. You were an amazing teacher, and I am incredibly grateful for the opportunity to have worked with you these past years.

Abstract

World energy consumption is projected to rise dramatically over the next three decades. Presently, over 80% of worldwide energy consumption is derived from nonrenewable sources. In order to meet these demands, increased utilization of solar energy will be required. Organic semiconducting materials are an attractive alternative to the traditional crystalline silicon devices which at present dominate the photovoltaic market. They possess a number of material and physical processes which may ultimately prove for photogeneration of electricity at a cost competitive with conventional nonrenewable fuel sources. However, the power conversion efficiencies of these devices at present limits their widespread adoption. In order to improve their efficiencies, it is important to understand the relationship between chemical and physical characteristics of the molcules with the exhibited excited state photophysics. In this dissertation, the excited state properties of various organic semiconducting materials, such as polymers and small molecules, will be examined.

First, in Chapter 3 a series of statistical donor/acceptor copolymers were generated where the monomer unit composition was tuned in order to adjust the absorption properties of the polymer. Ultrafast pump-probe spectroscopy was employed to characterize the effect that changing polymer composition has on the exciton lifetime within these materials. It was found that by tuning the composition of the monomer units, the lifetime could be extended nearly 30 times over that of either neat donor or neat acceptor monomer units.

Moreover, the lifetime reached a maximum at a ratio of approximately 1:4 donor to acceptor monomer units, suggesting that fine-tuning the ratio of the two may provide enhancements in OPV performance.

In Chapters 4 and 5, ultrafast pump-probe spectroscopy was used to characterize exciton transport in thin films of Subphthalocyanine and Subnaphthalocyanine. Adjusting the film composition was found to have a substantial influence on the exciton diffusion length in the films. Importantly, exciton-annihilation induced heating of the films resulted in the manifestation of thermal signatures in the transient spectra. These signatures were not previously well appreciated in literature as manifesting on a sub-nanosecond timescale, and have been potentially erroneously assigned as electronic signatures from excited state species. A method is proposed to isolate these thermal signatures from the excitonic signatures, yielding accurate exciton decay dynamics.

Finally, the excited state dynamics of a series of novel boron dipyrromethane derivatives will be investigated in Chapter 6. Particular attention will be made as to whether there is a potential for these materials to spontaneously form a spontaneously self-assembled supramolecular complex with fullerene in solution. The formation of such complexes is of considerable interest, however the results herein suggest that many of the previously reported complexes may actually be misinterpretation of photoluminescence extinguishing due to inner filter effects as opposed to quenching arising from energy and charge transfer.

Contents

List of Tables

List of Figures

List of Abbreviations

ΔOD	change in optical density
BODIPY	boron dipyrromethane
CW	continuous wave (laser)
DSSC	dye sensitized solar cell
E_g	band-gap
ESA	excited state absorption
FRET	Förster resonance energy transfer
FWHM	full width at half maximum
GSB	ground state bleach
GSH	ground state hole
HOMO	highest occupied molecular orbital
LED	light emitting diode
LUMO	lowest unoccupied molecular orbital
NOPA	noncollinear optical parametric amplifier (amplification)
OLED	organic light emitting diode
OPV	organic photovoltaic (device)
P3HT	poly(3-hexylthiophene)
PTV	poly(thienylene-vinylene)
PL	photoluminescence
PMT	photomultiplier tube
PV	photovoltaic (device)
QY	quantum yield (fluorescence)
regen	regenerative amplifier

SE	stimulated emission
SHG	second harmonic generation
SubNc	Subnaphthalocyanine
SubPc	Subphthalocyanine
TBTV	thiophene benzothiadiazone thienylene vinylene
TCSPC	time correlated single photon counting
Ti:Sapph	titanium sapphire (crystal)

Chapter 1

Introduction

1.1 Energy Outlook

Meeting ever-increasing energy demands remains one of the most pressing issues facing society today. In 2012, the world consumed over 548 quadrillion Btu of energy (equivalent to a rate of 18.3 TW), an amount which is projected to rise 48% by 2040 to over 815 quadrillion Btu (a rate of 27.5 TW). More than 80% of this rise in energy demand will occur in non-OECD nations (nations which are outside of the Organization for Economic Cooperation and Development), including countries such as China and India. At present, over 80% of energy produced worldwide originates from nonrenewable sources, a trend also observed in energy consumption the United States (Figure 1.1). A 2009 report projected depletion of oil and natural gas reserves by 2042.[1] Developing new renewable energy sources in the face of diminishing fossil fuel reserves is therefore imperative in both minimizing

geopolitical tensions as well as reducing economic strain associated with high energy costs. Petroleum is also a necessary reagent in the manufacture of many plastics, chemicals, and pharmaceuticals; its preservation for these uses is also critical.

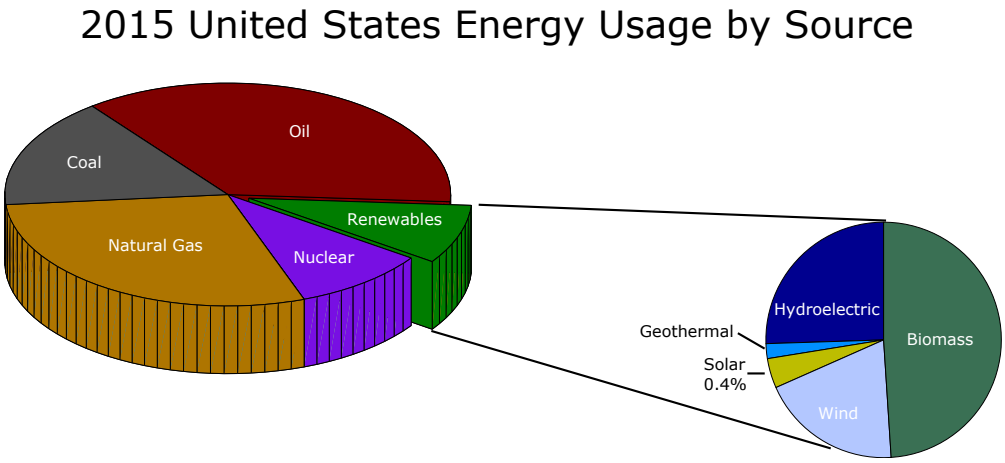

Figure 1.1: United States energy use by source for 2015 (left). Breakdown of 'Renewables' category (right). Data obtained from the U.S. Energy Information Administration September 2016 Monthly Energy Review.[2]

The feasibility of several non-carbon based primary energy sources to meet increased energy demand is first examined in order to understand the energy landscape, and place solar energy in the appropriate context.

Hydroelectric: Within OECD countries, the potential for expansion of hydroelectric

energy generation is low, as many of the exploitable resources have already been developed.[3] The maximum amount of technically and economically feasible global hydroelectric power totals about 0.9 TW, of which at least 0.6 TW has already been captured. Hydroelectric capacity thus possesses limited potential for meeting these needs via further resource exploitation.[4]

Geothermal: The estimated heat flux from the earth's interior integrated over the entire surface is 44 TW, a rate several times greater than the rate required to meet all of our energy needs.[5] It is debated precisely how much energy could feasibly be extracted from geothermal sources; however, most reasonable upper bounds on the rate being on the order of 1 TW or less, far less than what is necessary to meet human energy consumption.[4,6]

Biomass: Biomass has been toted as a potentially carbon-neutral energy source, however it faces key efficiency problems. Plants capture less than 1% of incident solar energy, and as a result over 30% of the world's total land would need to be converted solely to biomass production in order to meet all energy demands, a solution which is both theoretically and practically unrealistic.[4]

Wind: Wind energy could meet potentially 10% of our total future energy needs if every single potential site around the world was utilized. This would also require substantial technological advancements to be made in energy storage and transportation in order to exploit sites that are at present economically and technologically unfeasible, such as offshore based installations. The overall investment costs and limited power returns make wind power impractical to meet increased energy demands.[4]

Nuclear: Nuclear fission possesses the scalability to meet all of mankind's increased energy demands. However, two factors limit the long term implementation of nuclear fission. First, the total amount of fissile terrestrial uranium will only allow for ten years of energy demand to be met. Second, over 10,000 nuclear reactors would need to be constructed in order for nuclear energy production to meet these increased demands. This averages out to approximately one new nuclear plant made fully operational every other day for the next 50 years.[4] Research into the feasibility of other fissile materials, such as plutonium or thorium, is necessary in order for long-term sustained nuclear energy production. Public concern over nuclear related environmental impacts has increased, in particular due to events such as the disaster at the Fukushima Daiichi Nuclear power plant, resulting in a slow down in the construction of new nuclear power production facilities.[3,7]

Solar modules have seen rapidly increased utilization over the past 10 years, with capacity increasing at an average yearly growth rate of 56% between 2006-2011.[8] This increased capacity stems from two main sources: a large drop in the price of photovoltaic modules as well as governmental and regulatory policies that have favored solar implementation. However, as seen in Figure 1.1, solar energy remains a small player in the energy landscape, accounting for only 0.4% of energy consumption in the United States. Solar energy underutilization becomes readily apparent when considering the scale of its potential. The sun provides the earth with energy at a rate of 120,000 TW, over 10,000 times greater than current energy needs. If all the incident solar energy for one hour could be harnessed, we could power the entire planet for a year.[4,9] Of all the renewable energy sources discussed

thus far, only solar possesses the scalability necessary to meet all of mankind's energy demands.

To achieve large scale implementation, the costs of solar energy must achieve parity with other electricity generating sources.[10] Uncertainty about the longevity of favorable governmental regulations (subsidies, etc.) has also hindered more widescale adoption of solar photovoltaics. Studies have suggested that government involvement is a key factor for recent adoption.[11] The efficiencies of these devices must be improved to a point that they will be financially competitive with carbon-based fuel sources even in the absence of favorable regulatory policies. The photovoltaic market is currently dominated by silicon based devices, with power conversion efficiencies of laboratory research cells already approaching theoretical maximum limits (33% according to the Shockley-Quiesser limit for a single p-n junction cell).[12,13] Further improvements are becoming considerably more difficult and more costly to achieve. Silicon photovoltaic modules are also still hindered by high installation and repair costs.

In the past decade, research has turned to alternative, non-silicon based, organic semiconducting materials to meet increasing energy demand.[14] Dye-sensitized cells, inorganic quantum dots, and organic cells (typically made of either organic small molecules or polymers) are made of earth-abundant materials and can potentially possess lower production costs than silicon photovoltaics.[15,16] Because many of these materials are solution processable, they can be prepared on flexible substrates, and thus achieve lower costs through cheaper manufacturing techniques such as roll-to-roll processing. Unlike traditional silicon

photovoltatics, organic materials possess semi-transparency which allows them to be easily implemented into existing spaces (such as by coatings on windows), offering them a broader range of applications.[17,18]

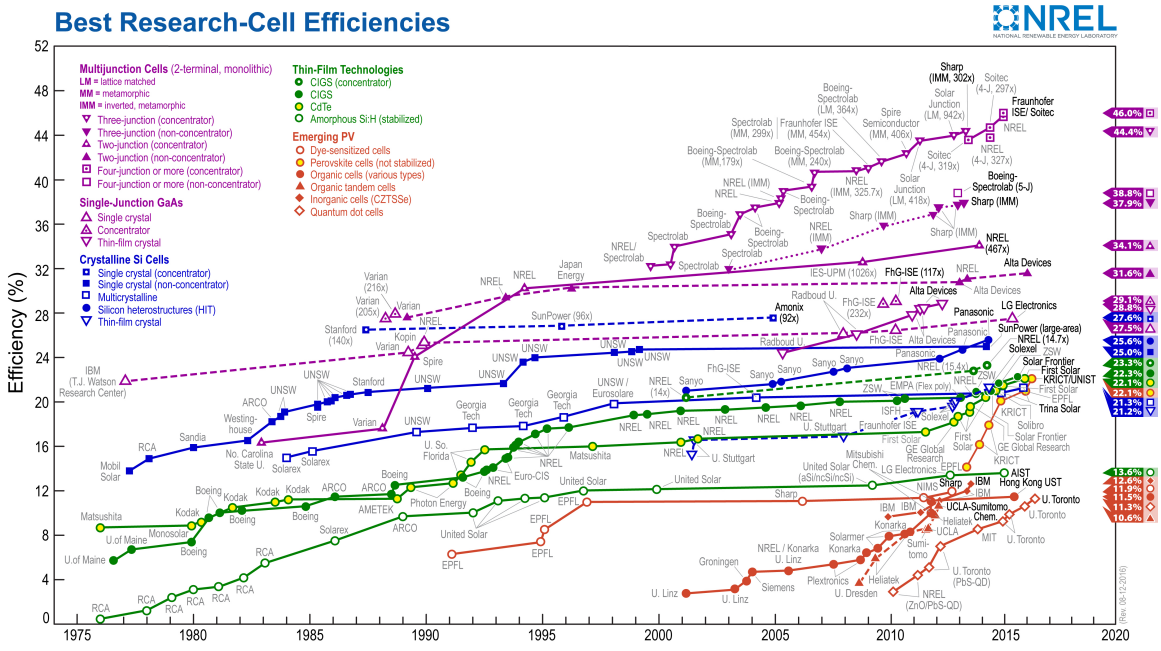

Figure 1.2: Best reported research-cell efficiencies for various photovoltaic technologies from 1976 through 2016. Figure reproduced from NREL.[12]

The implementation of organic photovoltaic (OPV) devices as commercially viable solar energy harvesters has been limited due to two primary factors. First, the power conversion efficiency of OPV devices is generally lower than silicon based devices.[19] Second, the operational lifetime of these devices is typically much shorter than silicon based devices. Each

of these issues needs to be addressed in order to achieve widespread adoption of organic photovoltaics. Recent years have seen promising improvements in reported device efficiencies (Figure 1.2). Estimates have suggested that an organic based device with a 15% power conversion efficiency and 20 year device lifetime would produce energy at a cost of roughly \$0.07-0.13 per kWh, a cost that is competitive with traditional carbon fuel sources.[15,20]

Further research into the improvement of organic photovoltaic material device efficiency is imperative for achieving cost-effective solar cells. This dissertation will focus on several different classes of organic materials, including conjugated polymers and organic small molecules. In particular, various physical factors such as molecular structure, film morphology, and composition will be studied as they relate to the fundamental physical processes of energy transfer within these materials. By elucidating these structure-function relationships, future device performance can be optimized through tailoring molecular process to exhibit desired device performance characteristics.

1.2 Solar Cell Operation

To place this work in an appropriate context, it is necessary to understand the key differences in operation between silicon based photovoltaics and photovoltaics made from alternative materials. This section will focus on the operation of both silicon and organic photovoltaic devices, as well as major sources of efficiency losses in both.

1.2.1 SiFlicon Photovoltaics

The prototypical silicon photovoltaic devices consists of single crystal silicon within which contains a p-n junction. The p-n junction is generated by atomically doping the silicon crystal with impurities. The p-type region is often obtained by doping with atoms deficient an electron in their valence shell, such as boron or indium, while the n-type region is often obtained by doping with atoms containing extra elections, such as arsenic or more typically phosphorus.[21] Near the interface between the p-type and n-type silicon, electrons in the n-type region will tend to diffuse towards the p-type region, recombining with the holes. This results in the formation of positive ions in the n-region and negatively charged ions in the p-region, effectively creating an electric field. This field suppresses further diffusion, creating a zone at the interface with no charge carriers known as the depletion region.

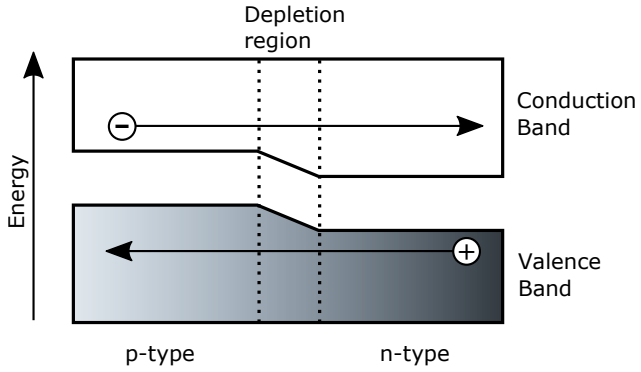

Figure 1.3: Energy diagram depicting the migration of electrons and holes within a silicon p-n junction.

When a photon impinges on the p-type region, an electron is promoted from the silicon crystal valence band to the higher lying conduction band, leaving behind a positively charged hole. In silicon, the dielectric constant is high enough to result in significant screening between the excited electron and the hole pair, generating free charge carriers. The field built into the p-n junction then causes the electron to migrate from the p-type region into the n-type region. Free electrons in the n-type region and holes in the p-type region are collected at the electrodes, which generates a current capable of driving an external load.

The Shockley-Quiesser limit is a detailed balance upper bound for the maximum power conversion efficiency of a single p-n junction silicon photovoltaic device.[13] There are three main sources of loss which contribute to the Shockley-Quiesser limit: spectral losses, blackbody radiation, and recombination.[22]

Spectral losses account for the majority of efficiency loss in photovoltaic devices. Materials can only absorb certain frequencies of light. Photons that possess energies less than the difference between the conduction band and the valence band (referred to as the band-gap) will not be absorbed. Furthermore, if a photon is absorbed possessing energy greater than the band-gap the excess energy will be lost as heat as the electron relaxes within the vibrational levels of the excited electronic state. Blackbody radiation is the baseline energy which is constantly emitted from the photovoltaic material and another source of energy loss.[22] Combined, these two sources of loss would limit a silicon device to a 44% efficiency.[13] A final major source of efficiency loss is recombination of the photoexcited

electron with the hole. In silicon, this rate is approximately 7.52×10^{-4} s^{-1}.[22] This recombination prevents the electron and hole from being used as charge carriers, and the emitted energy, either in the form of a photon or vibrational energy loss, also contributes to efficiency reduction. Altogether, sources of loss limit the efficiency of single junction devices to approximately 33.7%.[19,23,24]

1.2.2 Organic Photovoltaics

Organic photovoltaic devices function similarly to inorganic semiconductors, and are subject to many of the same efficiency losses as posited by the Shockley-Queisser limit. However, the nature of the excited state generated upon light absorption in organic materials is fundamentally different than that in inorganic devices.[25] In organic materials, the dielectric constant is much lower than in silicon, resulting in reduced shielding of the attraction between the electron and hole.[19] As a result, the electron and hole remain Coulombically bound to one another, creating a pseudoparticle known as an exciton. The exciton is a neutrally charged particle, and as such cannot be used to conduct charge necessary for electric work. The attraction between the electron and hole must be overcome in order to generate the free charges necessary to power an external load. This binding energy is typically 0.3-1.4 eV in organic materials, an order of magnitude greater than in silicon.[21,26] The excess thermal energy available under normal solar cell operating conditions is on the order of kT, which is approximately 0.026 eV.[27] The excess thermal energy available is thus insufficient to dissociate the exciton.

The highest occupied molecular orbital (HOMO) is the highest energetic orbital in a molecule where an electron resides prior to photoexcitation. Upon absorption of a photon, the electron is promoted to the lowest unoccupied molecular orbital (LUMO), while leaving a positively charged hole in the HOMO. The LUMO and HOMO are analogous to the conduction band and valence band, respectively, in a crystalline silicon semiconductor. The difference in the energy between the LUMO and HOMO can be referred to as the band-gap, E_g. One way to overcome the Coulombic attraction between the electron in hole occurs at the interface between two materials, a donor and an acceptor. At the interface, the exciton may form what is known as a charge-transfer exciton, where the electron is located on the acceptor yet still retains a Coulombic attraction to the hole on the donor. The acceptor material is generally designed such that its LUMO and HOMO are lower in energy than that of the donor material. This energetic difference will often drive charge separation, as the electron will be injected from the LUMO of the donor into the HOMO of the acceptor, while the hole remains localized in the donor HOMO. The now separated charges are free to migrate within the donor and acceptor material, and if collected at the electrodes can be used to drive an external circuit.

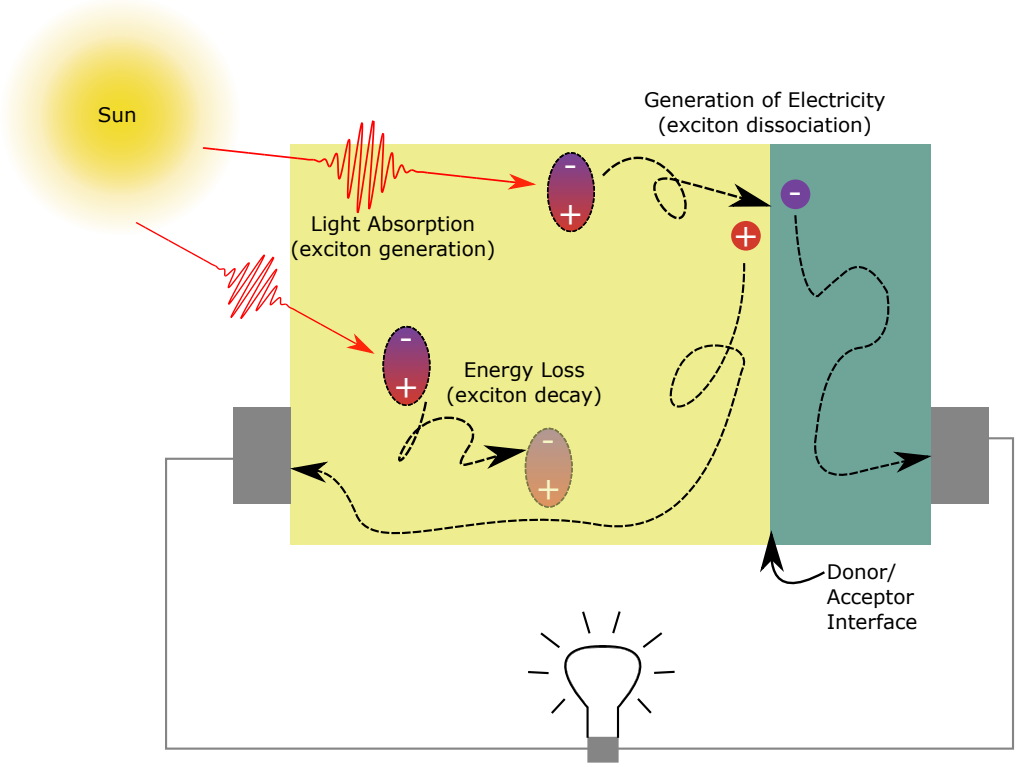

Figure 1.4: A schematic of an organic photovoltaic device showing exciton formation, diffusion, and dissociation.

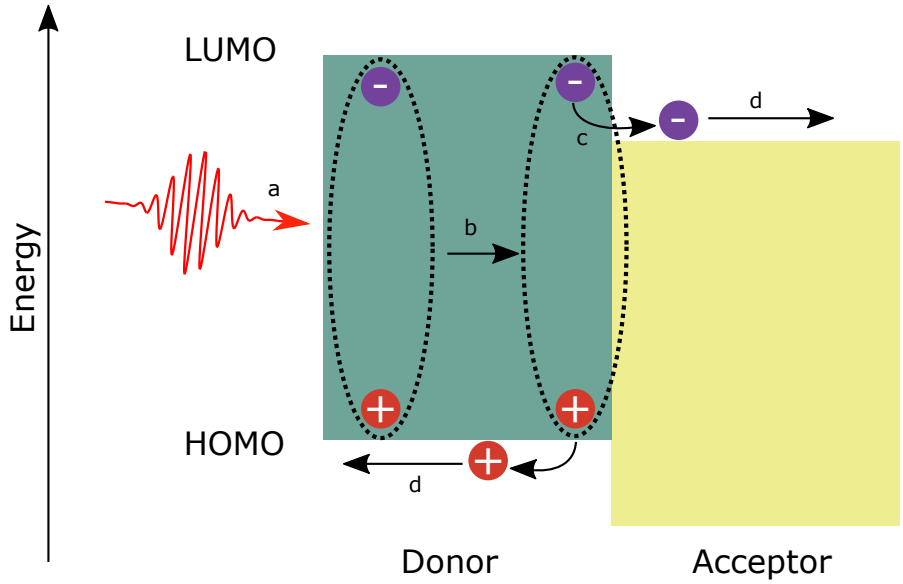

Figure 1.5: A schematic of an organic photovoltaic device showing exciton formation, diffusion, and dissociation.

Organic devices must be several hundreds of nanometers thick in order to capture the majority of incident sunlight. After light absorption, many excitons may be generated away from the interface between the donor and acceptor material, and in order to be useful for electrical work must migrate to the heterojunction by diffusion. However, excitons in organic materials can typically only diffuse 10-20 nm before the electron recombines with the hole. The relatively short diffusion lengths compared to the device thickness means that many of the generated excitons will not reach the heterojunction between donor and

acceptor materials. Balancing the efficiency gains by increasing film thickness in order to increase light absorption with the losses generated due to excitons not diffusing to the interface is trade-off known as the exciton bottleneck, and is a fundamental limit to device efficiency.[28] In an organic cell, recombination of the excited electron and hole is a much greater source of efficiency loss than in a silicon cell.

The external quantum efficiency, η_{EQE}, depends on four factors.

$$\eta_{EQE} = \eta_A \eta_{ED} \eta_{CT} \eta_{CC} \tag{1.1}$$

Each η represents the efficiency of a different physical process within the cell: η_A is the absorption efficiency, η_{ED} is the exciton diffusion efficiency, η_{CT} is the charge transfer efficiency, and η_{CC} is the charge collection efficiency.[28]

Understanding the key physical processes that contribute to exciton recombination and diffusion is critical to developing more efficient organic photovoltaic materials. Sometimes tuning molecular properties to enhance one of these efficiencies can have unintended effects on the other efficiencies, such as a reduction in the diffusion length that results from tuning a molecular structure to absorb a different region of the solar spectrum. By relating parameters such as molecular structure, film morphology, and device architecture to the fundamental physical processes occurring in the materials, a more rational approach to tuning these behaviors is possible.

1.3 Exciton Photophysics

This section will focus on the physics behind exciton formation, transport, and decay and provide a general context necessary to understand the topics discussed within this dissertation.

1.3.1 Exciton Formation

The first step in the process of solar energy collection involves the formation of an exciton, which begins with the absorption of a photon by a molecule. A photon possesses energy defined by Equation 1.2.

$$E = h\nu = \frac{hc}{\lambda} \tag{1.2}$$

Here, h is Planck's constant (6.626×10^{-34} J s), c is the speed of light, and ν and λ are the photon frequency and wavelength, respectively. If a photon possesses energy resonant with a molecular transition, the photon may be absorbed, resulting in an electronic transition promoting the molecule to an excited state. Different molecules will absorb different frequencies of light, depending on their electronic and vibrational structure.

In the presence of an oscillating electric field induced by a photon, the probability of absorbing a photon and transitioning from one electronic state to another electronic state is given by the square of the transition moment integral.[27,29] The transition moment integral,

M, has the form given by Equation 1.3.

$$M = \int \psi'^{*} \hat{\mu} \psi \mathrm{d}\tau = \langle \psi' | \, \hat{\mu} \, | \psi \rangle \tag{1.3}$$

The initial and final wave functions are given by ψ and ψ', respectively, while $\hat{\mu}$ is the transition dipole moment operator. The transition dipole moment operator $\hat{\mu}$ can be separated into two components, $\hat{\mu_e}$ and $\hat{\mu_n}$ depending on the electronic and nuclear coordinates, respectively. Moreover, the Born-Oppenheimer approximation, which states that electronic transitions are rapid relative to nuclear motion, allows for the total molecular wave function to be written as the product of three wave functions as shown in Equation 1.4

$$\psi = \psi_\nu \psi_e \psi_s \tag{1.4}$$

The three wave functions include the vibrational wave function (ψ_ν, the electronic orbital wave function ψ_e, and the electron spin wave function ψ_s. Because $\hat{\mu_e}$ does not operate on ψ_ν or ψ_s, and $\hat{\mu_n}$ does not operate on ψ_e or ψ_s, M can be more completely written as

$$M = \langle \psi'_\nu \psi_\nu \rangle \, \langle \psi'_e | \, \hat{\mu}_e \, | \psi_e \rangle \, \langle \psi'_s \psi_s \rangle \tag{1.5}$$

The first term, dealing with vibrational selection rules, is known as the Franck-Condon factor. The second and third terms form the basis of the orbital and spin selection rules, respectively. If any of these terms integrates to 0, then a transition is said to be forbidden.

Combined, these three factors tell us what frequencies of light will be absorbed, and in what relative proportion. The chemical nature of the molecule determines what values the factors take.

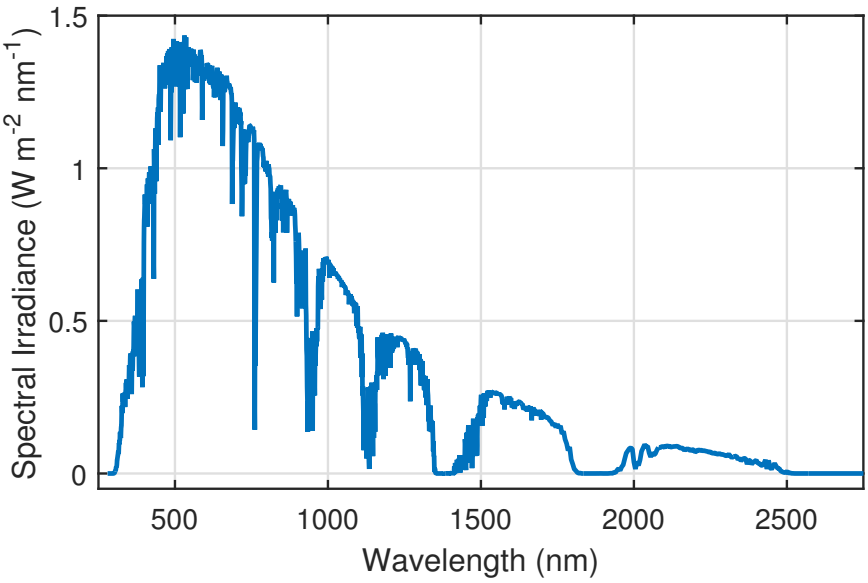

Figure 1.6: The solar irradiance spectrum AM 1.5. Data obtained from NREL.[30]

Tailoring the chemical structure of organic molecules to provide a better overlap of the molecular absorption spectrum with the solar irradiance spectrum (Figure 1.6), thus improving the photon capturing efficiency, has been one approach towards improving OPV device performance. However, tuning the absorption spectrum is seldom an act in isolation: by adjusting the electronic and vibrational properties of the molecule, other excited state processes such as energy transfer and exciton decay dynamics can be influenced as well. The effect of one such example of spectral absorption tuning on excited state

dynamics in conjugated polymers will be investigated in the PTV chapter. We will also investigate the influence of vibrational contributions to electronic spectroscopy, in particular how annihilation-induced heating manifests itself as spectral changes in subphthalocyanine mixed film transient absorption spectra.

1.3.2 Exciton Migration

The migration of an exciton throughout an organic material is a major contribution to the ultimate efficiency of an OPV device. There are two factors which need to be understood when considering exciton transport, the overall motion of the exciton and the mechanism by which that motion occurs. Exciton diffusion provides a mesoscopic description of the transport, while energy transfer describes the individual steps which comprise that transport.

Exciton Diffusion

Exciton diffusion is the process whereby an exciton migrates throughout a film, and ultimately reaches a boundary between a donor and acceptor material. Diffusion is derived stochastically, making use of the concept of a random walk, that is, a particle which starts at a point and will take steps in random directions.[31–34]

In this approach, we first consider the simple case of a particle constrained to movement in a single dimension, along a straight line. A particle initially at position x_0 at time t_0. After a time increment Δt, the particle can move a distance of Δx in either the positive or

negative direction, thus ending at either position $x_0 - \Delta x$ or $x_0 + \Delta x$ (note that a particle must move after a time increment Δt, that is $x(t_0) \neq x(t_0 + \Delta t)$. For isotropic diffusion, the probability of moving either direction is exactly $1/2$. If we assume that we now have a system of many random walkers, each moving randomly with the same step size and time interval as the initial particle, we can define $P(x, t)$ as the probability density of walkers at position x at time t. At time $t_0 + \Delta t$, half the walkers at position x_0 will have come from $x_0 + \Delta x$ and half from $x_0 - \Delta x$; all of the walkers initially at x_0 will have moved away. We can thus express the probability density $P(x_0, t_0 + \Delta t)$ by Equation 1.6.

$$P(x_0, t_0 + \Delta t) = \frac{1}{2}P(x_0 + \Delta x, t_0) + \frac{1}{2}P(x_0 - \Delta x, t_0) \tag{1.6}$$

To get to the well-known form of the diffusion equation, we perform a Taylor expansion for each term in Equation 1.6. For the left-hand side, we expand around Δt, yielding Equation 1.7.

$$P(x_0, t + \Delta t) = P(x_0, t_0) + \frac{\partial P}{\partial t}(x_0, t_0)(\Delta t) + \mathrm{O}((\Delta t)^2) \tag{1.7}$$

Here, $\mathrm{O}((\Delta t)^2)$ indicates higher order terms $(\Delta t)^2$ and above. Since Δt is taken to be very small, these higher order terms can be neglected. For the right-hand side of the equation, we expand around Δx, yielding equations for $P(x_0 + \Delta x, t_0)$ and $P(x_0 - \Delta x, t_0)$ in Equations 1.8 and 1.9, respectively.

$$P(x_0 + \Delta x, t_0) = P(x_0, t_0) + \frac{\partial P}{\partial x}(x_0, t_0)(\Delta x) + \frac{1}{2}\frac{\partial^2 P}{\partial x^2}(x_0, t_0)(\Delta x)^2 + \mathrm{O}((\Delta x)^3) \tag{1.8}$$

$$P(x_0-\Delta x,t_0)=P(x_0,t_0)+\frac{\partial P}{\partial x}(x_0,t_0)(-\Delta x)+\frac{1}{2}\frac{\partial^2 P}{\partial x^2}(x_0,t_0)(-\Delta x)^2+\mathrm{O}((-\Delta x)^3) \quad (1.9)$$

Equations 1.7, 1.8, and 1.9 can be substituted into Equation 1.6. Cancellation of terms and neglect of the higher order terms leads to the following expression

$$\frac{\partial P}{\partial t}(x_0,t_0)(\Delta t)=\frac{1}{2}\frac{\partial^2 P}{\partial x^2}(x_0,t_0)(\Delta x)^2 \quad (1.10)$$

Dividing both sides of Equation 1.10 by Δt results in the conventional form of the diffusion equation in one-dimension.

$$\frac{\partial P}{\partial t}(x_0,t_0)=\frac{(\Delta x)^2}{2\Delta t}\frac{\partial^2 P}{\partial x^2}(x_0,t_0)=D_{1D}\frac{\partial^2 P}{\partial x^2}(x_0,t_0) \quad (1.11)$$

Here, we define D_{1D} as the one-dimensional diffusion coefficient in the limit that Δx and Δt approach 0.

A fundamental solution to the diffusion equation is known as the Green's function of the diffusion equation.[34] In one-dimension, the Green's function is given by $P(x,t)$ in Equation 1.12.

$$P(x,t)=\frac{P_0}{2\sqrt{\pi D_{1D}t}}e^{-x^2/4D_{1D}t} \quad (1.12)$$

This solution can be used to evaluate how far a particle or exciton might travel. We

examine two cases: the expectation value of the particle displacement, x, and that of the square of the displacement x^2.

$$\langle x \rangle = \int_{\infty}^{\infty} xP(x,t)\mathrm{d}x = 0 \tag{1.13}$$

$$\langle x^2 \rangle = \int_{\infty}^{\infty} x^2 P(x,t)\mathrm{d}x = 2D_{1D}t \tag{1.14}$$

Some intuitive meaning can be found in the values of x and x^2. For an infinite number of steps, a random walker is expected to make an equal number of steps in the positive direction as it makes in the negative direction, and on net should end up back in the initial position. x^2 is reflective of the magnitude of the number of steps taken, that is, the total distance traveled. We define the characteristic one-dimensional diffusion length as the root-mean-squared displacement.

$$L_{D,1D} = \sqrt{2D_{1D}t} \tag{1.15}$$

The diffusion equation is a linear differential equation, and takes on an analogous form for multiple dimensions.

$$\frac{\partial P}{\partial t}(r,t) = D_n \nabla^2 P(r,t) \tag{1.16}$$

Because motion in each spatial direction is statistically independent, solutions to the diffusion equation are separable by dimension, that is, they will assume the form as a product

of one another.[35] For example, in three dimensions we can write the solution $P(r,t)$ as

$$P(r,t) = X(x)Y(y)Z(z)T(t) \tag{1.17}$$

This occurs because diffusion is assumed to be isotropic, and that motion in each of the Cartesian coordinates is independent of one another. The solution of $P(r,t)$ in three-dimensions is given by Equation 1.18

$$P(r,t) = \frac{P_0}{8(\pi D_{3D} t)^{3/2}} e^{-r^2/4D_{3D}t} \tag{1.18}$$

For the mean-square displacement in three dimensions, $\langle r^2 \rangle$ can be expressed as the sum of the independent contributions in each dimension.

$$\langle r^2 \rangle = \langle x^2 \rangle + \langle y^2 \rangle + \langle z^2 \rangle \tag{1.19}$$

More generally, for diffusion in n spatial dimensions, $\langle r^2 \rangle$ is given by Equation 1.20.

$$\langle r^2 \rangle = \int_{-\infty}^{\infty} r^2 P(r,t) \mathrm{d}\tau = 2nD_n t \tag{1.20}$$

Each Cartesian spatial direction independently contributes $2D_n t$ to the mean-square displacement. We establish the term diffusion length to refer to the root-mean-square

displacement, which for n dimensions is given by Equation 1.21.

$$L_{nD} = \sqrt{2nD_n t} \tag{1.21}$$

In the literature, the $\sqrt{2n}$ term is sometimes omitted. Care should be taken when comparing diffusion lengths to make sure they are reported in the same manner.

An OPV can only generate a usable electric current if an exciton is able to reach an interface between a donor and acceptor material. Naturally, much research effort is geared towards increasing the diffusion length of the exciton. Ultimately, this is achieved via either increasing the rate at which the exciton migrates through the film (increasing the diffusion coefficient D) or by increasing the time t for which an exciton exists.

Energy Transfer

Energy transfer describes the process by which energy is exchanged between molecules. A molecule possessing excess energy, such as one in an excited state, may act as a donor, transferring energy to another molecule. The mechanisms of energy transfer permit an exciton to migrate throughout a film.

In this section, the discussion will proceed assuming that the energy is transferred from a donor in the first excited electronic state while the acceptor is in the ground electronic state. However, it should be noted that energy can be transferred from a molecule in an excited state to another molecule in an excited state. One example of such a process is

exciton-exciton annihilation, which will be discussed in Section 1.3.4.

We begin by writing the initial and final total wave functions of the system, Ψ_i and Ψ_f.

$$\begin{aligned} \Psi_i &= \frac{1}{\sqrt{2}} \left[\psi'_{D,1} \psi_{A,2} - \psi'_{D,2} \psi_{A,1} \right] \\ \Psi_f &= \frac{1}{\sqrt{2}} \left[\psi_{D,1} \psi'_{A,2} - \psi_{D,2} \psi'_{A,1} \right] \end{aligned} \tag{1.22}$$

The subscript D or A refers to whether the wave function corresponds to that of the donor or acceptor, respectively. ψ' indicates a wave function describing an electron in an excited state. Since electrons are fermions, it is impossible to distinguish which electron in the donor or acceptor is the excited one, the wave functions must be written as a linear combination of the two potential spin states of the electron, indicated by the subscript 1 or 2.

The transition probability per unit time for a donor-acceptor system from a state Ψ_i with an initially excited donor to a state with an excited acceptor Ψ_f can be derived using time dependent perturbation theory and Fermi's golden rule.[36]

$$P_{DA} = \frac{2\pi}{\hbar} \left| \langle \Psi_f | \, H_1 \, | \Psi_i \rangle \right|^2 \rho_f(E_f = E_i) \tag{1.23}$$

Here, the operator H_1 is the Hamiltonian corresponding to the Coloumbic interaction between the donor and acceptor. $\rho_f(E_f = E_i)$ is the density of final states with identical

energy to the initial state.

$$\langle H_1 \rangle = \underbrace{\langle \psi_{D,1} \psi'_{A,2} | \, H_1 \, | \psi'_{D,1} \psi_{A,2} \rangle}_{\text{Förster}} - \underbrace{\langle \psi_{D,1} \psi'_{A,2} | \, H_1 \, | \psi'_{D,2} \psi_{A,1} \rangle}_{\text{Dexter}} \tag{1.24}$$

The first term represents the Coulombic interaction between donor and acceptor, and, if dipole-dipole interaction is dominant, gives rise to Förster energy transfer. The latter term arises from the possibility of a physical exchange of electrons between donor and acceptor, a process known as Dexter energy transfer. Each of the two contributions will now be examined individually.

Förster Energy Transfer

One form of energy transfer was first elaborated by Förster in 1948.[37,38] The first term in Equation 1.24 can be evaluated to yield an expression for the rate of Förster energy transfer, k_F.

$$k_F = \frac{1}{\tau} \left(\frac{R_0}{r} \right)^6 \tag{1.25}$$

The fluorescence lifetime of the donor is given by τ, r is the distance between the donor and acceptor, and R_0 is a parameter known as the Förster Radius. R_0 is defined as the separation distance between a donor and acceptor at which the rate of Förster energy transfer is equal to the rate of fluorescence decay, thus each event occurring with equal

probability. Mathematically, R_0 can be expressed by Equation 1.26.

$$R_0^6 = \frac{9\phi_D \ln(10)\kappa^2}{128\pi^5 n^4 N_A} \int_0^\infty f_D(\lambda)\epsilon_A(\lambda)\lambda^4 \mathrm{d}\lambda \tag{1.26}$$

The fluorescence quantum yield of the donor is ϕ_D, n is the refractive index of the solvent or medium between the donor and acceptor, N_A is Avogadro's number, and κ is a dipole orientation factor. For an isotropic distribution of dipoles, such as in solution where dipoles are free to rotate, κ^2 is equal to 2/3. In a more condensed phase, such as thin films, κ^2 is equal to approximately 0.476 due to constraint of the dipole rotation.[28] The integral term in Equation 1.26 (sometimes labeled as J in the literature), is the spectral overlap integral, which gives the probability that the donor and acceptor energy gap are equal. This term takes into account the spectral overlap between the area normalized emission of the donor, $f_D(\lambda)$, and the absorption of the acceptor, $\epsilon_A(\lambda)$.

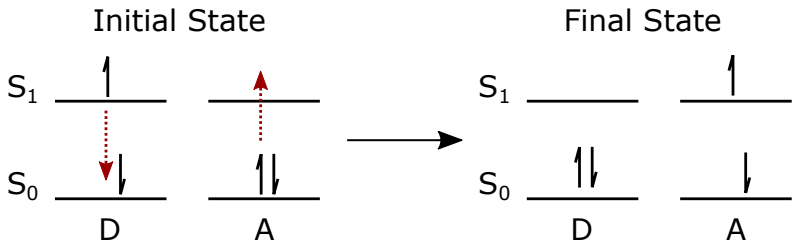

Figure 1.7: Diagram depicting Förster energy transfer process between a donor molecule (D) and an acceptor molecule (A).

While R_0 and k_F both have a dependence on the efficiency of the fluorescence process of the donor, it is important to realize that Förster energy transfer is a radiationless process, and does not involve the emission of an actual photon. Direct energy transfer is achieved by means of resonance between the oscillations of the donor molecule with that of the acceptor molecule. Because of this, Förster energy transfer is sometimes said to involve a "virtual photon." Energy can be transferred via emission of a real photon and subsequent reabsorption of said photon by another chromophore, however practically speaking this contributes very little to exciton migration within a film due to efficiency limitations and restricted system geometry.

Förster energy transfer is one means by which an exciton may migrate through a film. Values of R_0 are generally long range, typically on the order of 1-10 nm, when compared with intermolecular distances in organic thin films, which are typically 1 nm.[28] By transferring energy from one chromophore to the next, an exciton may effectively diffuse throughout a film. If we assume that the rate of exciton hopping is equal to the Förster rate given by Equation 1.25, the isotropic (three-dimensional) diffusion coefficient D_F can be defined using the intermolecular distance between chromophores, d, in Equation 1.27.

$$D_F = \frac{R_0^6}{6d^4} \tag{1.27}$$

Likewise, a three dimensional diffusion length, L_D can be defined.[39]

$$L_{D,F} = \sqrt{\frac{R_0^6}{d^4}} = \sqrt{6 D_F \tau_F} \tag{1.28}$$

Dexter Energy Transfer

Unlike in Förster energy transfer, Dexter energy transfer requires the physical exchange of electrons between donor and acceptor chromophores. Because of this, the exchange contribution to Equation 1.24 is generally very small unless the donor and acceptor are in very close proximity. The rate of Dexter energy transfer via the exchange mechanism can be expressed

$$k_D = \frac{2\pi}{\hbar} K^2 e^{-2r/L} \int f_D(E) F_A(E) \mathrm{d}E \equiv \kappa e^{-2r/L} \tag{1.29}$$

where K^2 is term relating to overlap of the charge clouds of the donor and acceptor, possessing units of energy squared, r is the distance between the donor and acceptor, L is an effective average Bohr radius of the excited donor and unexcited acceptor. f_D and F_A are the emission and absorption of the donor and acceptor, respectively. Both terms are normalized such that the integral term becomes unitless when integrated over photon energy. This is a different normalization scheme than that present in Equation 1.25. All of the terms except the exponential are often collected and written together as κ for simplicity of expression.

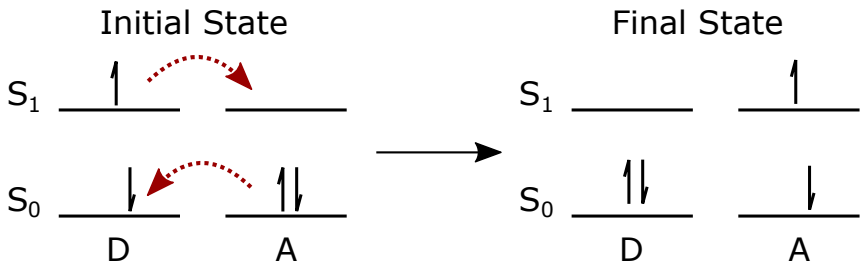

Figure 1.8: Diagram depicting Dexter energy transfer process between a donor molecule (D) and an acceptor molecule (A).

The exciton hopping distance is generally smaller in molecules where energy transfers primarily via a Dexter mechanism than in materials dominated by Förster transfer processes. A three-dimensional diffusion coefficient can be calculated for Dexter energy transfer.

$$D_D = \frac{d^2 \kappa e^{-2d/L}}{6} \tag{1.30}$$

where d is again the intermolecular separation. The diffusion length can similarly be calculated as that in FRET.

$$L_{D,F} = \sqrt{d^2 \tau \kappa e^{-2d/L}} \tag{1.31}$$

1.3.3 Exciton Decay

Excitons are subject to recombination, relaxing from an excited state back to a ground electronic state as the electron relaxes back into the hole. The duration of time for which an exciton exists is known as a lifetime, and often represented by τ, which is an exponential time constant assuming first order decay. The exciton lifetime is a crucial parameter in determining how far an exciton can diffuse. Knowledge of how physical and chemical factors influence the different exciton decay pathways can aid in the design of excitons with longer lifetimes, and consequently longer diffusion lengths.

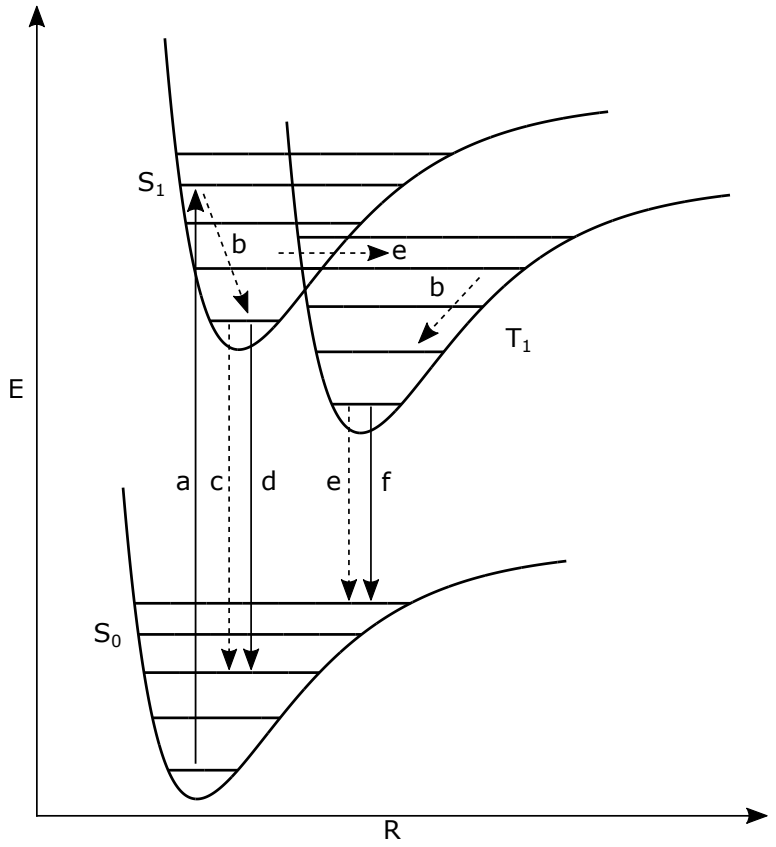

Figure 1.9: Diagram depicting sources of excited state decay. The vertical axis increases with increasing energy, and the horizontal axis depicts the normal coordinate. Arrows indicate transitions between different states as follows: a) Absorption, $S_0 \rightarrow S_1$, b) Vibrational relaxation, nonradiative, c) Internal conversion, nonradiative, $S_1 \rightarrow S_0$, d) Fluorescence, radiative, $S_1 \rightarrow S_0$, e) Intersystem crossing, nonradiative, $S_1 \rightarrow T_1$ and $T_1 \rightarrow S_0$, f) Phosphorescence, radiative, $T_1 \rightarrow S_0$.[29,40]

Figure 1.9 depicts the different pathways of excited state decay available to a molecule.

A molecule in the ground electronic state, S_0, can absorb a photon and be promoted into an excited singlet state, S_1. Once excited, several fundamental decay pathways between energy levels are possible. These can be classified into two categories: radiative transitions, which involve the emission of a photon, and nonradiative transitions, which do not. In general, absorption from S_0 to S_1 is likely to promote a molecule to a vibrationally excited state within the excited electronic state, the particular level depending on the overlap of the two vibrational wave functions. Vibrational relaxation of the molecule within the excited state manifold often occurs within 100s of femtoseconds (Table 1.3.3, relaxing to the lowest vibrational level ν_0 within the potential well. Because this thermalization happens on such a rapid timescale, radiative electronic relaxation from the excited state often occurs only from the ν_0 vibrational level, a tendency referred to as Kasha's Rule.[41] From ν_0 of the excited S_1 state, two different relaxation pathways are possible where the spin multiplicity of the electron is preserved. Internal conversion is the nonradiative decay process from S_1 to S_0, while fluorescence is the corresponding radiative decay process. Fluorescence and internal conversion often occur on picosecond to nanosecond timescales (Table 1.3.3).

Intersystem crossing is a nonradiative transtion that occurs when overlap between the vibrational levels of S_1 and the triplet state T_1 permits the spin multiplicity of the electron to change. Once in the triplet manifold, the molecule is still subject to vibrational relaxation and other sources of excited state decay. From T_1, there are again two transition pathways back to the ground electronic state S_0, each involving a change in spin multiplicity. Intersystem crossing is the nonradiative decay pathway, usually mediated by

collisions or vibrational energy exchange between neighboring molecules. The radiative decay pathway from T_1 to S_0 is a slow process (relative to that of S_1 to S_0 and described in Table 1.3.3)known as phosphorescence. The spin forbidden nature of this transition means that the timescales on which phosphorescence occurs are typically several orders of magnitude longer than that of the analogous fluorescence process, with relaxation often taking hundreds of microseconds to occur.

Process	Transition	Radiative	Δ Spin Multiplicity	Timescale
Vibrational relaxation	-	No	No	10^{-14} s
Internal conversion	$S_1 \rightarrow S_0$	No	No	10^{-12}-10^{-7} s
Fluorescence	$S_1 \rightarrow S_0$	Yes	No	10^{-9} s
Intersystem Crossing	$S_1 \rightarrow T_1$	No	Yes	10^{-12}-10^{-6} s
Phosphorescence	$T_1 \rightarrow S_0$	Yes	Yes	10^{-7}-10^{-5} s
Intersytem Crossing	$T_1 \rightarrow S_0$	No	Yes	10^{-8}-10^{-3} s

Table 1.1: Timescales of selected first-order excited state decay pathways.[40]

The mechanism by which a molecule undergoes unimolecular decay from an excited state to the ground state can be written according to Equation 1.32.

$$\begin{aligned} S_1 &\xrightarrow{k_r} S_0 \\ S_1 &\xrightarrow{k_{nr}} S_0 \end{aligned} \tag{1.32}$$

The rate coefficients of unimolecular radiative and nonradiative decay are given by k_r and k_{nr}, respectively. The change in population of the excited state[S_1] can be written as the differential equation.[42]

$$-\frac{\mathrm{d}[S_1]}{\mathrm{d}t} = (k_r + k_{nr})[S_1] = k_t[S_1] \tag{1.33}$$

Equation 1.33 can be trivially solved, and yields an exponential decay function.

$$[S_1] = [S_1]_0 e^{-k_t t} \tag{1.34}$$

Here, k_t is the total rate coefficient from the excited state, obtained as the sum of k_r and k_{nr}, and $[S_1]_0$ is the initial population of excitons generated immediately after photoexcitation. The exponential decay is a useful model for mathematically describing exciton functions as a population of time.

First-order decay pathways such as those described above typically depend only on the exciton itself, and are not influenced by other excitons generated within the material. However, when exciton density is high, as may be encountered during pump-probe experiments on condensed phase materials such as thin films, another source of exciton decay becomes competitive with unimolecular decay: exciton annihilation. In exciton annihilation, two or more excitons may interact with one another in such a way that the energy of one or more excitons is nonradiatively lost. When exciton annihilation is a prevalent form of population loss, exponential decays are no longer the correct functional form to model

the physical processes occurring in the system.

1.3.4 Exciton Annihilation

Exciton annihilation is a source of exciton decay that occurs when the influence of one exciton on the excited state lifetime of another is no longer negligible. Depending on the absorption cross section, the instantaneous exciton density generated by absorption of natural solar light in a photovoltaic cell is many orders of magnitude less than the molecular density of the absorbing material. Under normal operating conditions, the probability of two excitons encountering one another is generally quite low. However, in ultrafast pump-probe experiments, high pulse energies within a short duration of time means that in thin organic films many excitons will be generated simultaneously and in close proximity. Exciton annihilation can therefore be an appreciable source of energy loss and must be taken into consideration when interpreting excited state photophysics in condensed phase materials.

Figure 1.10 is a simplified depiction of exciton annihilation. First, two excitons A and B exist in a radius small enough for them to couple with one another. This may happen as a result of exciton diffusion, or through longer-range Förster type interactions. The energy from exciton B is absorbed by exciton A, promoting exciton A to a higher lying excited state, while exciton B relaxes back to the ground state. The higher lying transient exciton is unstable, and very rapidly (on the order of femtoseconds) relaxes back to the first excited state by dissipating the excess energy through internal conversion. As the molecule

relaxes, the vibrational energy must be absorbed by the surrounding bath, which could include the chromophore on which exciton B was initially located, other chromophores or molecules neighboring exciton A or interfaces such as the air or substrate. Generally, in a solid-state film macroscopic diffusion of vibrational energy as heat is a slow process relative to electronic processes, and so the final state of the system is that of a single exciton and neighboring molecules which exist in a vibrationally excited ground electronic state.

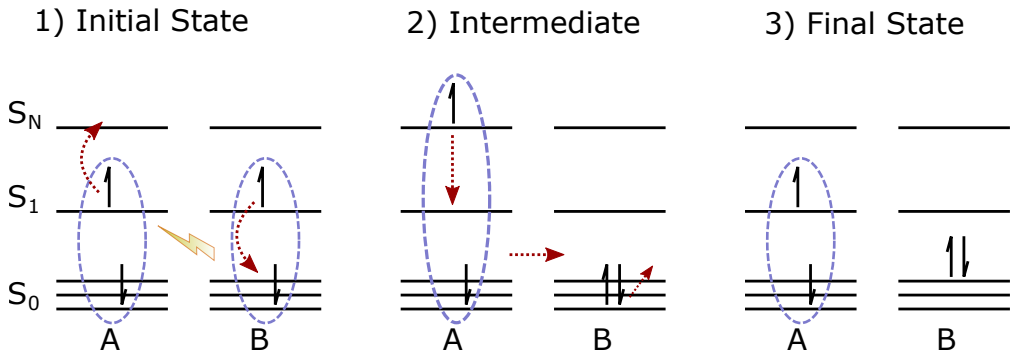

Figure 1.10: Diagram depicting the exciton annihilation process. 1) Two excitons interact with one another, resulting in the near instantaneous promotion of exciton A to a higher lying excited state and the relaxation of B to a ground state. 2) The higher lying exciton rapidly and nonradiatively relaxes back to S_1, with vibrational energy transferred to the surroundings. 3) The final state of the system, consisting of one exciton and one molecule in a vibrationally excited yet electronic ground state.

In Section 1.3.3, it was shown how exciton populations could be modeled as first-order

decays when second-order processes such as annihilation were absent. Exciton annihilation is usually considered in the context of a bimolecular rate equation.[43–45] When exciton annihilation occurs, both that process and first-order processes contribute to depopulation of the excited state.

$$\frac{\mathrm{d}n(t)}{\mathrm{d}t} = -kn(t) - f\gamma(t)n(t)^2 \tag{1.35}$$

Here, $n(t)$ is the exciton population density as a function of time, k is the intrinsic decay rate of the exciton(that is, the low excitation density decay rate which is governed primarily by unimolecular non-radiative and radiative decay processes), and $\gamma(t)$ is the rate coefficient of the annihilation process. The factor f depends on the survival of excitons after the annihilation event. In the circumstance where both excitons are annihilated, for example, if the event results in an ionization, f equals 1. If only one exciton remains, then f is equal to 1/2. Care should be taken when evaluating examples in the literature, as f is occasionally omitted in Equation 1.35 and often incorporated directly into the definition of $\gamma(t)$. In the derivations that follow, we assume that exciton annihilation does not result in ionization of the molecules, and thus use $f = 1/2$.

To begin, the substitution $y = 1/n(t)$ can be employed in order to transform Equation 1.35 from a nonlinear differential equation into one that is both first-order and linear. Using $\mathrm{d}n(t)/\mathrm{d}t = -(1/y^2)\mathrm{d}y/\mathrm{d}t$ and multiplying by $-(1/y^2)$, Equation 1.35 can be rewritten as Equation 1.36.

$$\frac{\mathrm{d}y}{\mathrm{d}t} - ky = f\gamma(t) \tag{1.36}$$

Equation 1.36 is then multiplied by the integrating factor e^{-kt} to yield Equation 1.37.

$$e^{-kt}\frac{\mathrm{d}y}{\mathrm{d}t} - ke^{-kt}y = e^{-kt}f\gamma(t) \tag{1.37}$$

One may recognize that the left hand side of Equation 1.37 is merely the application of the product rule.

$$\frac{\mathrm{d}}{\mathrm{d}t}(e^{-kt}y) = e^{-kt}\frac{\mathrm{d}y}{\mathrm{d}t} - ke^{-kt}y \tag{1.38}$$

Equation 1.38 can be substituted into Equation 1.37 to yield an easily solvable differential equation.

$$\frac{d}{dt}(e^{-kt}y) = e^{-kt}f\gamma(t) \tag{1.39}$$

Equation 1.39 is integrated to yield the general form shown in Equation 1.40.

$$e^{-kt}y = \int_0^t e^{-kt}f\gamma(t)\mathrm{d}t + c \tag{1.40}$$

Equation 1.40 can then be solved analytically when the functional form of $\gamma(t)$ is known. The annihilation coefficient $\gamma(t)$ can take on different forms depending on the physics underlying the annihilation mechanism. The following sections will focus on the derivation of various forms of $\gamma(t)$, and the resulting functional form of $n(t)$.

Diffusion-Limited Exciton Annihilation

An analogous problem to that of three dimensional exciton diffusion and annihilation is that of the coagulation of colloidal particles.[33,46,47] It is first assumed that there exists a material with a uniform distribution of excitons, each possessing a critical radius R_c. In the original derivation, if two colloidal particles approached each other within this critical distance, they were assumed to instantaneously coalesce into a single "double particle." In the case of exciton annihilation, we assume that the coalescence results in a single exciton remaining. Each exciton will possess motion as described by the standard diffusion equation, until such point that they move within R_c. When the separation between two excitons is less than or equal to R_c, one of the excitons is lost.

In order to determine the rate of annihilation, we need to know the rate at which excitons will diffuse within the critical radius of another exciton. First, we will consider the case of a stationary particle fixed at the origin of a coordinate system. We then attempt to determine what is the rate of excitons entering into the stationary exciton sphere of influence at a radius r equal to R_c.

The diffusion equation can be employed to determine this rate. First, it's given that a particle possesses probability $P(r,t)$ of existing at position r from another particle at time t.

$$\frac{\partial P}{\partial t} = D\nabla^2 P \tag{1.41}$$

The solution to Equation 1.41 must satisfy the boundary conditions given below.

$$P\text{=p, at } t = 0, \text{ for } \mid r \mid > R_c$$

$$P\text{=0, at } \mid r \mid = R_c \text{ for } t > 0$$

The concentration of particles at distances $\mid r \mid > R_c$ at t=0 is held constant as a constant p. Since P depends only on the distance r from the center, the diffusion equation takes the form given by Equation 1.42.

$$\frac{\partial}{\partial t}(rP) = D\frac{\partial^2}{\partial r^2}(rP) \tag{1.42}$$

From the boundary conditions, the solution of Equation 1.42 can be readily solved.

$$P = p\left[1 - \frac{R}{r} + \frac{2R}{r\sqrt{\pi}}\int_0^{(r-R)/2(Dt)^{1/2}} e^{-x^2}\mathrm{d}x\right] \tag{1.43}$$

To determine the total rate $\gamma(t)$ of particles passing through a sphere of radius R_c, we multiply $\partial P/\partial r$ by the surface area, $4\pi R_c^2$ and evaluate the derivative at $r = R_c$.

$$\gamma(t) = 4\pi D\left(r^2\frac{\partial P}{\partial r}\right)_{r=R} = 4\pi DR_c\left(1 + \frac{R}{(\pi Dt)^{1/2}}\right) \tag{1.44}$$

As stated, the right hand side of Equation 1.44 is valid for the situation in which one exciton is stationary. When both excitons are in motion, the rate of annihilation depends on the relative displacements of both. For two exciton with diffusion coefficients D_1 and

D_2 we find for the rate of coagulation $\gamma(t)$ can be expressed as in Equation 1.45.

$$\gamma(t) = 4\pi(D_1 + D_2)R_c\left(1 + \frac{R_c}{(\pi(D_1 + D_2)t)^{1/2}}\right) \tag{1.45}$$

A reasonable assumption can be made that the diffusion coefficient is the same for all excitons, that is $D = D_1 = D_2$. In this case, the final form of the annihilation coefficient for isotropic diffusion in three dimensions is thus

$$\gamma_{3D}(t) = 8\pi D R_c\left(1 + \frac{R_c}{(\pi(2Dt)^{1/2}}\right) \tag{1.46}$$

A similar procedure can be followed to derive the annihilation coefficient when exciton transport is constrained to one or two dimensions. The one-dimensional diffusion limited annihilation coefficient $\gamma_{1D}(t)$ is given by Equation 1.47.

$$\gamma_{1D}(t) = \frac{1}{a\rho}\sqrt{\frac{8D}{\pi t}} \tag{1.47}$$

The one-dimensional lattice constant is given by a, ρ is the three dimensional molecular density, and D is the diffusion coefficient in the direction of excitonic motion.[45]

When the functional form of $\gamma(t)$ is know, Equation 1.40 can be solved analytically. Equation 1.46 may be substituted into the integral portion of Equation 1.40, and using

$f = 1/2$, we obtain Equation 1.48.

$$\int_0^t e^{-kt} f\gamma(t)\mathrm{d}t = \int_0^t e^{-kt} 4\pi D R_c \left(1 + \frac{R_c}{(\pi(2Dt)^{1/2}}\right)\mathrm{d}t \tag{1.48}$$

The integral on the right hand side of Equation 1.48 can be solved analytically, and substitution of the solution into Equation 1.40 yields Equation 1.49.

$$e^{-kt}y = c + \frac{4\pi D R_c}{k}(1 - e^{-kt}) + 2\pi R_c^2 \sqrt{\frac{2D}{k}}\,\mathrm{erf}(\sqrt{kt}). \tag{1.49}$$

The error function, designated by erf, is defined by Equation 1.50.

$$\mathrm{erf}(x) = \frac{2}{\sqrt{\pi}} \int_0^x e^{-t^2}\mathrm{d}t \tag{1.50}$$

Recalling that $y = 1/n(t)$, and that the initial population at time $t = 0$ is given by $n(0)$, we can solve for c by substitution, obtaining

$$c = \frac{1}{n(0)} \tag{1.51}$$

This allows for the analytical form of the exciton population as a function of time to be clearly expressed by Equation 1.52.

$$n(t) = \frac{n(0)e^{-kt}}{1 + 4\pi D R_c n(0) k^{-1}(1 - e^{-kt}) + 2\pi\sqrt{2Dk^{-1}} R_c^2 n(0)\,\mathrm{erf}(\sqrt{kt})} \tag{1.52}$$

Thus, when a system exhibits isotropic, three-dimensional diffusive exciton motion and conditions of exciton annihilation, the population of excitons can be modeled by Equation 1.52.

Static Annihilation

In the limit of slow exciton transport, exciton annihilation via diffusion may not be an appreciable source of population loss. Static mechanisms may be responsible for annihilation.[45,48,49] In these cases it is often more intuitive to model the annihilation as a single step Förster or Dexter energy transfer annihilation process. The method used to derive $\gamma(t)$ for each method of energy transfer will be described briefly here, but a more thorough derivation is available in a 1965 publication by Inokuti and Hirayama.[48]

First, it is assumed that the only sources of exciton population loss occur due to spontaneous deactivation (fluorescence, internal conversion, etc.) and energy transfer to acceptors. The fraction of excited donors to that of the initial exciton population, $\phi(t)$ is given by Equation 1.53.

$$\phi(t) = e^{-kt} \lim_{N,V\to\infty} \left\{ \frac{4\pi}{V} \int_0^{R_V} e^{-k(r)t} R^2 \mathrm{d}R \right\}^N \tag{1.53}$$

Here, $k(R)$ is the rate coefficient of energy transfer from donor to acceptor at a distance R. N is the number of acceptors within a volume V defined by $V = 4\pi R_V^3/3$. The limit is taken such that the acceptor concentration, N/V is held constant as N and V both

go to infinity. This formalism accounts for energy transfer from the donor to all possible acceptors.

For a single-step annihilation method where Förster energy transfer is the annihilation mechanism, $\gamma_F(t)$ assumes the form given by Equation 1.54.

$$\gamma_F(t) = \frac{2}{3}\pi R_F^3 \sqrt{\pi k t^{-1}} \tag{1.54}$$

This leads to a functional form for the exciton population as a function of time $n(t)$ given by Equation 1.55.

$$n(t) = \frac{n(0)e^{-kt}}{1 + \frac{\pi^2 R_F^3}{3}\,\mathrm{erf}(\sqrt{kt})} \tag{1.55}$$

A model can also be constructed for exciton annihilation via Dexter energy transfer.[48,50] The curious reader is encouraged to read the full derivations.

1.4 Dissertation Overview

Thus far, many of the physical processes occurring in organic photovoltaics and how they are mathematically treated have been discussed. In particular, we have discussed how exciton populations can be modeled as a function of time and the previously mentioned physical processes. By measuring exciton populations as a function of time, and then fitting those populations with physical models, we can extract meaningful information about the

types and nature of the physical processes occurring. The timescales of these processes are very short, typically on the order of femtoseconds ($10^{-}15$ s) to microseconds ($10^{-}6$ s). Populations, or a signal proportional to population, needs to be monitored over these timescales if these physical processes are to be modeled.

Ultrafast pump-probe spectroscopy is one of the primary techniques used to characterize these physical processes. In this technique, a very short pump pulse of laser excitation is made incident upon a sample, which when absorbed can create excitons. A second probe pulse of laser excitation is then directed to the sample, from which further absorption can occur. Excitons will have a transient absorption that is different from the absorption in the ground electronic state. As the delay time between the pump and probe signal is changed, the state of the system will evolve as many physical processes, such as energy transfer, radiative decay, and exciton annihilation, occur.

In this dissertation, several different organic semiconducting systems were studied in order to better connect the photophysics with chemical and morphological considerations. In Chapter 3, a series of donor/acceptor conjugated statistical copolymers were generated where the percentage of donor/acceptor monomer unit was varied. This technique allows for the generation of low band-gap polymers, increasing the polymer overlap with the solar irradiance spectrum. We investigate the effects of tuning composition on excited state lifetimes in these materials.

In Chapter 4, thin films of an optically active chromophore, subphthalocyanine (SubPc), were prepared in a wide band-gap host matrix. By adjusting the concentration of SubPc in

the matrix, the diffusion length could be tuned, and moreover, improved over the diffusion length in films containing only SubPc. Models assuming isotropic three-dimensional exciton diffusion and exciton annihilation were used to evaluate the diffusion length as a function of this dilution. It was also determined that a large thermal component is prominent on sub-nanosecond time scales, and that this feature, when not properly accounted for, can ultimately skew the observed dynamics.

In Chapter 5, a similar host-guest architecture to that in Chapter 4 was employed. However, instead of a wide band-gap, optically inert host, another optically active material was selected. By incorporating mixed films of SubPc and the slightly smaller band-gap subnaphthalocyanine (SubNc), it was hoped that a similar improvement to exciton diffusion and consequently device efficiency could be achieved. Here, the diffusion length is measured in neat SubNc films, and energy transfer from an excited SubPc to an acceptor SubNc is modeled according to a Förster energy transfer mechanism.

Finally, in Chapter 6, the excited state behavior of a series of boron dipyrromethane (BODIPY) derivatives are studied. In addition, studies were conducted to see if the formation of supramolecular complexes between a BODIPY and C60 fullrene would occur. These supramolecular complexes have received increased attention in literature, as they are seen to mimic natural photosynthetic systems by stabilizing photoinduced charge-separated states. One of the main techniques utilized to investigate the association of the two molecules in an aggregate is photoluminescence quenching, whereby photoluminescence of a fluorophore is reduced as it transfers energy or electrons to a non-luminescent acceptor.

Here, we find no evidence of any complex formation, and preliminary results which suggest that improperly accounted for inner-filter effects may be responsible for the apparent photoluminescence quenching in many previously studied systems.

Chapter 2

Instrumentation

In this chapter, a brief overview will be given to both the theoretical and practical concepts relating to the experimental techniques and instrumentation employed in these studies.

2.1 Absorption Spectroscopy

It is important to know what range of radiation a molecule absorbs, as well as how strongly it absorbs that light. To quantify this, absorption spectroscopy is employed.

First, we consider how light is absorbed as it passes through a material. The incremental change in light intensity $\mathrm{d}I$ over an incremental distance $\mathrm{d}x$ through a chromophore with concentration c can be expressed by Equation 2.1.

$$\mathrm{d}I(\lambda) = -\beta I(\lambda) c \mathrm{d}x \tag{2.1}$$

The parameter β is a proportionality constant depending on the material.[51,52] To determine the intensity of light that remains after being transmitted through the sample, the differential equation is integrated over the boundary conditions.

$$-\int_{I_0(\lambda)}^{I(\lambda)} \frac{\mathrm{d}I(\lambda)}{I(\lambda)} = \int_0^l \beta c \mathrm{d}x \tag{2.2}$$

Evaluating the integral in Equation 2.2 yields a relationship between the natural logarithm of the ratio I/I_0.

$$-(\ln(I) - \ln(I_0)) = -\ln\left(\frac{I}{I_0}\right) = \beta c l \tag{2.3}$$

Convention typically dictates the use of a base-10 logarithm for reporting absorbance, hereafter referred to as optical density (OD).[52] The expression for OD as function of wavelength is shown in Equation 2.4.

$$OD(\lambda) = -\log_{10}\left(\frac{I(\lambda)}{I_0(\lambda)}\right) = \frac{\beta(\lambda)}{\ln 10} c l = \epsilon(\lambda) c l \tag{2.4}$$

An Olis Cary 14 spectrometer was used to collect steady-state absorption spectra for the experiments in this dissertation. The spectrometer contained two light sources depending on the wavelength range of light desired to be studied, a deuterium lamp for ultraviolet (UV) wavelengths and a tungsten lamp for visible and near-infrared (NIR) wavelengths. Radiation from the appropriate source is directed to a monochromator where specific wavelengths can be selected. A semicircular mirror on a chopper wheel rotating at 30 Hz

alternately sends half the beam to a reference cell and half the beam to a sample cell. After passing through the reference or sample, the light is directed to either a photomultiplier tube (PMT) or PbS detector to measure the intensity of UV/visible light and NIR light, respectively. The wavelength axis was calibrated using a holmium oxide standard, which possess a large number of well-defined absorption peaks for calibration purposes.[53]

In addition to the chromophore of interest, absorption also comes from other sources, such as solvent, cuvette, or film substrate. This additional absorption needs to be accounted for when collecting absorption spectra. To do this, a baseline absorption spectrum is collected with a blank, typically a cuvette containing neat solvent for solution measurements and a bare substrate for thin film measurements. The absorption spectrum of the blank is then subtracted from the absorption spectrum of the sample. This results in a corrected absorption spectrum with only absorption from the sample presented.

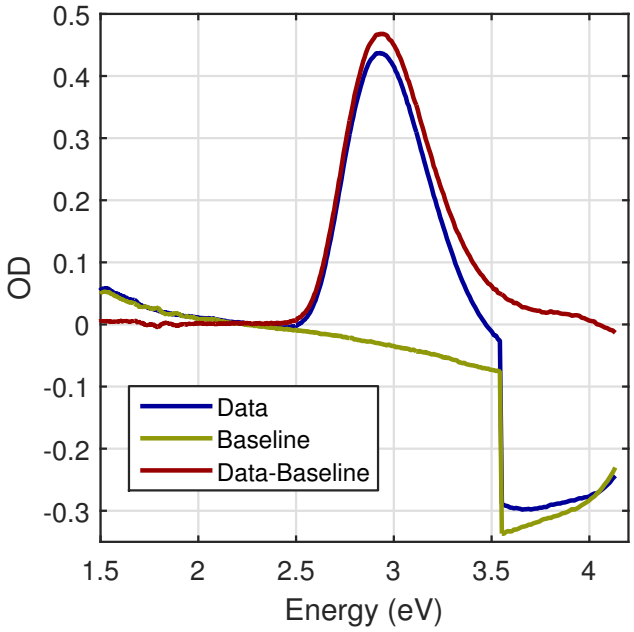

Figure 2.1: Sample UV-Vis spectrum. Raw data: blue; baseline: yellow; corrected data with baseline subtracted: red.

A sample absorption spectrum of the laser dye Coumarin 153 is plotted in Figure 2.1, including the raw data, the baseline, and the corrected absorption after baseline subtraction. The y-axis is the OD of the sample, while the x-axis is the photon energy. Often, absorption spectra are plotted as a function of wavelength, which involves use of the relation $E = hc/\lambda$.

2.2 Fluorescence Spectroscopy

A SPEX Fluorolog 1680 was employed in the characterization of the photoluminescent behavior of molecules. Light from a xenon lamp is first directed through a double monochromator, permitting the selection of a narrow wavelength band of light for sample excitation. The light is then directed with mirrors through a slit towards the sample chamber. Emitted radiation can be detected in either a front-face (typically employed for thin film photoluminescence measurements or concentrated solution measurements) or right-angle geometry (typically employed in dilute solution photoluminescence measurements).

After the geometry for emission is selected, the emitted photons are directed through another double monochromator before being detected by a PMT. The grating pair in the second monochromator are rotated simultaneously in the same direction, allowing for an entire photoluminescence spectrum to be collected as the wavelength is changed. In order to account for the wavelength dependence of the PMT and the monochromator gratings, a correction curve was created using the emission spectra of coumarin 153, quinine sulfate, DCM and LDS 751.[54] This calibration curve was utilized for all photoluminescence measurements.

The detected intensity of the emitted fluorescence of a molecule is influenced by a number of factors: choice of excitation wavelength, absorption of the sample, collection geometry, detector sensitivity, etc.[51,55,56] Often, we are interested in obtaining a more intrinsic measure of the photoluminescence efficiency that is comparable between molecules.

To achieve this, the fluorescence quantum yield Φ_i for a molecule is often calculated relative to that of a molecule with a known quantum yield.[56] Φ_i can be expressed by Equation 2.5.

$$\Phi_i = \Phi_r \frac{\int PL_i}{\int PL_r} \frac{OD_{r,\lambda}}{OD_{i,\lambda}} \frac{n_i^2}{n_r^2} \tag{2.5}$$

Φ_r is the known quantum yield of a reference, $\int PL_i$ and $\int PL_r$ are the integrated photoluminescence intensities of the sample and reference, respectively, $OD_{i,\lambda}$ and $OD_{r,\lambda}$ are the optical density of the sample and the reference at the excitation wavelength λ, respectively, and n_i and n_r are the refractive indices of the sample and reference, respectively. For solution measurements, n_i and n_r are generally taken to be the refractive indices of the neat solvent. It should be noted that the expression in Equation 2.5 is normally valid only for low concentrations. Samples with high concentrations of absorbing chromophores may not be well represented by this expression due to the inner-filter effect, which will be discussed in more detail later in this dissertation.[55]

2.3 Time Correlated Single Photon Counting

Time resolved fluorescence spectroscopy can be a useful tool for determining the excited state lifetimes of emissive molecules. Time correlated single photon counting (TCSPC) is one technique by which to measure it.

Samples were excited with a 40 MHz diode laser (Driver, Picoquant PDL 800-B; Heads: LDH series, 5 mW average power, 375 nm, 470 nm, 650 nm). The specific wavelength

of the laser head was selected such that it would be absorbed by the sample. A double monochromator (Jobin-Yvon TRIAX-320) is used to direct sample emission to an avalanche photodiode (Picoquant MPD PDM) for detection. The monochromator was set to pass a wavelength where the sample would emit. After each laser shot, a signal is sent to a timing card (Picoquant TimeHarp2000). When a photon emitted by the sample reaches the avalanche photodiode, another signal is sent to the timing card. The timing between the laser pulse and emitted photon detection is recorded, and a histogram is generated over a series of bins. With the setup employed herein, each bin has a width of approximately 31 ps.

Because of the binned nature of data collection, it is important that excitation power is kept low enough such that one or fewer emission events reach the detector per laser pulse cycle. The detector will report the time when the first photon per cycle is incident upon it, and then due to electronic limitations will experience a "dead time" during which it will not register other incident photons; photons reaching the detector later will be "lost". If multiple emission events occur per pulse, this has the effect of undercounting photons at long delay times, artificially skewing the histogram to shorter times and potentially resulting in decays that appear to decay faster than the underlying physical processes would actually merit.

The instrument response is obtained by placing a cuvette filled with salt in the beam path. The monochromator is tuned to select for the same wavelength as the excitation beam, and scatter from the cuvette is collected by the photodiode. The returned histogram

typically has a 500 ps FWHM and is used as the instrument response. When fitting data, this instrumental response function was convoluted with an exponential decay to generate the total fit.

2.4 Ultrafast Laser System

While TCSPC is useful for measuring excited state lifetimes of emissive molecules, it is relatively less helpful at elucidating the excited state lifetimes of nonemissive molecules. Furthermore, the temporal resolution of these instruments is often limited to nanoseconds, a timescale longer than many important ultrafast phenomena. To investigate earlier time dynamics, and in particular dynamics in systems with non-radiative excited state decay, pump-probe spectroscopy is needed.

The ultrafast laser system employed in these studies consists of four major parts: an oscillator, generating a passively mode locked laser; a stretcher, temporally stretching the pulse width to avoid damaging optics; a regenerative amplifier, which amplifies the energy present in each laser pulse; and finally a compressor, which temporally compresses the pulse, allowing for experiments on sub-picosecond timescales to be conducted. Each of these components will be discussed in this section.

2.4.1 Mode-Locked Oscillator

In order to perform ultrafast pump-probe experiments, a pulse train must first be generated. This can be achieved with a mode-locked oscillator.

An electromagnetic field can only exist in a cavity when the wave propagating in one direction adds constructively with the wave propagating in the reverse direction. This superposition of waves means that only certain modes are permitted to exist within the cavity. In particular, the wavelengths of each mode must posses a node at the ends of the cavity.[57] This is known as the phase condition, and can be mathematically expressed in Equation 2.6.

$$\lambda_n = \frac{2l}{n} \tag{2.6}$$

Here. λ_n are the allowed wavelengths satisfying the boundary condition, l is the length of the cavity, and n is an integer.[58,59] The angular frequency of each mode w_n is then given by Equation 2.7.

$$\omega_n = \frac{\pi c n}{l} \tag{2.7}$$

The frequency spacing between longitudinal modes n and $n+1$ can be easily calculated.[60]

$$\Delta\omega = \frac{\pi c}{l} \tag{2.8}$$

The electromagnetic field $E(t)$ arising from $2n+1$ equally spaced longitudinal modes of

frequency ω is given by Equation 2.9.

$$E(t) = \sum_{q=-n}^{n} E_q e^{i[(\omega_0 + q\Delta\omega)t + \phi_q]} \tag{2.9}$$

Here, E_q is the amplitude and ϕ_q the phase of mode q. Normally, the phase of each mode is random, leading to constructive and destructive interference randomly, resulting in continuous wave (CW) operation. If the phase relationship between modes was not random, but instead fixed to some constant phase relationship, then the electric field would periodically interfere constructively at one point in time and destructively at all other points in time, causing the output to appear as a pulse. The phases of the modes in the output beam are said to be locked provided the condition in Equation 2.10 is met.

$$\phi_q - \phi_{q-1} = \phi \tag{2.10}$$

The value of ϕ must be a constant for this condition to be met. If the phases are mode locked, then a pulse will be generated with a period given by $T = 2l/c$. There are two general categories of techniques by which mode-locking is achieved in ultrafast systems: active mode locking and passive mode-locking.

In active mode-locking, an externally driven intracavity loss modulator is driven at a frequency $\omega_m = 2\pi/T$ which corresponds to the longitudinal mode spacing of the laser, where T is the round trip pulse transit time within the cavity. By switching to a low loss

mode at frequency ω for only a short time interval, and then operating at a high loss mode all other times, the modulator essentially acts as a periodic shutter, permitting one pulse per round cavity round trip. Lasing will only occur when the phases are mode-locked, and the laser will not operate in a CW mode.[61]

Passive mode locking makes use of nonlinear optical effects which induce modulation internally. One such example, and the means by which the laser used in these experiments is mode-locked, is through the use of Kerr-lens mode-locking. As the name suggests, Kerr-lens mode-locking makes use of the optical Kerr effect.[62,63] The optical Kerr effect describes how the refractive index of a material varies with the intensity of the light passing through it.[64,65] The nonlinear refractive index n can be written according to Equation 2.11.

$$n = n_0 + n_2 \frac{|a(t)|^2}{A_{eff}} \tag{2.11}$$

The instantaneous power of the pulse is given by $|a(t)|^2$, A_{eff} is the effective area of the beam in the Kerr medium.[58] The greater the intensity of the light traveling through the material, the larger the change in the index of refraction. A laser beam with a Gaussian profile has a greater intensity at the center of the beam than the perimeter, and because most materials possess $n_2 > 0$, will experience a greater index of refraction at the center. This results in an effective gradient in the refractive index throughout the material and leads to self focusing of the beam. The higher intensities of pulsed mode-locked beams leads to them being more tightly focused than CW beams.

Hard-aperture Kerr-lens mode locking makes use of a slit or iris to physically block the CW mode.[58] In a soft-aperture set up, self-lensing and self-focusing influences the overlap of the lasing mode with the profile of the pump laser beam in the Kerr medium.[66] The self-focusing effect of the mode locked pulses increases the overlap with the pump beam, further increasing the net gain, while the CW mode does not overlap as substantially, and thus experiences reduced gain. The oscillator in the experiments conducted herein makes use of this soft-aperture means of Kerr-lens mode-locking.

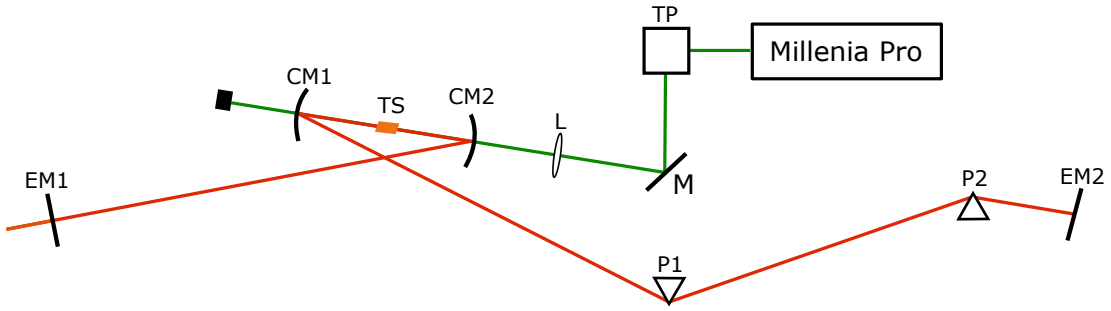

Figure 2.2: Schematic of the Ti:Sapph oscillator. TP: twisted periscope, M: 532 nm dichroic mirror, L: focusing lens, TS: Ti:Sapphire, CM1/2: focusing cavity mirrors, EM1: end mirror and output coupler, P1/2: fused silica prisms, EM2: end mirror.

A schematic of the oscillator is shown in Figure 2.2. A Millenia Pro (Spectra Physics, Nd:YVO_4) produces 1.9 W of continuous wave, s-polarized light centered at 532 nm, which

is then directed into a twisted periscope, raising the beam height and rotating the polarization to p-polarized. The beam is directed by a 532 nm dichroic and then a focusing lens into a 4 mm, Brewster cut, 0.25% doped titanium-sapphire crystal (Ti:Sapph), stimulating emission from the crystal. The lens is placed such that the focus of the beam will serve as a soft-aperture for Kerr-lens mode-locking. The emitted photons from the Ti:Sapph cycle back and forth throughout the cavity. Each pass in the cavity results in gain, as the emitted photons further stimulate emission. Dispersion is accounted for by passing the beam through a pair of prisms set approximately 53.5 cm apart, at an angle of incidence equal to the Brewster's angle.

In order to mode-lock the system, a slight jolt is given to the translation stage, on which prism 2 (P2) is mounted, in the direction perpendicular to the beam path. After the laser is modelocked. The repetition rate f is given by $f = c/2d$, where c is the speed of light, and d is the length of the cavity. The repetition rate f of the oscillator is normally 85 MHz. When the pulse hits the output coupler, a small portion is transmitted. Mode-locking typically increases the output power of the laser by 50% over that of the CW mode (100 mW increased to 150 mW), with a bandwidth of approximately 40 nm. The temporal width of each pulse from the oscillator is usually between 5-10 fs.

2.4.2 Pulse Stretcher

The output of the oscillator has low pulse energies (<2 nJ/pulse) which are insufficient for the energy requirements for the the ultrafast experiments we wish to conduct. In order to

achieve sufficient pulse energy, the output must be amplified; however, because the pulses have a very short temporal width, amplification would result in instantaneous pulse energy greatly exceeding the damage threshold of the optics in the amplifier.[67] To overcome this limitation, the pulses must be temporally stretched.

Group velocity refers to the rate at which the modulation envelope of a pulse advances.[62,68] In normal dispersive media, pulses with higher frequencies (e.g. blue light) experience greater indices of refraction, thus traveling at slower group velocities than light of lower frequencies (e.g. red light).[65] Because the wave packet of the laser pulses consists of light of not just a single frequency, but a range of frequencies, the pulse will exhibit group velocity dispersion. The principles of group velocity dispersion can be employed to temporally stretch or compress the pulse. By increasing the distance traveled of high frequency light relative to low frequency light, the pulse can be stretched in time by generating positive group velocity dispersion, resulting in an up-chirped pulse. If, on the other hand, low frequencies are made to travel farther than high frequencies, negative group velocity dispersion is introduced, resulting in pulse compression and a down-chirped pulse.

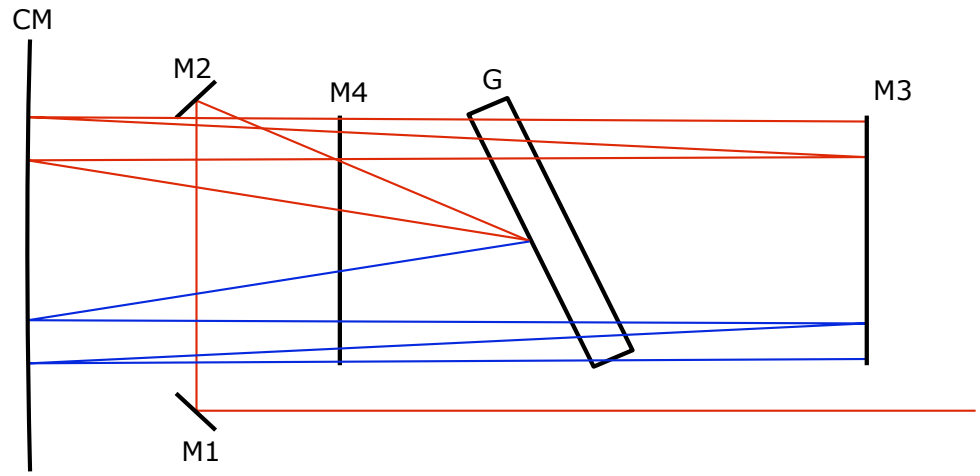

Figure 2.3: Schematic of the pulse stretcher. M1/2/3/4: flat mirrors, G: grating, CM: curved focusing mirror.

Figure 2.3 is a schematic of the pulse stretcher employed in the experiments conducted in this thesis.[69,70] All reflective optics are utilized in order to minimize higher-order aberrations in chirp introduced by transmissive optics such as lenses. The stretcher functions by temporally ordering the various wavelengths of light in an ultrashort pulse. The beam first comes in and is directed by mirrors M1 and M2 to the grating G. At the grating, the light is diffracted, separating the different frequencies of light. The light is directed to the curved focusing mirror CM, which in turn directs the light to the fold mirror M3. M3 directs the light back to CM, which reflects back towards G. The incident light is then sent to the retroreflector M4, which reverses (after a slight vertical displacement) the beam

path. The beam traverses back out the direction it came and can be picked off with another optic. The combination of the angle and spacing of G results in higher frequency photons traveling a longer distance than lower frequency photons. The stretched pulses will now no longer have an instantaneous power that, when amplified, would exceed the damage threshold of the optics.

2.4.3 Regenerative amplification

The output from the oscillator is directed into the regenerative amplifier (regen) after having been temporally stretched in the stretcher.[69,70] A schematic of the regen is depicted in Figure 2.4. The regen cavity consists of two focusing cavity mirrors (CM1 and CM2) coated to reflect 800 nm light while transmitting 527 nm light, and a flat end mirror (EM) coated to reflect 800 nm light. A 4 mm, Brewster cut, 0.25% doped titanium-sapphire crystal (Ti:Sapph) is employed as the gain medium (indicated by TS in Figure 2.4). The Empower 15 is an intracavity-doubled, Q-switched, diode-pumped Nd:YLF laser system that produces a pulsed 527 nm output beam. The beam is focused to a spot size of approximately 470 μm at the Ti:Sapph crystal, first by enlarging the beam waist with a telescoping lens pair (T), then focusing with a lens. The incident power prior to the Ti:Sapph measures 10 W. Light from the pump that is not absorbed by the Ti:Sapph is refocused on the crystal using a 527 nm dichroic focusing mirror, which further increases gain.

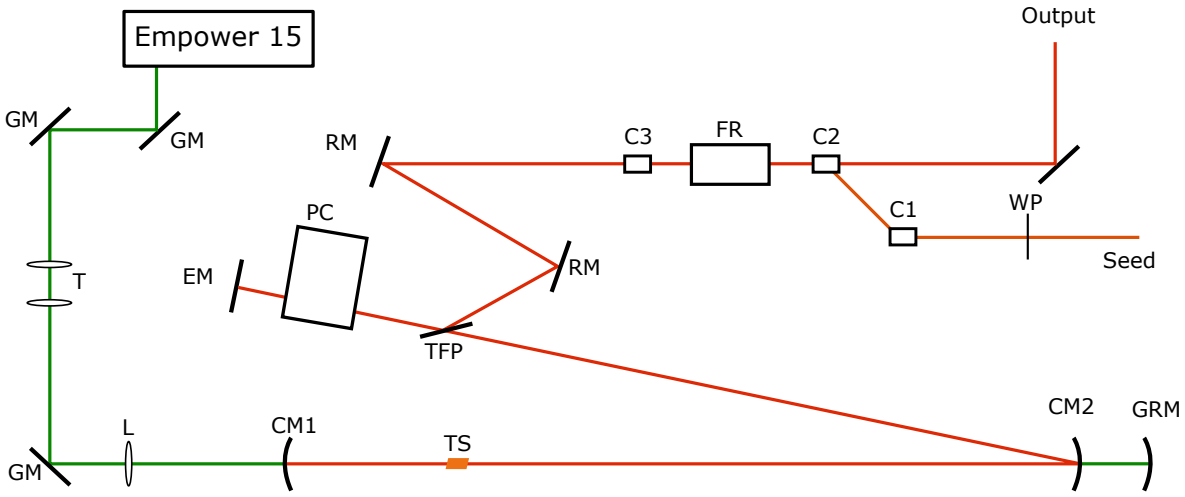

Figure 2.4: Schematic of the Ti:Sapph regenerative amplifier. GM: 527 nm dichroic mirrors, T: telescoping lens pair, L: focusing lens, CM1/2: focusing cavity mirrors, TS: Ti:Sapphire, GRM: 527 nm focusing dichroic mirror, TFP: thin film polarizer, PC, Pockels cell, EM: end mirror, RM: 800 nm dichroic mirrors, C1/C2/C3: polarizing cube beamsplitters, FR: Faraday rotator, WP: half waveplate.

The oscillator output (seed), having passed through the stretcher, is directed into the regen. The seed passes through a half waveplate, rotating the polarization from p-polarization to s-polarization. Two polarizing cube beam splitters (C1 and C2) direct the seed through a Faraday Rotator in the reverse direction, such that the polarization is not rotated.[62] A rotated polarizing cube beam splitter (C3) is placed to only permit s-polarized light to transmit, ensuring that the regen output polarization is fixed. The seed is then directed

towards a thin film polarizer (TFP) via a series of 800 nm dichroic mirrors (RM), before being reflected by the TFP in the direction of the end mirror.

A Pockels cell (Thales Laser MEDOX) is used to trap the laser within the cavity. When a high voltage (3.6 kV) is applied to the Pockels cell, light that passes through will experience a polarization rotation of 45°.[58,65] If a seed pulse reflects off the thin film polarizer and traverses through the Pockels cell while the voltage is applied, its polarization will be rotated twice: once on the way into the Pockels cell and once coming out, resulting in p-polarized pulses. The p-polarized pulse will then transmit through the TFP, and the voltage to the Pockels cell is switched off. The now p-polarized light is trapped within the cavity defined by the end mirror (EM) and the two cavity mirrors (CM1 and CM2). The pulse is amplified each time it passes through the Ti:Sapph crystal. After it has been sufficiently amplified, a voltage is again applied to the Pockels cell, rotating the polarization of the pulse back to s-polarization. The pulse will no longer transmit through the TFP, and instead reflects back through the Faraday rotator. Now traveling in the forward direction, the Faraday rotator will rotate the polarization 90° to p-polarization, allowing the beam to transmit through C2. The beam can then be directed out of the regen and into the compressor.

The result of the amplification is an 800 nm pulse train at a 1 kHz repetition rate, with approximately 1.2 W of power. The output of the regen is then sent into the compressor for pulse compression.[70,71]

2.4.4 Pulse Compressor

The output pulse of the regenerative amplifier is temporally up-chirped. A compressor is used to introduce negative group velocity dispersion to the pulses, causing the pulse envelopes of the different frequencies of light to temporally overlap.

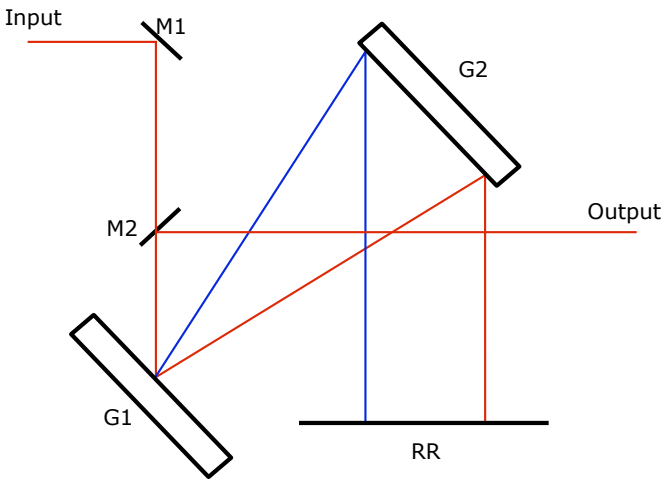

Figure 2.5: Schematic of the pulse compressor. M1: flat mirrors, G1/2: gratings, RR: retroreflector, M2: vertically displaced flat mirror.

A schematic of the pulse compressor employed is shown in Figure 2.5. The output of the regen is directed to the first grating G1 by the mirror M1. The grating is angled to diffract the light towards G2, which in turn diffracts the light (and by doing so, collimates the beam) towards the retroreflector RR. RR periscopes the beam vertically downwards, and then sends it back towards G2. The beam is then reassembled by G1, and picked off

by the vertically displaced mirror M2, which directs the pulse down the table for further experiments. The compressor set up accounts for not only the group velocity dispersion induced by the stretcher, but any induced by the optics in the regenerative amplifier as well.

After compression, the pulse has a spectral bandwidth (FWHM) of approximately 40 nm, a 1 kHz repetition rate, and approximately 650 μJ per pulse (due to the approximately 65% efficiency of the compressor), a nearly forty-thousand fold amplification over the oscillator per pulse output. Autocorrelation of the pulse usually gives pulse widths of 70-80 fs.

2.5 Pump-Probe Experiments

As mentioned in Section 2.4, pump-probe spectroscopy is a useful technique for probing ultrafast dynamics in organic systems. This section will focus on three topics: the physical phenomenon resulting in pump-probe signal, three-wave mixing and the generation of optical pulses of a specific frequency, and finally the experimental setup employed for data collection.

2.5.1 Sources of Pump-Probe Signal

Pump-probe spectroscopy (often referred to as transient absorption) is an ultrafast laser technique which can be used to monitor excited state dynamics.

A pump pulse is first incident upon the sample, which absorbs the photons in the pulse to generate excited states. A second pulse, which may be a single color or a broad continuum, follows. Photons from this pulse may be absorbed by molecules which are in either the ground or excited electronic states. Since there is absorption from both ground state and excited state molecules, we must compare the transmitted light to a reference beam in order to gain useful information. The pump pulse is chopped at half the repetition rate of the probe pulse. In effect, only every other probe pulse will have been directly preceded by a pump pulse. If the intensity of probe light transmitted through the sample is monitored, comparison of every other pulse allows for the determination of the influence of the pump on the transmitted light. By taking the negative log of the ratio of the intensity of light transmitted in the presence of the pump (I_{on}) to that of the intensity of light transmitted in the absence of the pump (I_{off}), we obtain a measurement analogous to the difference of two absorption measurements, ΔOD.

$$\begin{aligned} \Delta OD &= -\log\left(\frac{I_{on}}{I_0}\right) - \left(-\log\left(\frac{I_{off}}{I_0}\right)\right) = -\log\left(\frac{I_{on}}{I_{off}}\right) \\ &= OD_{on} - OD_{off} \end{aligned} \tag{2.12}$$

The intensity of light incident upon the sample is depicted here by I_0. In practice, I_0 need not be measured, as it will be canceled out as shown by Equation 2.12.

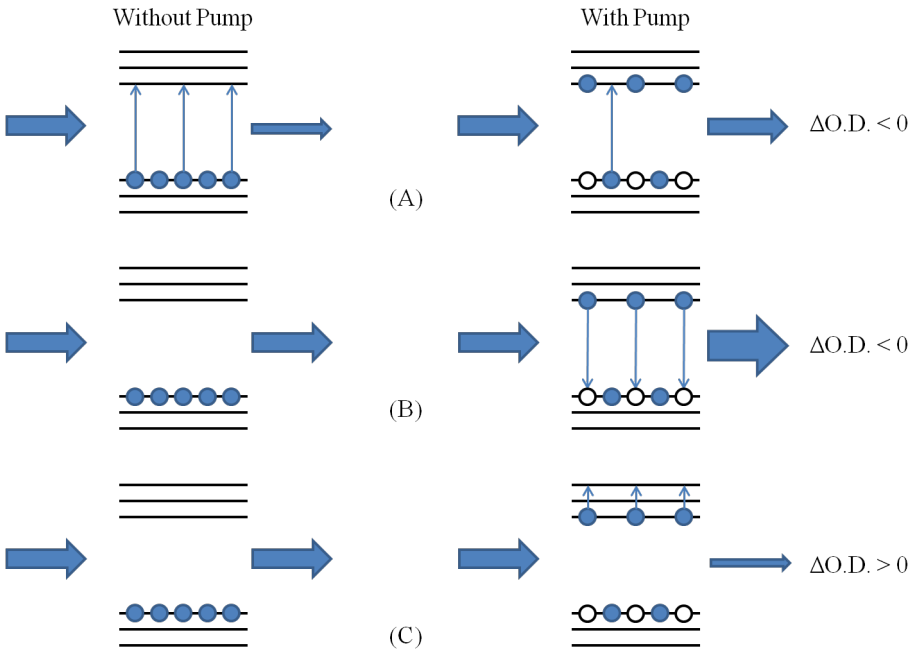

Figure 2.6: Sources of signal in pump-probe spectroscopy. A: ground state bleach, B: stimulated emission, C: excited state absorption.

There are three main features which contribute to changes in optical density: ground state bleach (GSB), stimulated emission (SE), and excited state absorption (ESA).[72] Prior to pump excitation, photons of a particular frequency from the probe pulse may be absorbed

by molecules in the ground electronic state. The pump beam will promote a population of chromophores in the system into the excited state. When the probe is now incident on the system, there are fewer chromophores present in the ground electronic state to absorb that particular frequency, thus a greater amount of light is transmitted with the pump than without it. Because I_{on} is greater than I_{off}, ΔOD is negative. This term is called a ground state bleach (GSB), and the term is often used interchangeably with ground state hole (GSH). In some cases, the probe beam may stimulate emission from excited chromophores. This is not possible without the pump, as no population yet exists in an excited electronic state. The emitted photons will reach the detector, making the intensity of light detected greater than without the pump. As in the case of a ground state bleach, the amplitude of ΔOD is negative. The final source of signal in pump-probe experiments is an excited state absorption, which occurs when molecules which have been promoted to an excited state due to the pump pulse exhibit absorption to a higher lying excited state. Since the excited states are absorbing photons which were not previously absorbed when the molecule was in the ground state, the amount of light transmitted through the sample decreases. I_{on} is less than I_{off}, resulting in a positive ΔOD. The measured pump probe signals will be a summation of all of the above signal sources (Figure 2.7). Because these signals are often overlapping, care must be taken to interpret ΔOD features correctly.

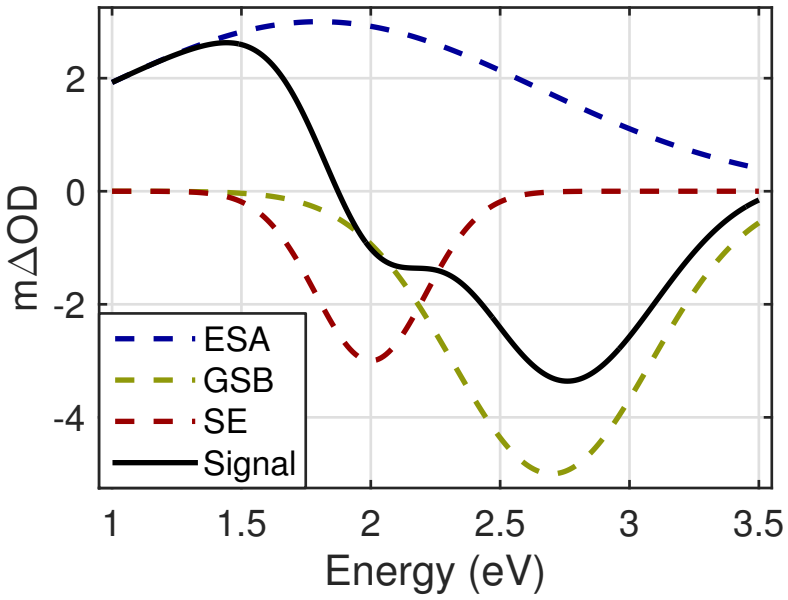

Figure 2.7: Simulated pump-probe spectrum depicting different contributions to the signal. The dashed lines depict individual sources while the black line depicts the summation of all sources.

The timing between the pump and probe pulses can be controlled. By delaying the probe beam, we can monitor changes in optical density as a function of time. Because the intensity of light transmitted depends on both the identity of the excited state as well as the population density of the excited state, information about the physical processes occurring can be gleaned. Kinetic models can be developed which predict the exciton population as a function of time. Figure 2.8 depicts an example of a pump-probe spectrum that might be obtained for the simple case of an excited state decaying directly to the ground state. The inset of Figure 2.8 depicts the decay of the amplitude of a transient absorption feature

as a function of probe delay. Excited state processes are usually not so trivial as to be represented by a single exponential, and often more complicated decay pathways emerge, such as vibrational relaxation within an excited state manifold, intersystem crossing to form triplets, charge-transfer, singlet fission, etc.

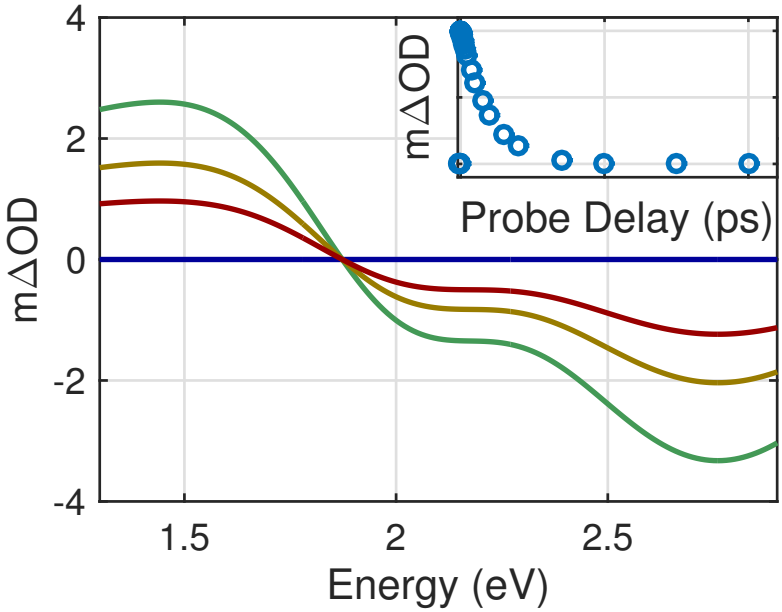

Figure 2.8: Simulated pump-probe spectrum as a function of probe delay time, with each delay time depicted by a different color line. The inset shows the decay of the signal amplitude as a function of probe delay.

2.5.2 Pump Generation

Optical excitation of molecules often requires specific wavelengths of light. Two techniques were primarily used to convert the 820 nm output of the laser system into other frequencies:

second harmonic generation (SHG), which can be used to generate 410 nm excitation pulses, and noncollinear optical parametric amplification (NOPA), which can be used to generate wavelengths between 470-680 nm.

Second Harmonic Generation

If an intense laser beam is incident on a transparent crystal, a new beam at twice the incident beam frequency may be generated. This nonlinear optical effect is an example of three-wave mixing and referred to as second harmonic generation (SHG).[60] For this process to occur, both energy and momentum must be conserved. This ultimately leads to the frequency and phase-matching conditions.

$$\begin{aligned} \hbar\omega_3 &= \hbar\omega_1 + \hbar\omega_2 \\ \hbar\mathbf{k}_3 &= \hbar\mathbf{k}_1 + \hbar\mathbf{k}_2 \end{aligned} \tag{2.13}$$

The angular frequency of the photon is represented by ω and $\mathbf{k}$ represents the wave vector. In a collinear geometry, the frequency-matching and phase-matching conditions may be rewritten according to Equation 2.14.

$$\begin{aligned} \omega_3 &= \omega_1 + \omega_2 \\ \omega_3 n_3 &= \omega_1 n_1 + \omega_2 n_2 \end{aligned} \tag{2.14}$$

The frequency matching conditions arise because of the dispersive nature of all materials, and thus the three waves travel at different velocities which correspond to their refractive indexes, n. Second harmonic generation is a degenerate case of three waving mixing, when $\omega_1 = \omega_2 = \omega$. This leads to a frequency-matching condition where $\omega_3 = 2\omega$. However, the phase-matching condition requires that the index of refraction experienced by ω_3 is equal to that of ω, that is $n(2\omega) = n(\omega)$.[68]

A birefringent material, that is, one where incident light experiences a different index of refraction depending on its polarization, is employed to overcome this apparent limitation.[58] Control of the indices of refraction is achieved by appropriate control of beam polarization and crystal orientation. One particular class of materials of interest are uniaxial crystals, which are characterized by an optical axis and frequency dependent ordinary (o) and extraordinary (e) refractive indexes ($n_0(\omega)$ and $n_e(\omega)$). An ordinary wave experiences an index of refraction $n(\omega)$ independent of the relative angle between the wave vector and the crystal optical axis, that is $n(\omega) = n_o(\omega)$. For an e-wave, the index of refraction $n_e(\omega, \theta)$ depends on the angle between the optical axis of the crystal and the wave vector according to the relation expressed in Equation 2.15.

$$\frac{1}{n_e^2(\omega, \theta)} = \frac{\sin^2(\theta)}{n_e^2(\omega)} + \frac{\cos^2(\theta)}{n_o^2(\omega)} \tag{2.15}$$

There are two types of uniaxial crystals, negative uniaxial crystals, for which $n_o(\omega) > n_e(\omega)$, and positive uniaxial crystals, for which $n_o(\omega) < n_e(\omega)$. In order to achieve phase-matching,

the polarization of the wave with frequency 2ω is selected such that its refractive index is the lower of $n_e(2\omega)$ and $n_o(2\omega)$. For a negative uniaxial crystal, the phase-matching condition is achieved with Type-1 three-wave mixing (defined as the higher frequency photon having orthogonal polarization to one of the lower frequency photons) in a negative uniaxial crystal, such as barium borate (BBO), requires that the lower frequency photons are ordinary beams. This is called Type-I o-o-e SHG (with o-o-e designating polarization for photons with frequency ω_1, ω_2, ω_3, respectively). In a positive uniaxial crystal, Type-I SHG is achieved with e-e-o polarization (with e-e-o designating polarization for photons with frequency ω_1, ω_2, ω_3, respectively). For collinear Type I SHG, the final conditions for phase-matching are summarized below.[62]

$$\begin{aligned} &\text{Type-I o-o-e SHG:} \qquad n_o(\omega) = n_e(2\omega, \theta) \\ &\text{Type-I e-e-o SHG:} \qquad n_e(\omega, \theta) = n_o(2\omega) \end{aligned} \tag{2.16}$$

Noncollinear Parametric Amplification

SHG can create light at frequency twice that of the fundamental. However, often neither the fundamental nor the result of SHG will provide satisfactory excitation of a sample. Optical parametric amplification is a technique which can be used to generate pump pulses over a wide range of visible frequencies of light.

In optical parametric amplification (OPA), three wave mixing between a high frequency, high intensity pump beam (frequency ω_p) and a lower frequency, lower intensity signal

beam (frequency ω_s) results in amplification of the signal beam. A third idler beam is also generated (frequency ω_i), satisfying the relationship $\omega_i < \omega_s < \omega_p$. Like in SHG, energy and momentum conservation must be maintained.[73]

$$\begin{aligned} \hbar\omega_p &= \hbar\omega_s + \hbar\omega_i \\ \hbar\mathbf{k}_p &= \hbar\mathbf{k}_s + \hbar\mathbf{k}_i \end{aligned} \tag{2.17}$$

The wave vectors of the pump, signal, and idler, are $\mathbf{k}_p$, $\mathbf{k}_s$, and $\mathbf{k}_i$, respectively. In noncollinear optical parametric amplification (NOPA), the angle between the direction of the pump and signal wave vectors is not 0. The vectorial phase-mismatch can be decomposed into components parallel and perpendicular to $\mathbf{k}_s$ according to the diagram in Figure 2.9 and expressed in Equation 2.18.[73,74]

$$\begin{aligned} \Delta k_{\parallel} = 0 &= k_i \cos(\Omega) + k_s - k_p \cos(\Psi) \\ \Delta k_{\perp} = 0 &= k_i \sin(\Omega) - k_p \sin(\Psi) \end{aligned} \tag{2.18}$$

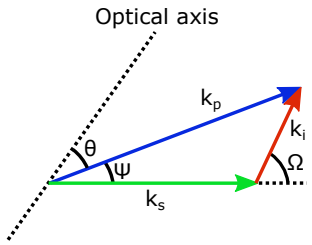

Figure 2.9: Phase-matching conditions for NOPA. k_p: pump wave vector, k_s: signal wave vector, k_i: idler wave vector, Optical axis: BBO optical axis, θ: angle between k_p and optical axis, Ψ: angle between k_p and k_s; Ω: angle between k_i and k_s.

The noncollinear geometry, coupled with choice of polarization, relative angles between the pump and signal, and optical axis can be used to achieve the frequency and phase-matching conditions. Efficient phase-matching occurs with a BBO optical axis cut at 27.3°, allowing for generation of a large bandwidth pulse capable of compression to less than 10 fs.[50]

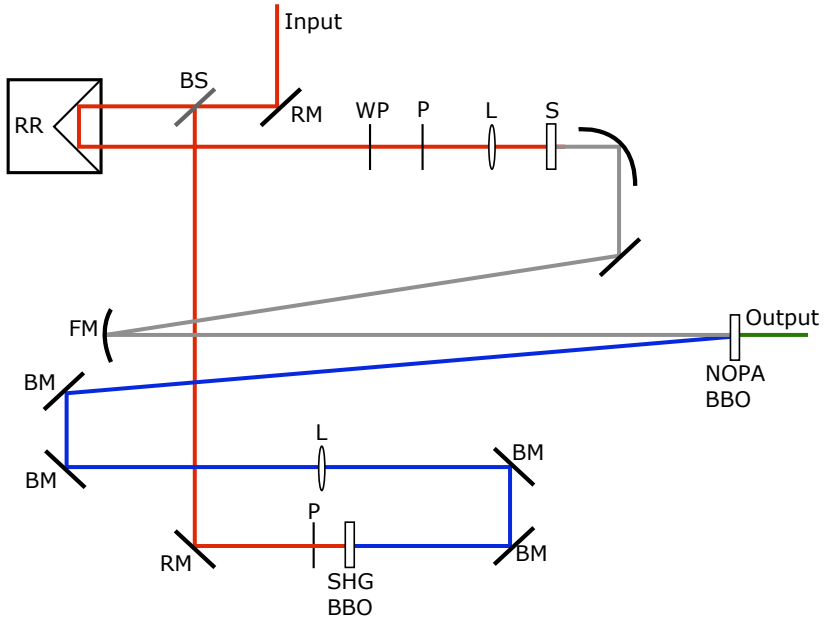

Figure 2.10: Schematic of the NOPA. RM: 800 nm dichroic mirror, BS: beam splitter, RR: retroreflector, WP: half waveplate, P: grid polarizer, L: focusing lens, S: sapphire, FM: focusing mirror, SHG BBO: BBO for 800 nm to 400 nm SHG, BM: 400 nm dichroic mirrors, NOPA BBO: BBO cut for NOPA between white light and 400 nm. Red lines indicate the 810 nm beam path, gray lines indicates the white light beam path, blue lines indicate the 410 nm beam path, green line depicts the amplified visible output beam.

A schematic of the NOPA employed in this work is shown in Figure 2.10. Input 820 nm p-polarized light is directed into the NOPA and split into the signal and pump using a beam splitter. The signal transmits through the beam splitter and into a retroreflector

mounted on a delay stage. The retroreflector can be manually translated in order to adjust the temporal overlap between the signal and pump beams. After exiting the retroreflector, the beam passes through a half waveplate and grid polarizer, rotating the polarization to s, which attenuates the beam. The beam then transmits through a 10 cm focusing lens and into a sapphire, generating a white light continuum. A parabola is used to collimate the beam, which is then reflected to a 50 cm spherical mirror. The spherical mirror focuses the white light into a specially cut BBO crystal (Newlight Photonics) for Type-I NOPA between visible and 410 nm light. The pump beam reflected off the beam splitter is directed through a polarizer and a BBO cut for 800 nm to 400 nm SHG (Newlight Photonics). The pump reflects off two 400 nm dichroic mirrors (BM) before passing through a lens with a 75 cm focal length. The remaining two mirrors are used to align the pump beam with the signal in the NOPA BBO. The focus of the pump is intentionally set after the NOPA BBO to reduce the likelihood of crystal damage and increase pump overlap with the signal. The NOPA BBO is mounted on a stage that permits the rotation of the crystal relative to the incident beams, which allows for the phase-matching angle to be tuned.

By adjusting the spatial and temporal overlap of the signal and pump, as well as the phase-matching angle, the NOPA can be tuned to generate an output with wavelengths ranging from 470-680 nm. A fused silica window can be placed in either the white light signal beam path or the pump path to temporally chirp each beam. By placing the window in the signal beam path, a narrow range of wavelengths will overlap temporally with the pump, generating a more narrow bandwidth of the amplified light. By chirping the

pump beam, a broader bandwidth of amplified light will result, as more wavelengths will temporally overlap with the now chirped pump.

The resulting output of the NOPA is sent through a prism pair set to the Brewster angle in order to compress the pulse.[74] Compression, as measured by cross-correlation between the 820 nm pulse and output NOPA pulse, typically results in 60 fs pulses.

2.5.3 Probe Generation

Equally important to pump generation in a pump-probe experiment is the generation of a probe beam. The 820 nm output of the laser is focused into a transparent condensed medium, such as sapphire or calcium fluoride (CaF_2). At sufficiently high input power and focus, a multitude of nonlinear effects result in the generation of a white-light continuum with the same polarization as the input pulse. Among the explanations for the continuum generation include multiphoton excitation, self-phase modulation, and self-steepening of the pulse as well as avalanche ionization within the optical medium.[75–77] The width of the continuum has been suggested to depend on the band-gap of the optical material. For the experiments conducted in this thesis, sapphire was chosen as the material for continuum generation, providing a broad spectrum ranging from approximately 420 nm into the near-IR region. On occasion, a CaF_2 window was employed, generating a broader continuum extending to approximately 350 nm.[77] The CaF_2 window is susceptible to laser burn-in and degradation, and must be continually translated so as to avoid these deleterious effects.

2.5.4 Pump-Probe Setup

A schematic of the pump-probe set up is shown in Figure 2.11. A signal from the regenerative amplifier is sent to a chopper wheel (New Focus 3501), which modulates the pump beem to a repetition rate half that of the laser (500 Hz). The pump and probe beams are sent down a set of boltholes straight into a retroreflector (PLX, Inc.) on motorized stages (Newport UTM150PP.1, controller ESP301). The retroreflectors can be translated forward and backwards by the stage, thereby increasing or decreasing the distance with which the pump and probe beams travel, and, consequently, when a pulse of light will reach the sample. Grid polarizers (Edmund Optics) are used to control the polarization of the light. A half waveplate is placed prior to the polarizers, allowing for the intensity of light selected by the polarizer to be modulated. If the pump is generated via SHG (400 nm light), dichroics are employed in place of the remaining three flat mirrors to remove excess 800 nm light from the laser line. A white light continuum is obtained by focusing the 800 nm light into either a sapphire crystal or CaF_2 window. A parabolic mirror is then positioned so that it collimates the incident white light. Both pump and probe beams are directed to a final parabolic mirror, which focuses and spatially overlaps both beams at the sample. After the sample, the pump beam is blocked to prevent stray scattered radiation from reflecting across any other optics. The probe beam is collimated with a lens. From here, it can be directed onto a diode (Thorlabs DET210) via a flip-up mirror, which can then be recorded with either a lock-in amplifier (Stanford Research Systems

SR830), or a low noise current preamplifier (Stanford Research Systems SR570). A band pass filter is placed in front of the diode to select for features at specific wavelengths.[78] For full frequency experiments, the probe beam is instead focused into a monochromator (Princeton Instruments SP2150, 150 g/mm grating) and detected with a 256 pixel silicon diode array (Hammamatsu, visible, 450-950 nm: S3901-25Q Si array with C7884-20 driver). The signal from the array is read out by a National Instruments data acquisition system (DAQ board NI: PCI-6132, conncetor block NI BNC-2110). The wavelength axis is calibrated using a series of calibrated band pass filters. To account for temporal chirp of the probe continuum induced by the solvent, cuvette, or sample substrate, the cross-phase modulation was measured at earlier times and fitted to the Sellmeier equations, allowing for the creation of a chirp-curve.

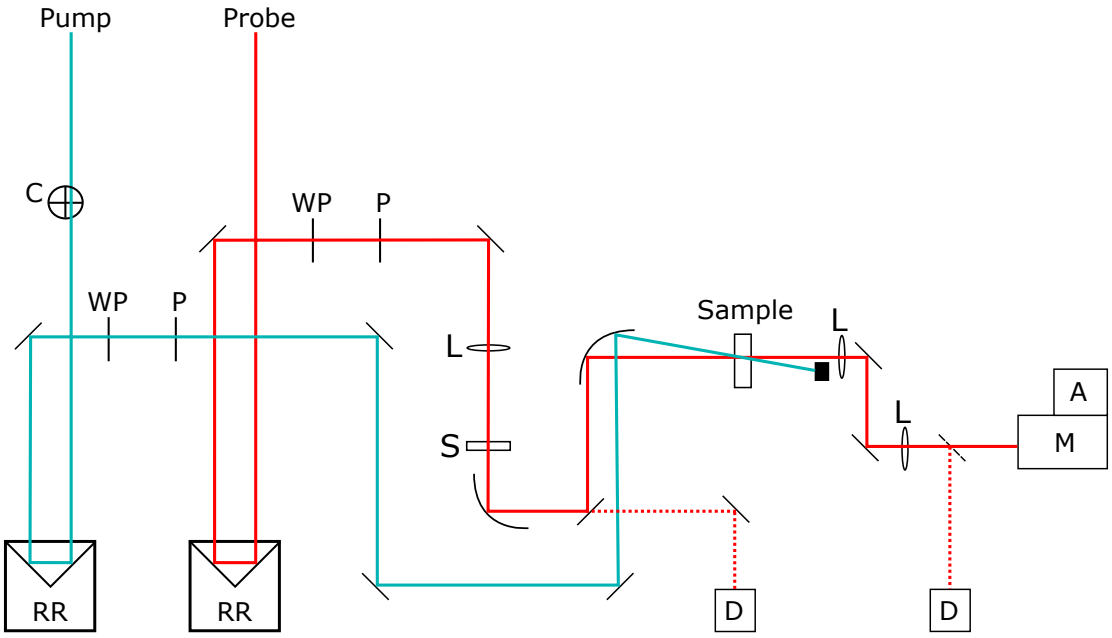

Figure 2.11: Schematic of the pump probe set up. Solid black angled lines depict flat mirrors, dashed black angled lines depict flip up mirrors, solid black curved lines depict parabolic mirrors. The pump beam path is depicted by the blue line, while the probe beam path is depicted by the red line. The dashed red line indicates the probe beam path when referenced photodetection methods were employed. C: chopper wheel, RR: retroreflector, WP: wave plate, P: polarizer, L: lens, S: sapphire, D: diode, M: monochromator, A: diode array.

Referenced Photodetection

Organic thin film samples are often particularly sensitive to high laser fluence, which results in nonlinear decay pathways such as exciton annihilation.[46,79] To mitigate this, low pump beam powers are desirable. However, the transient signal is proportional to the amount of light absorbed, and consequently the incident pump fluence. The Hammamatsu array used for full-frequency detection is not sensitive enough to detect transient signals when the response is very low. A referenced photodetection set up similar to that employed by Werley et al. was employed when experimental conditions warranted low pump fluences.[80] A block diagram of the set up is shown in Figure 2.12.

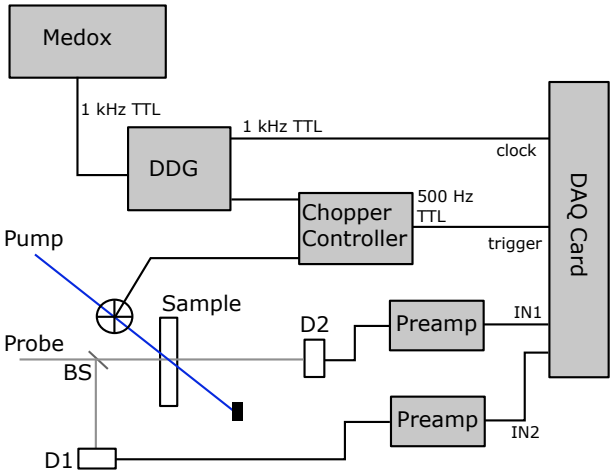

Figure 2.12: Block diagram of the referenced photodetection set-up. Medox: Timing control of regen, DDG: digital delay generator, BS: beam splitter, D1: photodiode 1, D2: photodiode 2, Preamp: SRS current preamplifier, DAQ Card: data acquisition card, IN1/2: analog input 1/2 from preamplifiers. Adapted from Werley et al.[80]

A 30-70 beamsplitter is placed in the probe line, sending 30% of the probe to photodiode D2 (Thorlabs, DET110) and the remaining 70% through the sample, which is ultimately directed to photodiode D1 (Thorlabs, DET110). In front of each diode was a matched 10 nm band-pass filter to select for features at specific wavelengths. A neutral density filter balanced the intensity of light incident upon each diode in the absence of the pump pulse. Each photodiode detects the laser signal and converts that signal to a time-dependent voltage which is amplified by a current preamplifier (SRS570, Stanford Research Systems).

The analog signal from the preamplifier is sent to DAQ card, where it is digitized.

The digital delay generator (DG535, Stanford Research Systems) provided the sample clock for the DAQ and the chopper controller. A TTL signal from the timing box of the regenerative amplifier (Medox) was sent to the digital delay generator (DDG) to synchronize it with the laser output. The timing of the DDG was set such that the rising edge of the output square wave coincided with the peak voltage of the preamp signal. The signal from the DDG was also used to control the chopper, which served as the trigger.

$$\frac{I_{on}}{I_{off}} = \left(\frac{D1_{on}}{D1_{off}}\right)\left(\frac{D2_{off}}{D2_{on}}\right) \tag{2.19}$$

where $D1_{on}$ and $D1_{off}$ are the signals recorded by D1 in the presence and absence of the pump, respectively, and $D2_{on}$ and $D2_{off}$ are the analogous quantities for D2. By referencing the signal to one another, temporal fluctuations in the white-light intensity can be canceled out, leading to a greater signal-to-noise ratio. The resulting ratio in Equation 2.19 can be used in Equation 2.12 to calculate changes in optical density. This results in an ability to detect transient signals at excitation densities on the order of 10^{-4} times that achievable via full-frequency detection using the photodiode array. It also permits much more rapid acquisition of single color decay dynamics, which is useful for samples subject to laser-induced photodegradation as it minimizes total exposure time.

A modified version of this set up can be employed for transient anisotropy measurements. In such an experiment, the beamsplitter before the sample is removed. After the

sample, a Wollaston prism is placed in the probe beam path, which separates the horizontal and vertically polarized light. The transmitted light of each polarization is directed to separate balanced diodes with matched bandpass filters. The polarization of the pump beam is set to 45° relative to that of the probe prior to incidence on the sample in order to interact equally with both polarization directions. The anisotropy $r(t)$ can be calculated from the following equation

$$r(t) = \frac{I_{\parallel}(t) - GI_{\perp}(t)}{I_{\parallel}(t) + 2GI_{\perp}(t)} \tag{2.20}$$

where $I_{\parallel}(t)$ is the intensity of the transmitted light with parallel polarization, $I_{\perp}(t)$ is the intensity of the transmitted light with perpendicular polarization, and G is an experimental correction factor which accounts for differences in detector response to the different polarizations of light.[56,81]

Chapter 3

Poly(thienylene)vinylene Statistical Copolymers: The Role of Composition on Excited State Dynamics

3.1 Introduction

Conjugated polymers are a rapidly emerging class of materials which are being increasingly investigated for applications in organic field effect transistors, light emitting diodes, and photovoltaics.[82,83] Many conjugated polymers are solution processable, which provides

an attractive and cost-effective manufacturing route for a number of applications.[84] A tandem polymer solar cell was recently created, with efficiencies exceeding for 8.6%.[85] One successful synthetic approach towards more efficient polymer solar cells has been the use of polymers with lower optical band gaps consisting of alternating electron rich and electron poor repeat units (sometimes referred to as donor-acceptor architecture).[86,87] In these "push-pull" polymers, hybridization between the HOMO of the donor and the LUMO of the acceptor results in a reduced band gap.[88,89] The push-pull nature of these polymers has been documented to facilitate intrachain electron transfer.[90]

To that end, statistical copolymerization has emerged as a synthetically facile way to create low band gap materials consisting of structurally and electronically different monomer units.[91,92] This technique also affords the additional advantage of allowing for the synthesis of non-stoichiometric compositions, as opposed to the traditional 1:1 alternating donor-acceptor structure.[93] Thiophene-benzothiadiazole repeat units have been employed in a variety of polymer systems to create a vast catalogue of interesting donor/acceptor conjugated polymers.[16,93–97] Poly(thienylene vinylene) devices report low power conversion efficiencies, often on the order of 1% or less.[92,98] Devices consisting of TBTV have been shown to possess 0.51% power conversion efficiency.[99,100]

Despite the promising PV performance of DA materials, less attention has been given to understanding the excited state photophysics of these materials compared to classic "neat" polymers such as P3HT and PPV.[101] Because the nature of the excitations in these complicated systems are not as well understood, the polymers we are studying can provide a

model system for understanding the nature of the interactions between donor and acceptor monomer units. Ultrafast pump-probe spectroscopy provides a means to examine exciton decay pathways due to both radiative and non-radiative transitions. Use of this technique will elucidate valuable information about the intramolecular decay processes occurring in polymers consisting of thienylene vinylene (TV) and thiophene benzothiadiazole thienylene vinylene (TBTV) monomer units. It is especially important to consider what effect the random organization of donor and acceptor units will have on the nature of the exciton generated upon light absorption.

3.2 Experimental

3.2.1 PTV Sample Preparation

PTV-TBTV polymers were obtained from the Hillmyer group and used without further purification. The structures of the polymers are shown in Figure 3.1. For all solution measurements, the polymers were dissolved in chloroform (Fisher Scientific, HPLC Grade, 99.9%) and degassed with argon. All measurements were collected on the same day the sample was prepared and no evidence of polymer degradation was observed.

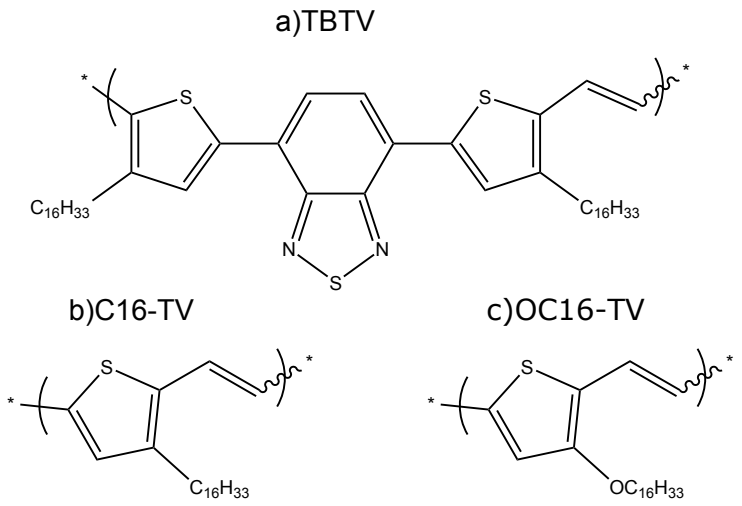

Figure 3.1: Structure of the monomer units comprising the polymers employed in this study. a) TBTV, b) C16-TV, c) OC16-TV.

Polymer	M_N (kg/mol)	PDI	Avg. Chain Length		
C16	33	2.2	87.2		
OC16	4	1.6	11.5		
TBTV	7	1.9	5.2		
% TBTV		C16 Series		Run C16-TV	Run TBTV
5	10	1.7	28.2	20	1.1
21	6	1.2	14.1	4.8	1.3
37	6	1.4	12.1	2.7	1.6
59	5	1.4	8.4	1.7	2.4
78	6	1.4	8.9	1.3	4.5
% TBTV		OC16 Series		Run OC16-TV	Run TBTV
22	3	1.1	6.8	4.5	1.3
45	4	1.2	7.4	2.2	1.8
77	4	1.2	5.9	1.3	4.3

Table 3.1: Physical description of the polymers employed in this study, including number average molecular weight (M_N), polydispersity index (PDI), average chain length (number of monomers) calculated from Equation 3.1, and average sequence length of monomer units calculated from Equations 3.4, and 3.5.

Because the monomer units are randomly distributed within a polymer, it is important to begin by attempting to understand what an average polymer chain might resemble. The average number of monomer repeat units n in a given polymer chain can be calculated by Equation 3.1,

$$n = \frac{M_N}{P_A M_A + (1 - P_A) M_B} \tag{3.1}$$

where M_N is the number average molecular weight of the polymer chains, P_A is the percentage of monomers of type A in the chain, and M_A and M_B are the molecular weights of the monomer repeat units A and B, respectively.[102] The polydispersity index (PDI) of a sample is a measure of the breadth of the distribution of polymer chain lengths. A monodisperse sample would possess a PDI of 1, while more typical reactions yield PDI closer to 2. The C16 series generally tends to have greater molecular weights than the OC16, albeit a broader distribution of polymer chain lengths as suggested by the PDI.

We can also obtain statistical information based upon how many of a given monomer unit will occur in a row in a given polymer chain (e.g. the number of monomer A in a row before encountering a monomer of B). The average value of a sequence length of monomer A, ν is given by

$$\bar{\nu} = 1 + r_A \frac{[A]}{[B]} \tag{3.2}$$

where r_A is the reactivity ratio, [A] is the concentration of A, and [B] is the concentration of monomer B in the feedstock.[102] An analogous equation can be constructed for monomer B

$$\bar{\mu} = 1 + r_B \frac{[B]}{[A]} \tag{3.3}$$

The copolymers employed in these experiments are close to ideal (the radical polymer chain will react with monomer A or B with equal probability), with $r_A \approx r_B = 1$. We can thus replace [A] and [B] with their relative percentages to obtain average sequence lengths. For monomer A, we obtain for the average sequence length $\bar{\nu}$

$$\bar{\nu} = 1 + \frac{P_A}{P_B} \tag{3.4}$$

Likewise, for monomer B we obtain the average run length $\bar{\mu}$

$$\bar{\mu} = 1 + \frac{P_B}{P_A} \tag{3.5}$$

3.2.2 UV/Vis Absorption and Photoluminescence

Absorption spectra of the polymers were collected using an Olis Cary 14 spectrophotometer. Polymer samples were suspended in chloroform with an absorption maximum of approximately 0.3 in a 1 cm quartz cuvette.

A SPEX Fluorolog 1680 0.2 m double spectrometer was used to collect photoluminescence spectra of the polymers at excitation wavelengths of 400 and 600 nm. Samples possessed an optical density in a 1 cm quartz cuvette of approximately 0.2-0.3 at the excitation wavelength. Coumarin 481 in ethanol was used as the reference dye for excitations at 400 nm while the dye Nile blue was used for excitation at 600 nm. The absorption of these references at the excitation wavelength were matched to the absorption of the sample to within 5%. The quantum yield ϕ_i of each of the polymers was calculated according to the following equation

$$\Phi_i = \Phi_r \frac{\int PL_i}{\int PL_r} \frac{A_{r,\lambda}}{A_{i,\lambda}} \frac{n_i^2}{n_r^2} \tag{3.6}$$

where Φ_r is the quantum yield of a reference, $\int PL_i$ and $\int PL_r$ are the integrated photoluminescence intensity of the sample and reference, respectively, $A_{i,\lambda}$ and $A_{r,\lambda}$ are the respective value of absorption for the sample and reference at the excitation wavelength λ, and n_i and n_r are the refractive indices of the sample and reference solvents, respectively.

3.2.3 Ultrafast Pump Probe

Ultrafast pump probe spectroscopy was performed using a home built Ti-sapphire oscillator, stretcher-compressor, and regenerative amplifier similar in design to one previously described.[70,71] The laser system produced 85 fs pulses at a 1 kHz repetition rate. For the pump, 800 nm light was passed through a doubling BBO, generating 400 nm light (3.1

eV). The probe pulse was obtained by focusing 800 nm light into a sapphire, generating a white-light continuum ranging from 1.7 to 2.8 eV. All experiments were conducted with the pump polarization set to the magic angle (54.7°) with respect to the probe polarization to isolate isotropic exciton dynamics. The pump was focused to a spot size of approximately 100 μm. Upon passing through the sample, the probe beam is collimated and directed into a Princeton Instruments SP2510i monochromator and detected with a 256 pixel diode array (Hamamatsu) with a resolution of 2 nm per pixel. The pump beam was mechanically chopped at half the repetition rate of the laser (500 Hz) while the probe beam was measured for every pulse. ΔOD, the change in optical density, was calculated for each pulse pair. ΔOD for each time delay between the pump and probe beam was found by averaging 25000 pulse pairs. Polymer samples were prepared in chloroform at concentrations which yielded an optical density of approximately 0.1 in a 1 mm quartz cuvette at the pump excitation wavelength of 400 nm. Samples were degassed immediately prior to data collection and sealed to prevent oxygen in the atmosphere from affecting exciton decay dynamics. The sample solution was flowed through a 1 mm quartz flow cell so as to prevent the accumulation of any photoproducts that might have formed within the sample window.

3.2.4 Ultrafast Anisotropy

Ultrafast anisotropy measurements were collected using a similar set up to that of the ultrafast pump-probe experiments. The pump pulse (400 nm) polarization was set to

45° relative to that of the probe polarization. After passing through the sample, the probe beam is collimated and passed through a Wollaston prism, separating the perpendicular and parallel components of the transmitted light. Each of the beams is then directed through a neutral density filter and then to a photodiode (DET210, Thorlabs) for detection. A set of matched filters (CVI) was used on each photodiode in order to monitor specific wavelengths. The neutral density filters were employed in order to match the intensity of the parallel and perpendicular polarized beams in the absence of any sample.

3.3 Results and Discussion

3.3.1 Steady State Measurements

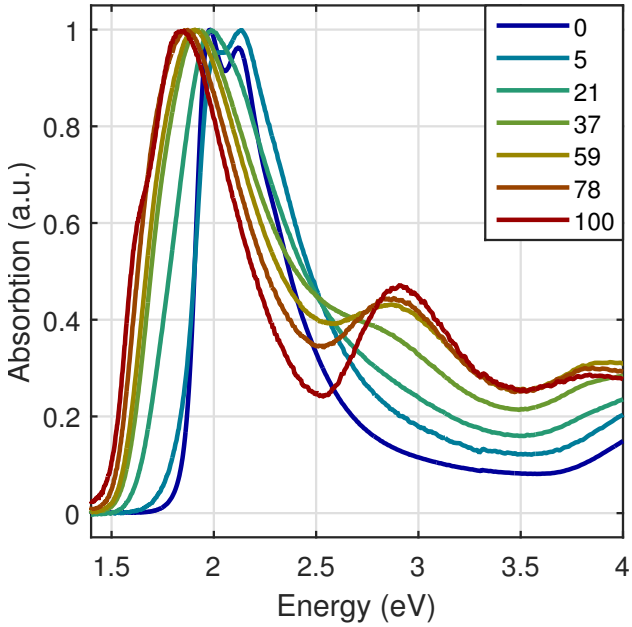

Figure 3.2: Steady-state absorption of C16-TBTV series. Polymers are labeled as percentage of TBTV monomer.

The absorption of the C16-TBTV series is shown in Figure 3.2. The polymer series features two prominent absorption features that change with increasing TBTV content: a peak centered at approximately 2 eV that shifts to lower energies and broadens, covering a larger portion of the solar spectrum, as the TBTV concentration is increased, and a peak centered at approximately 2.9 eV that grows in with increasing TBTV content. We note that the spectra of the ratios containing both C16 and TBTV monomers cannot be recreated as a

linear combination of the two neat polymers, indicative of orbital hybridization/interaction between the two monomer units. For the 0% and 5% TBTV polymers, there is a slight splitting of the 2 eV peak. This has previously been attributed to vibronic effects arising from polymer self-aggregation and folding.[103–106] It is also noteworthy that in the 100% TBTV sample, a shoulder appears at 1.7 eV, suggesting a change in the vibronic structure not present in any of the other polymers. Cyclic voltammetry measurements place the HOMO of 100% TBTV approximately 0.1 eV below the HOMO of the other polymers in this series, furthering the assessment of a different electronic environment in this polymer.[92].

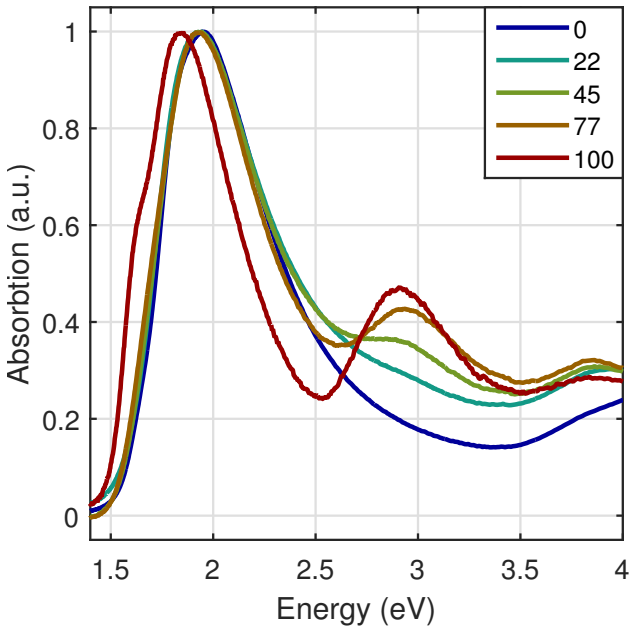

Figure 3.3: Steady-state absorption of OC16-TBTV series. Polymers are labeled as percentage of TBTV monomer.

The steady-state absorption of the OC16-TBTV series is shown in Figure 3.3. An absorption peak attributed to TBTV grows in at approximately 2.9 eV when the TBTV content is increased, similar to that of the C16-TBTV series, however, the peak centered at approximately 2 eV does not undergo the same shift observed in the C16-TBTV series. Only the 100% TBTV sample possesses an absorption band shifted from that of the other polymers.

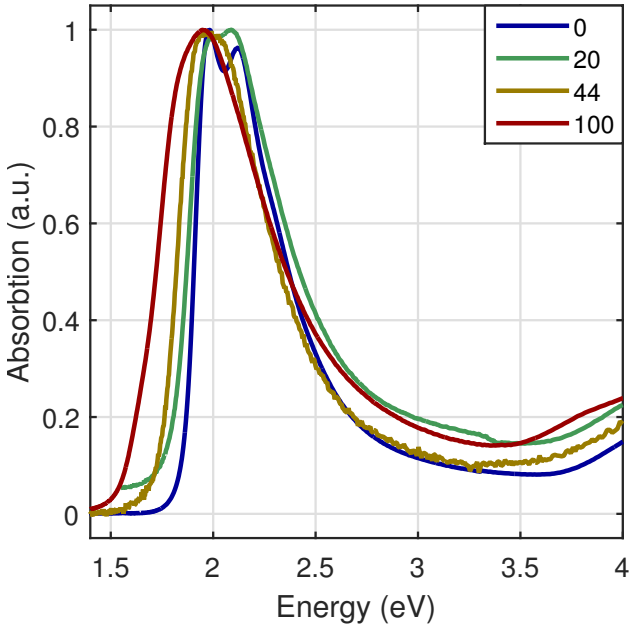

Figure 3.4: Steady-state absorption of C16-OC16 series. Polymers are labeled as percentage of OC16 monomer.

Figure 3.4 shows the absorption of several polymers in the C16-OC16 series. The spectra undergo only a slight shift as OC16 content is increased, and the spectral widths

remain relatively constant.

Fluorescence measurements were also collected for each of the polymer series. However, negligible fluorescence was detected for all of the polymer samples except for 100% TBTV. Measured quantum yields did not exceed 0.02% for any of the polymers, which is within the error of our detection equipment. These results are largely consistent with previous measurements of PTV photoluminescence. Emissive PTVs were created by the addition of electron-withdrawing alkylsulfanyl groups.[107]

3.3.2 Ultrafast Pump Probe

The full-frequency transient absorption spectra obtained from 400 nm photoexcitation are shown in Figures 3.5-3.11 below for the indicated polymer. The negative of the steady-state absorption spectra is overlayed on the transient spectra and plotted as the dashed black line. The spectra are all similarly featured, each with a negative ground state hole arising from depopulation of the ground state (which overlaps well with the steady state absorption), and an excited state absorption most prominent at lower energy wavelengths. As the TBTV ratio is increased, and the steady-state absorption red-shifted, the overlap between the excited state absorption and the ground state absorption increases, causing the ESA to appear to shift to lower energy as the ratio is increased. Most of the transient signal is gone by 500 ps, indicating the absence of any triplet excitons which are typically characterized by long-lived, slowly decaying features.

As the probe delay is increased, the transient signals decay uniformly. The shape of

the transient spectra are relatively time invariant. For each polymer, the ESA decays at the same rate as the GSH is recovered, suggesting that the kinetics underlying the change in signal are correlated between the two. This implies a simple physical model: excitation to an excited electronic state which then decays, directly repopulating the ground state.

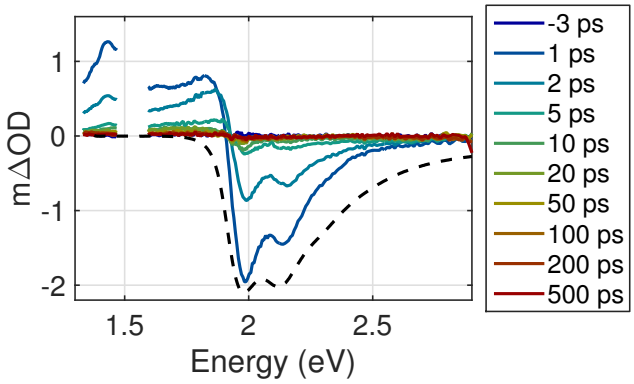

Figure 3.5: Full-frequency pump probe spectra of 0% TBTV upon 3.1 eV photoexcitation.

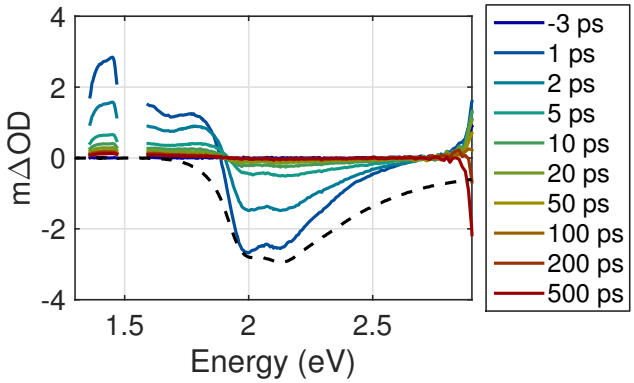

Figure 3.6: Full-frequency pump probe spectra of 5% TBTV upon 3.1 eV photoexcitation.

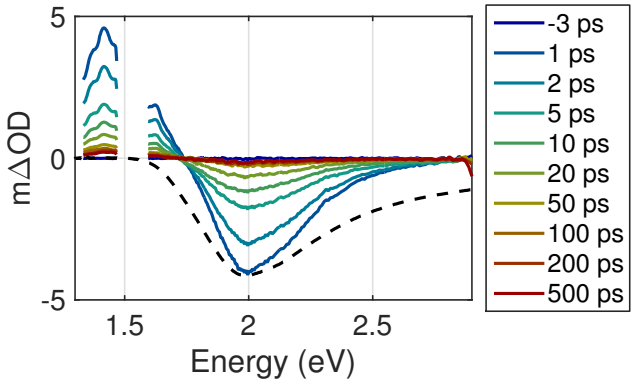

Figure 3.7: Full-frequency pump probe spectra of 21% TBTV upon 3.1 eV photoexcitation.

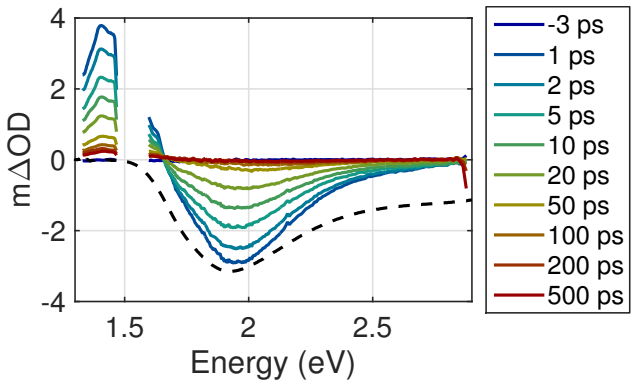

Figure 3.8: Full-frequency pump probe spectra of 37% TBTV upon 3.1 eV photoexcitation.

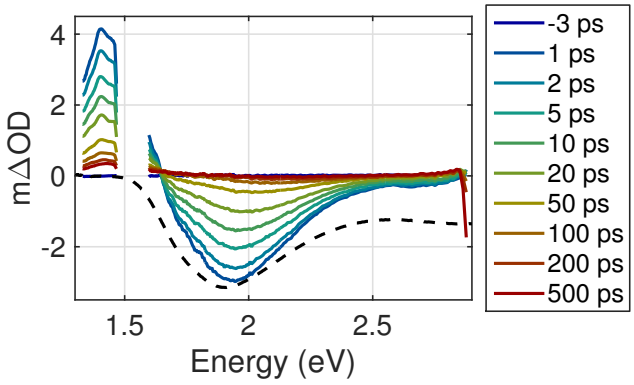

Figure 3.9: Full-frequency pump probe spectra of 59% TBTV upon 3.1 eV photoexcitation.

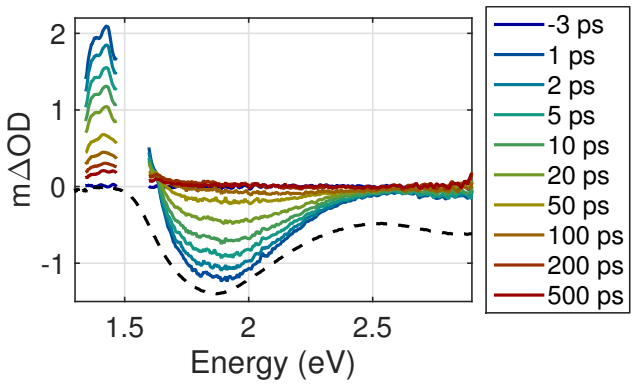

Figure 3.10: Full-frequency pump probe spectra of 78% TBTV upon 3.1 eV photoexcitation.

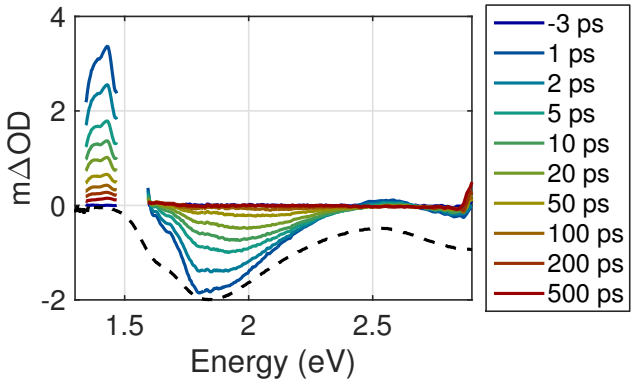

Figure 3.11: Full-frequency pump probe spectra of 100% TBTV upon 3.1 eV photoexcitation.

The decays of the transient absorption features are not well characterized by a single exponential for any of the polymer ratios except 0% TBTV. In order for the data to be adequately fit, multiple exponential terms are required, often with 6 or more free fitting parameters. Models with many terms may obscure information about the system, as overfitting can decrease the confidence with which one knows any single parameter. An alternative approach is to fit the data using models with fewer fitting parameters. One such function that provides adequate fitting to the decays is that of the stretched exponential, which takes the form given by

$$S(t) = Ae^{-(\frac{t}{\tau_s})^{\beta}} \tag{3.7}$$

for $0 < \beta \leq 1$.[108] In the case of $\beta = 1$, S(t) converges to a simple exponential decay,

with a characteristic lifetime τ_s. For values of $\beta < 1$, the decay is stretched, decaying more rapidly than a single exponential at t$< \tau_s$ and more slowly than a single exponential at t$> \tau_s$.

The stretched exponential has often been used to model relaxation in glasses and polymer dynamics such as rotational diffusion.[109–111] It has also been used for describing luminescence decay in solids and polymers.[112–115] Figure 3.12 plots the normalized signal amplitude from within each polymer excited state absorption, as well as the associated stretched exponential fit.

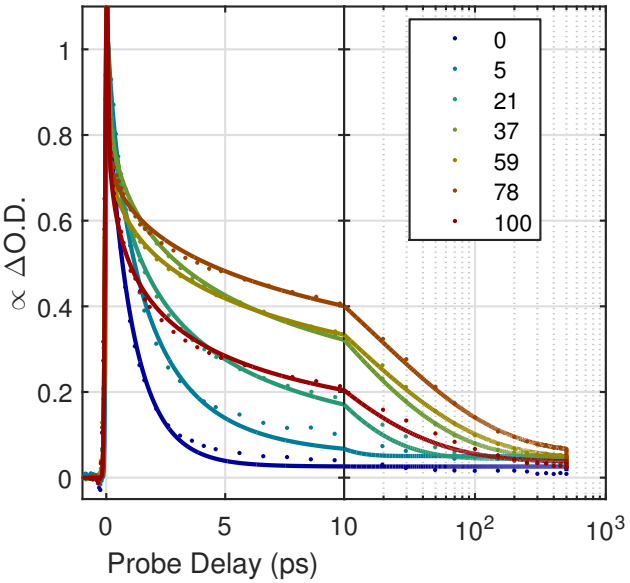

Figure 3.12: The normalized signal amplitude of the ESA feature from each of the C16-TBTV polymer ratios after 400 nm photoexcitation. Note that the x-axis changes from a linear scale to a logarithmic scale at 10 ps. Stretched exponential fits are shown as solid lines of the same color as the data points.

The 0% TBTV sample decays quickly, and by 10 ps nearly all of the signal has decayed. As the ratio of TBTV is increased, the transient feature decays at a slower rate, with the 78% TBTV sample possessing the slowest apparent decay. The 100% TBTV sample breaks this trend, appearing to decay at a rate similar to that of 21% TBTV.

To quantitatively compare the decay rates between the different ratios, an average

lifetime can be calculated using the fit parameters from Equation 3.7.

$$<\tau>= \frac{\tau_s}{\beta}\Gamma(\frac{1}{\beta}) \tag{3.8}$$

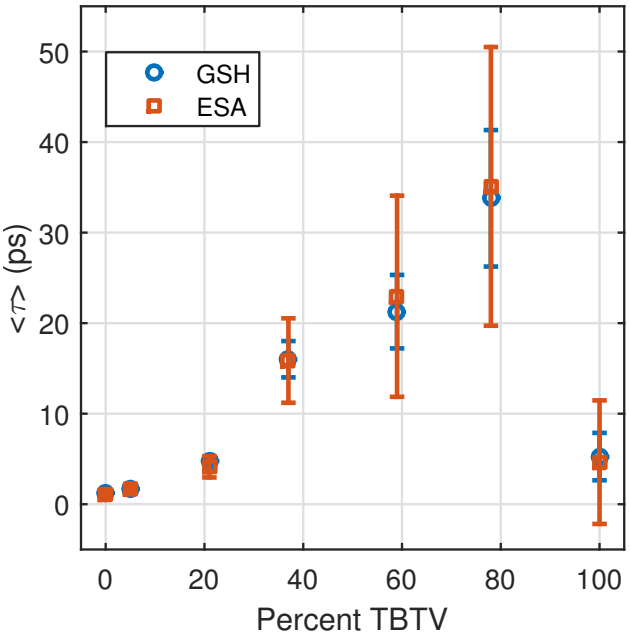

Figure 3.13: A plot of $<\tau>$ vs percent TBTV for the C16-TBTV polymer series upon 400 nm photoexcitation.

Figure 3.13 depicts the value of $<\tau>$ obtained for each polymer ratio of C16-TBTV. The value of $<\tau>$ from the fits to the GSH recovery are shown as blue circles, and the value of $<\tau>$ from the fits to the ESA are shown as the red squares. The error bars in the above plot are obtained by generating a distribution of $<\tau>$ using a random, normal

distribution of parameters τ_s and β constrained by the fitting confidence intervals. The resulting distrubtion is then fitted by a Gaussian, and the resulting value of σ used as the error bars. As a result, these error bars are likely to underestimate the confidence for which the parameter is calculated. The value $<\tau>$ calculated from the GSH decay and ESA decay agree well for each of the polymers, again suggesting a correlated decay pathway. For 0% TBTV, $<\tau>$ of 1.1 ps agrees well with previous literature measurements for the lifetime of neat PTV in solution.[103,116] The trend observed in the transient decays is again reflected here, with the 78% TBTV polymer possessing the longest $<\tau>$ of approximately 34 ps, and 100% TBTV possessing a $<\tau>$ similar to that of 21% TBTV.

There are several interpretations to the physical meaning of a stretched exponential.[117,118] One interpretation considers β to be indicative of the heterogeneity of the system, with lower values corresponding to a more heterogeneous systems, consisting of a broad distribution of decay rates. In other words, the stretched exponential decay is a superposition of many single exponential decays. For a transient signal modeled by Equation 3.7, there is some distribution of exciton lifetime τ, given by $\rho(\tau)$, for which S(t) can also be expressed

$$S(t) \propto \int_0^\infty \rho(\tau) e^{-(\frac{t}{\tau})} d\tau = \int_0^\infty g(k) e^{-kt} dk \tag{3.9}$$

where k=1/τ. In order to understand our system, knowledge of $\rho(\tau)$ (or rather $g(k)$)

is desired. $\rho(\tau)$ is related to $g(k)$ by the expression

$$\rho(\tau) = \frac{1}{\tau^2} g(k) \tag{3.10}$$

The $1/\tau^2$ term is a dominant feature in $\rho(\tau)$, which has the effect of masking any graphical distinctions that may be observed by comparing $\rho(\tau)$ from the different polymer ratios. It is more instructive to consider the distribution in terms of the decay rate, k, for which the distribution assumes a more conventional shape.

The Laplace transform of a function $f(t)$ is defined as

$$\mathcal{L}\{f(t)\} = \int_0^\infty f(t)e^{-st}dt \tag{3.11}$$

If we say that an equation $F(t)$ is the Laplace transform of some function $f(t)$, then the mathematical operation known as the inverse Laplace transform of $F(t)$ yields $f(t)$, that is

$$\mathcal{L}^{-1}\{F(t)\} = f(t) \tag{3.12}$$

By performing an inverse Laplace transform on a stretched exponential given by Equation 3.7 we obtain the distribution function $g(k)$.

$$\mathcal{L}^{-1}\{e^{-(\frac{t}{\tau_s})^\beta}\} = g(k) \tag{3.13}$$

This provides us with information as to the proportion of polymers within the system decaying at a given decay rate k. The functional forms of the distribution are only determinable analytically for select values of β, for example, $\beta = 0.5$. For other values of β, numerical methods are necessary.

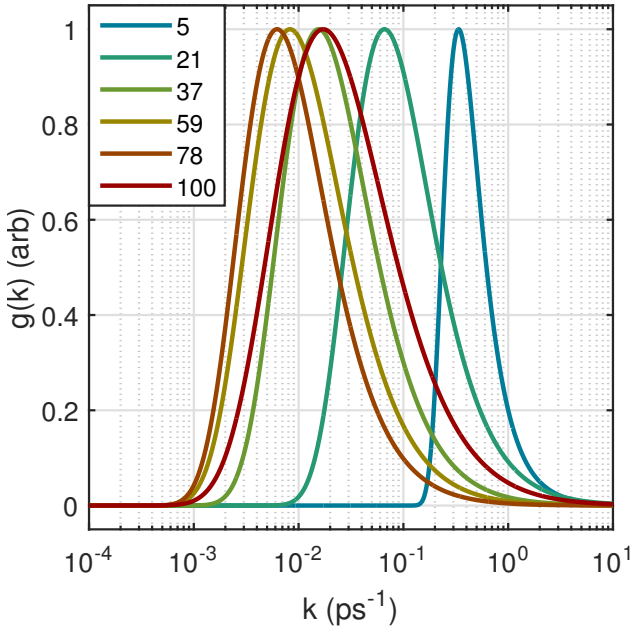

Figure 3.14: The distribution function g(k) vs k, scaled to a value of 1 at the most probable decay rate, for the stretched exponential fits to the C16-TBTV ESA decays.

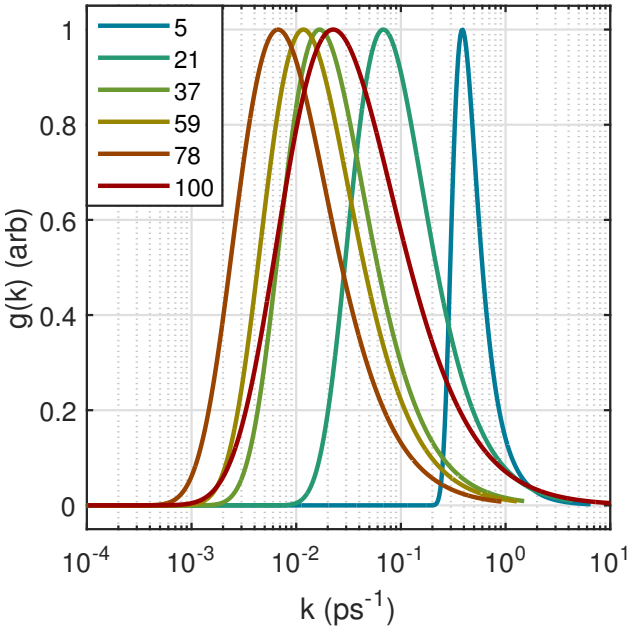

Figure 3.15: The distribution function g(k) vs k, scaled to a value of 1 at the most probable decay rate, for the stretched exponential fits to the C16-TBTV GSH decays.

Figure 3.14 depicts the distributions g(k) for each of the polymer compositions using the ESA decay fitting parameters. Figure 3.15 depicts the distributions g(k) for each of the polymer compositions using the GSH fitting parameters. The neat C16 solution (0% TBTV), is not depicted, as the distribution converges to a delta function centered around 1 ps^{-1}. The distributions are similar when performed for the ESA and GSH fits, as would be expected due to the correlated nature of the relaxation and recovery processes. We note that the distributions shift towards a maximum probability at slower decay rates as the proportion of TBTV increases. The distributions also broaden significantly, a feature

which is somewhat obscured by the logarithmic scale of Figures 3.14 and 3.15. The 100% TBTV sample has a peak comparable to 37% TBTV, but the distribution is much broader. More of the polymers in the system are decaying at faster rates. The broader distribution of rates is consistent with the polymer size distributions and chain lengths presented in Table 3.2.1.

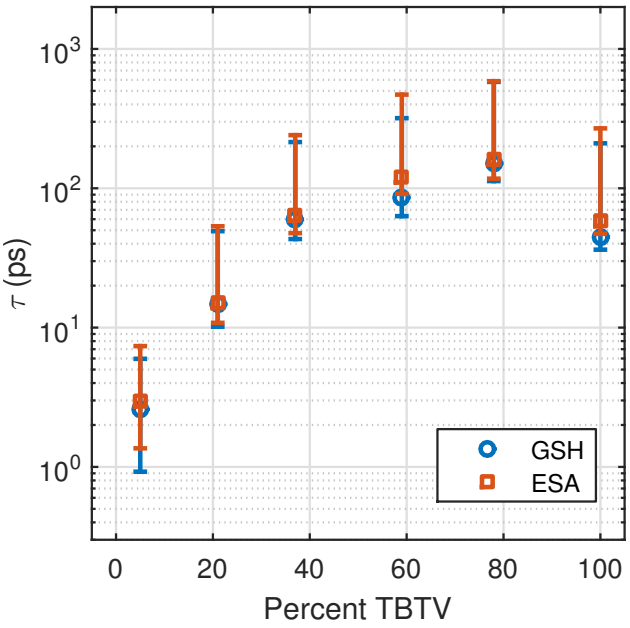

Figure 3.16: A plot of the value of τ correlating to the value of k for which the corresponding distribution function g(k) achieves a maximum. The bars depict the values of τ corresponding to k where g(k) is equal to half of the maximum value. The values for the distributions corresponding to the GSH fits are plotted as the blue circles, while the values corresponding to the ESA fits are plotted as the orange squares.

Note that the axis for k is plotted on a log scale, and that the distributions are actually asymmetric, with tails skewed towards long decay times (or rather slow decay rates). This is demonstrated in Figure 3.16. For each polymer ratio, the value of τ corresponding to the value of k for which g(k) reaches a maximum is plotted as an open circle (GSH distribution, blue) or open square (ESA distribution, orange). The error bars indicate the values at which the distribution reaches half of the maximum amplitude.

In the experiments above, photoexcitation occurred at 3.1 eV (400 nm). As seen in Figures 3.2 and 3.3 the polymer absorption at that wavelength is largely due to increased TBTV content. If an exciton localized on a TBTV monomer possessed longer average lifetimes than one localized on a TV monomer, one potential explanation for the increased lifetimes could then be preferential excitation of excitons localized on the TBTV component.

To determine whether this might be the case, pump-probe experiments were also conducted using 2.2 eV (560 nm) pump excitation. This photon energy is within absorption bands present both in TV and TBTV, and should therefore be less susceptible to preferential excitation.

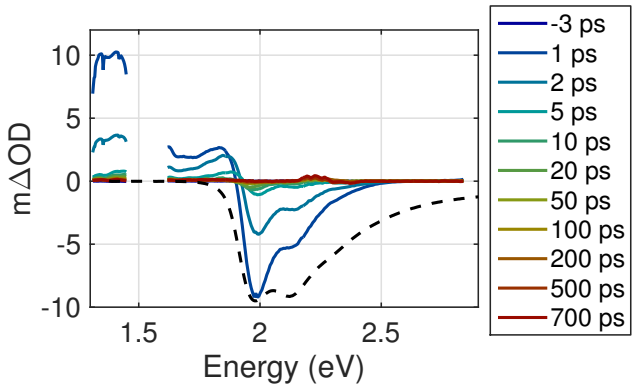

Figure 3.17: Full-frequency pump probe spectra of 0% TBTV upon 2.2 eV photoexcitation.

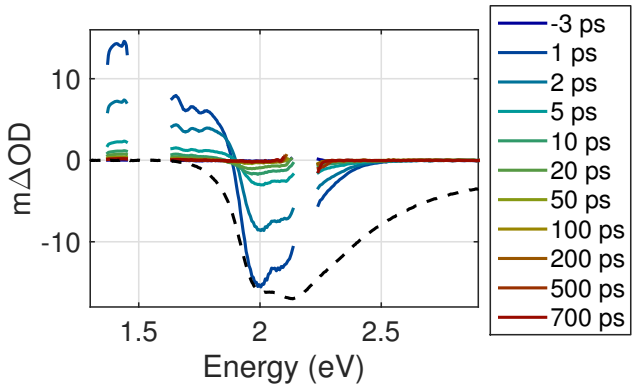

Figure 3.18: Full-frequency pump probe spectra of 5% TBTV upon 2.2 eV photoexcitation.

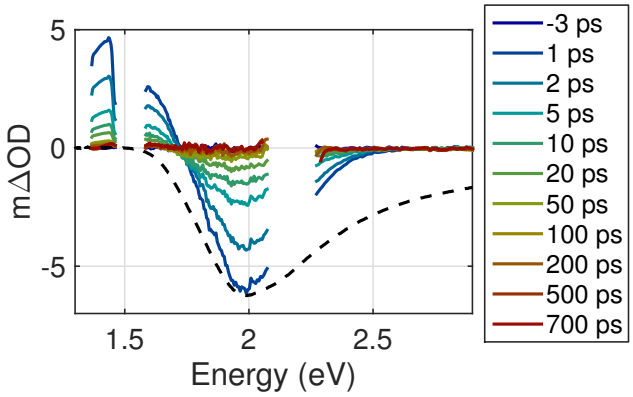

Figure 3.19: Full-frequency pump probe spectra of 21% TBTV upon 2.2 eV photoexcitation.

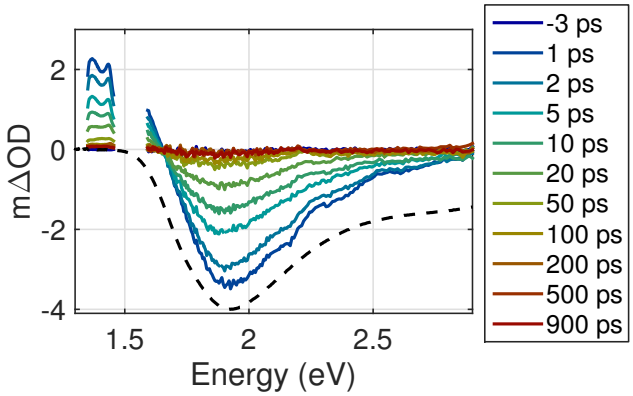

Figure 3.20: Full-frequency pump probe spectra of 37% TBTV upon 2.2 eV photoexcitation.

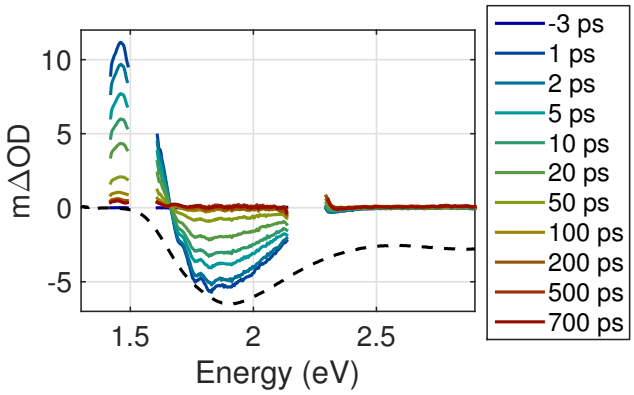

Figure 3.21: Full-frequency pump probe spectra of 59% TBTV upon 2.2 eV photoexcitation.

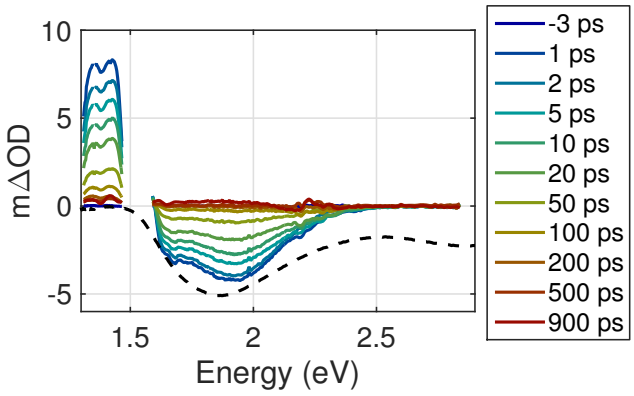

Figure 3.22: Full-frequency pump probe spectra of 78% TBTV upon 2.2 eV photoexcitation.

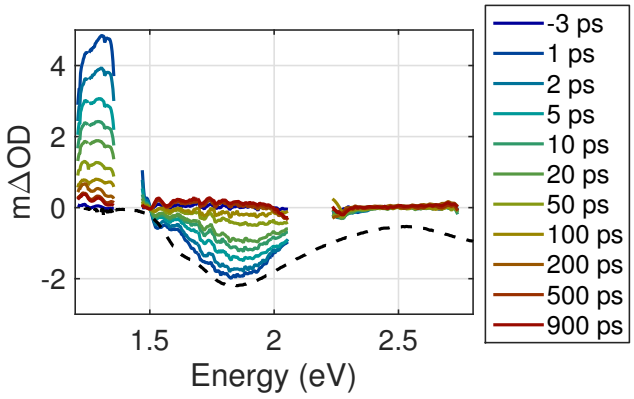

Figure 3.23: Full-frequency pump probe spectra of 100% TBTV upon 2.2 eV photoexcitation.

The transient spectra for the C16-TBTV polymer series excited at 2.2 eV are similar to those obtained upon 3.1 eV photoexcitation. The recovery of the GSH and decay of the ESA are again correlated, suggesting a simple decay pathway. The decay of the ESA feature is also well fitted by a single stretched exponential decay for each of the polymers, as shown in Figure 3.24.

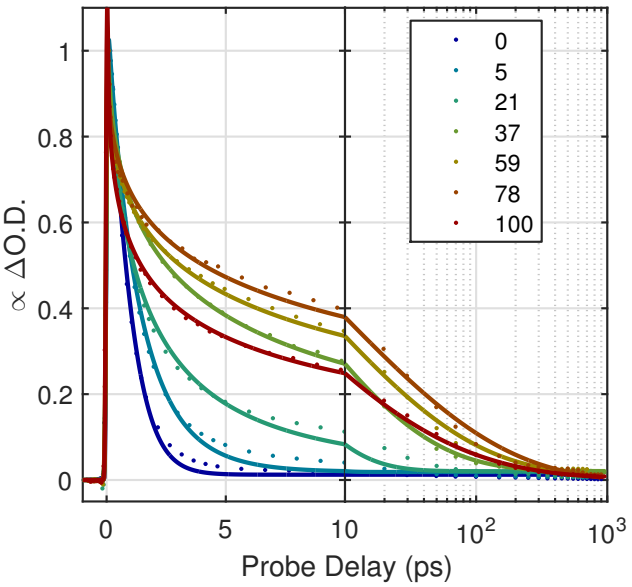

Figure 3.24: The normalized signal amplitude of the ESA feature from each of the C16-TBTV polymer ratios after 560 nm photoexcitation. Note that the x-axis changes from a linear scale to a logarithmic scale at 10 ps.

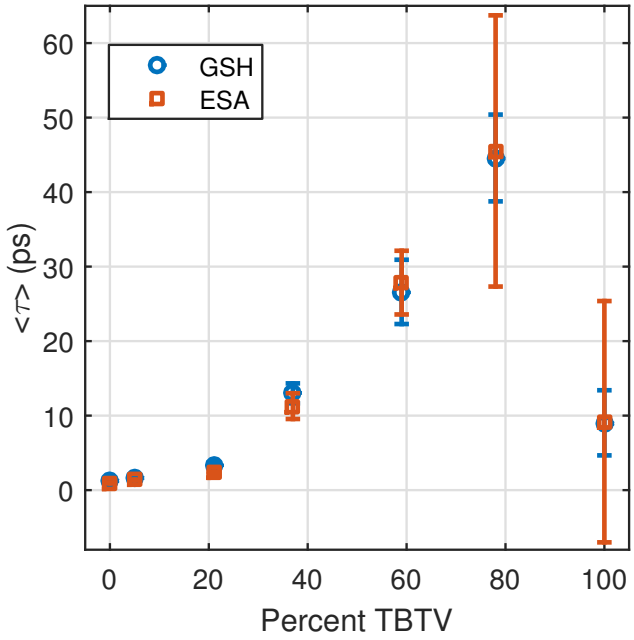

Figure 3.25: A plot of $<\tau>$ vs percent TBTV for the C16-TBTV polymer series upon 560 nm photoexcitation.

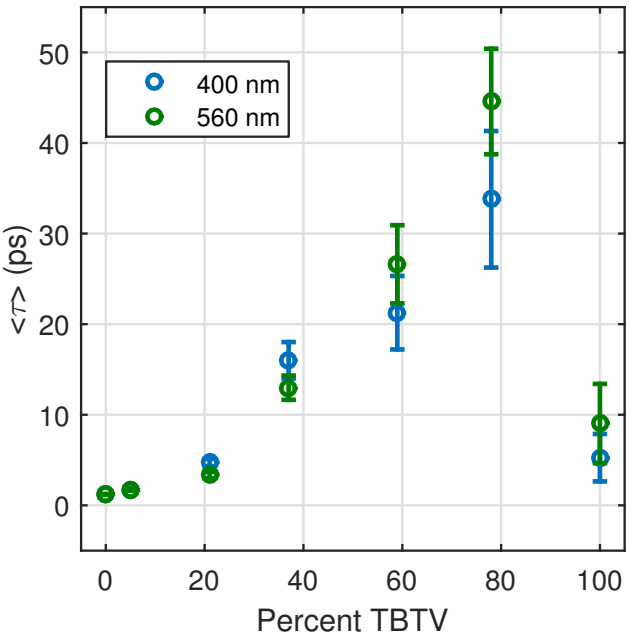

Figure 3.26: A comparison plot of $<\tau>$ vs percent TBTV for the C16-TBTV polymer series upon 400 (blue) and 560 nm (green) photoexcitation.

Figure 3.26 compares the measured value of $<\tau>$ for each polymer ration upon 400 nm and 560 nm photoexcitation. The measured values agree well within the estimated error bounds. If the exciton was localized to a single monomer unit, and the results upon 400 nm excitation only arose because of preferential excitation of longer lived TBTV excitons, then we would potentially expect shorter lifetimes upon 560 nm excitation. Because the lifetimes are comparable within error, these results suggest that the increased lifetime observed is not due to preferential exciton of TBTV chromophores, or at the very least that the initially generated exciton localizes to the same state within our time resolution

regardless of whether or not it is excited by 400 nm or 560 nm photons.

By observing how the transition dipole moment rotates as a function of time, we are provided information with the nature of the exciton relative to the initially generated state. The polarization anisotropy can be calculated as a function of time from the following equation.[119]

$$r(t) = \frac{I_{\parallel}(t) - GI_{\perp}(t)}{I_{\parallel}(t) + 2GI_{\perp}(t)} \tag{3.14}$$

where $I_{\parallel}$ is the intensity of the parallel polarized probe beam, $I_{\perp}$ is the intensity of the perpendicular polarized probe beam, and G is an experimental correction factor which accounts for differences in detector response to the different polarizations of light. In the setup employed in this study, G was experimentally determined to be approximately 1.

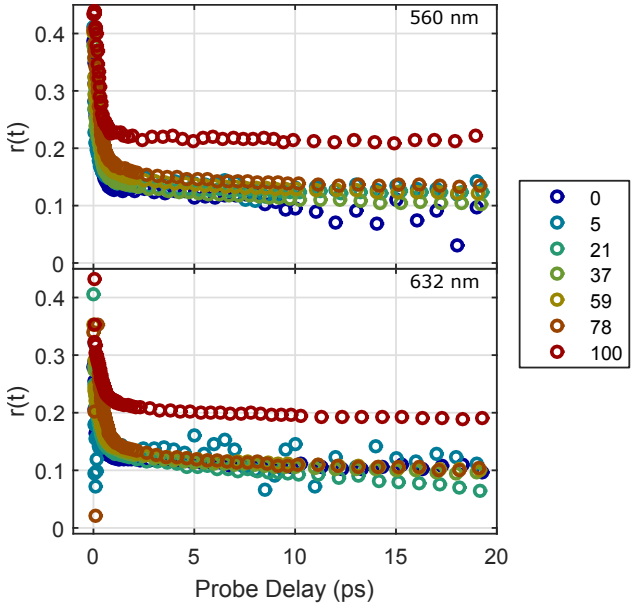

Figure 3.27: Anisotropy r(t) at 560 nm (top) and 632 nm (bottom) for each of the C16-TBTV polymer ratios.

Figure 3.27 shows the ultrafast anisotropy measurements collected for each of the polymers at 560 nm (top) and 632 nm (bottom) probe wavelengths. We are probing the intensity of the light that is not absorbed due to the loss of the ground state population. The anisotropy decays are similar for both probe wavelengths, starting out around the theoretical maximum value of 0.4, then decaying with the same initial time constant (∼300 fs) before leveling off. This rapid decay corresponds to strong electronic coupling, which suggests a Dexter-type energy transfer.[120] For polymers at 78% TBTV and below, r(t) levels out at a value of approximately 0.12; however, the 100% TBTV polymer anisotropy

levels off at a value of 0.21, nearly twice that of the other polymers. These anisotropies correspond to a reorientation of the transition dipole moment by 43° in the polymers with 0-78% TBTV and 34° in neat TBTV.

In poly(3-hexylthiophene) films it was shown that excitons located across multiple polymer chains within 100 fs.[121] The data herein suggest that energy redistribution occurs on sub-picosecond timescales, and that no appreciable change in the absorption dipole occurs over the next 20 ps of the exciton lifetime. It is conceivable that dynamic localization as a result of structural relaxation of excited segments is responsible for this fast decline.[122] These results are also consistent with the conventional view of PTV photoexcitation: direct excitation into a $1B_u$ state followed by rapid internal conversion to the lower energy, dark $2A_g$ state.[103,116] Ikuta et al demonstrated that geometrical relaxation of a free exciton to a self-trapped state occurs within 100 fs in polydiacetylenes.[123]

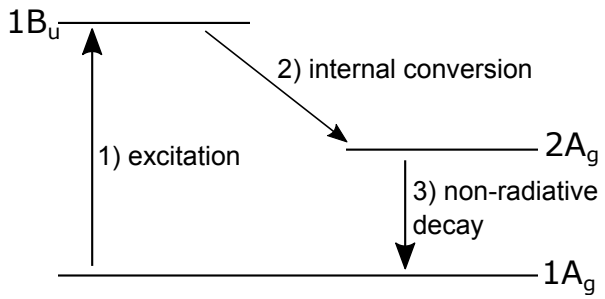

Figure 3.28: Photoexcitation scheme for PTV. Adapted from Musser et al.[103]

The exciton localization size is an important factor worth considering. The greater value r(t) to which the 100% TBTV polymer levels out suggests that the excitons localize into a state more similar to the initial free exciton than each of the other polymers. We note that the 100% TBTV polymer chain also consists of fewer monomer units than the other chains, which could suggest that the exciton size is limited by the polymer chain length. The exciton is limited in its ability to sample new geometries and sites. This also suggests an exciton delocalization size of at least 5 monomer units, which is the average chain length in TBTV. Solution based fluorescence-quenching studies of poly(3-hexylthiophene) with C60-fullerene covalently attached to the ends of the chain found that the exciton generated possessed a 7.0 nm intrachain diffusion length, corresponding to roughly 17 thiophene moieties.[124]

Coupled with the anisotropy results, the change in the excited state lifetime induced by a increasing the relative TBTV composition appears to largely arise from a decrease in the non-radiative decay rate from the excited $2A_g$ state to the $1A_g$ ground state. Increasing the TBTV content in the polymer chains up to 78% TBTV appears to reduce the accessibility of rapid vibrational decay pathways, potentially by increasing the planarity of the polymer and eliminating conjugation breaking defects such as kinks and twists in the polymer backbone. A combination of changing the charge-transfer characteristic by adjusting monomer unit composition and the shorter chain length account for the shorter lifetimes observed in 100% TBTV.

3.3.3 OC16-TBTV

In order to determine the influence of monomer identity on the measured ultrafast dynamics, experiments were also conducted using a series of ether substituted TV monomers (OC16-TV). These monomers should provide extra electron density due to the electron donating ether chain, potentially increasing the relative strength of the donor/acceptor interaction and enhancing the charge-transfer characteristic of the exciton.

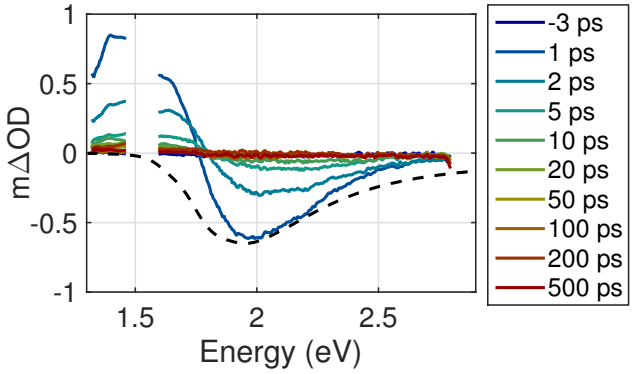

Figure 3.29: Full-frequency pump probe spectra of 0% TBTV upon 3.1 eV photoexcitation.

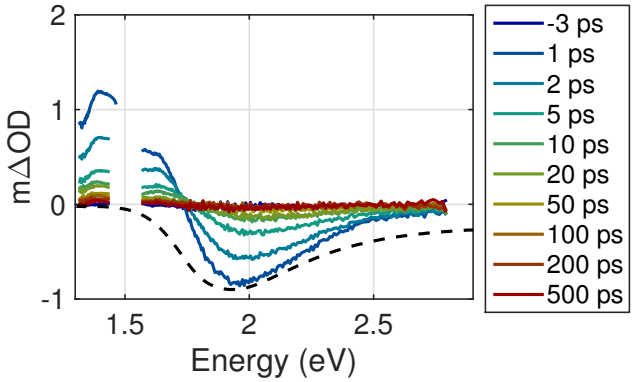

Figure 3.30: Full-frequency pump probe spectra of 22% TBTV upon 3.1 eV photoexcitation.

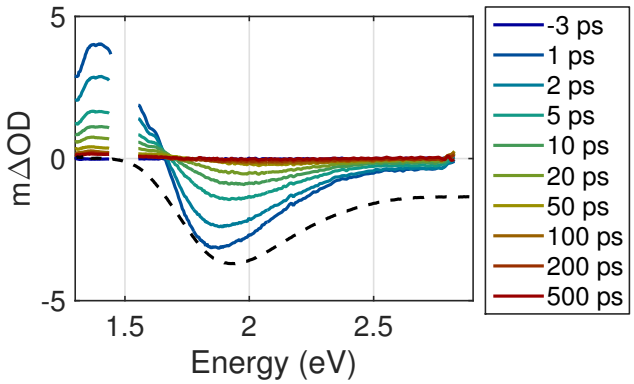

Figure 3.31: Full-frequency pump probe spectra of 45% TBTV upon 3.1 eV photoexcitation.

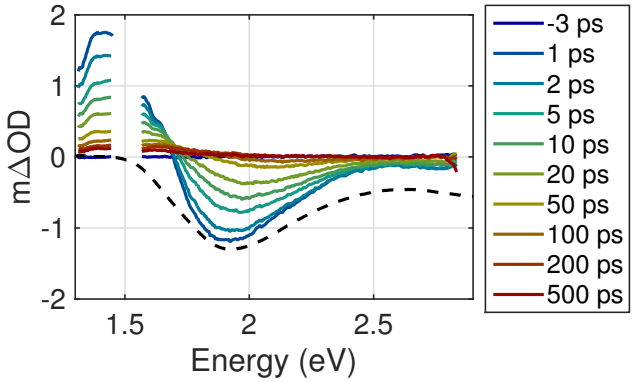

Figure 3.32: Full-frequency pump probe spectra of 77% TBTV upon 3.1 eV photoexcitation.

The transient absorption spectra for 0-77% TBTV of the OC16 series are presented in Figures 3.29-3.32. The transient features are similar to that of the C16-TBTV series: a short lived excited state absorption that decays concurrently with a ground state hole recovery.

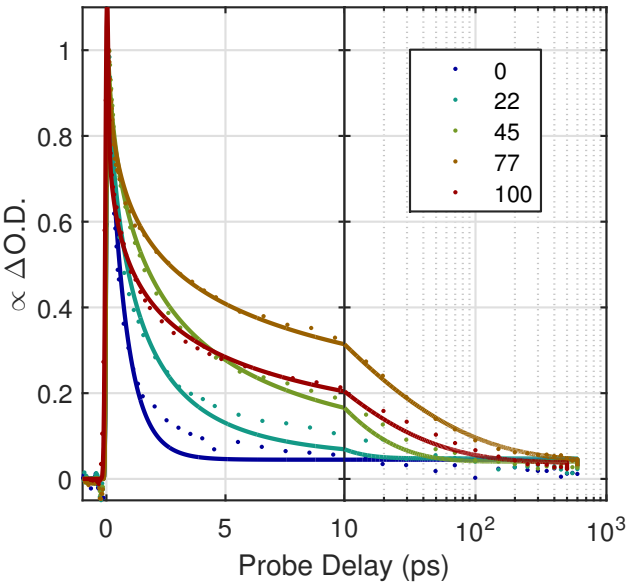

Figure 3.33: The normalized signal amplitude of the ESA feature from each of the OC16-TBTV polymer ratios after 400 nm photoexcitation. Note that the x-axis changes from a linear scale to a logarithmic scale at 10 ps. Stretched exponential fits are shown as solid lines of the same color as the data points.

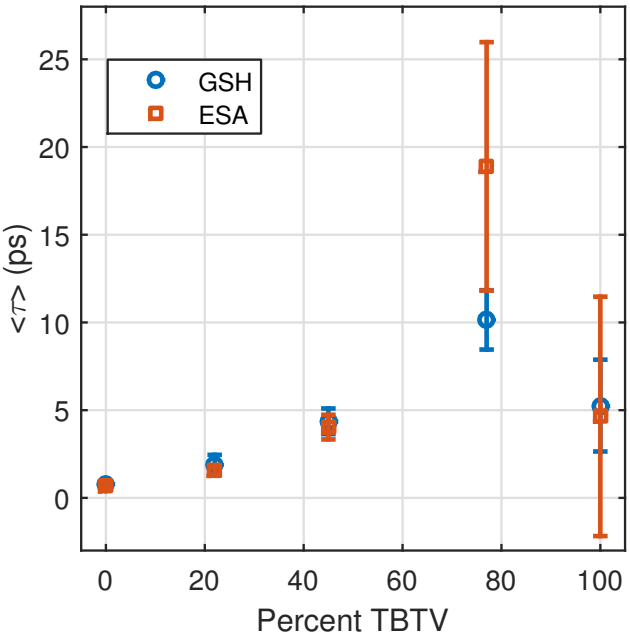

Figure 3.34: A plot of $<\tau>$ vs percent TBTV for the OC16-TBTV polymer series upon 400 nm photoexcitation.

The OC16-TBTV polymer series possess shorter lifetimes than the C16-TBTV series by roughly a factor of two. This shortened lifetime is possibly due to the shorter average polymer chain length for each of the ratios.

In both C16-TBTV and OC16-TBTV polymer series, the excited state lifetime can be increased over that of either homopolymer. Interestingly, the maximum lifetime does not occur at a 1:1 ratio of donor:acceptor, but rather closer to 1:3. These results suggest that further improvements in the efficiencies of polymer based solar cells may yet still be achieved through tuning of monomer unit composition. Moreover, this efficiency gains may

still manifest themselves via ensemble changes in polymer composition, leading to further reduction in effective manufacturing costs.

Singlet fission has been observed in thin films of PTVs. Busby et al. demonstrated that singlet fission with yields of 173% occurring in donor-acceptor polymers in dilute chloroform solution.[125] By using pulsed radiolysis to generate isolated triplet excitons, they were able to assign transient absorption features to triplet states. The rate of singlet fission was found to be affected by polymer chain composition. By adjusting the composition, the charge-transfer character of the initial singlet exciton. They also observed evidence of an internal conversion process ($1B_u$ to the dark $2A_g$) competing with internal conversion on 100 fs timescales. The singlet fission occurs from the 1Bu state, so the competing decay to 2Ag can greatly reduce efficiency. The observed lifetimes are on the order of ps, much shorter than would be expected due to the spin forbidden triplet recombination process. Because excitons generated from singlet fission are confined to the same polymer chain, triplet-triplet annihilation to reform a singlet exciton may lead to shorter effective lifetimes. The shorter 100% TBTV polymer chain length may thus explain the shorter observed lifetimes, as triplet pairs have fewer sites available to sample, annihilation is more probable.

In the a study on singlet fission in PTVs, excitation in excess of the bandgap was required for singlet fission, resulting in longer measured lifetimes (and excess ESA assigned to triplets).[103] Because the transient decay rates are unaffected by excitation frequency, there is not as strong of a case for singlet fission in these polymers. Additionally, analysis of spectral shapes does not reveal any meaningful differences in excited state absorption due

to excess photon energy excitation; however, there are several experimental complications which make such a comparison more difficult. Beam overlap between the pump and probe pulses may have differed for the different pump excitation frequencies, and differences in fluence could also change the transient shapes.

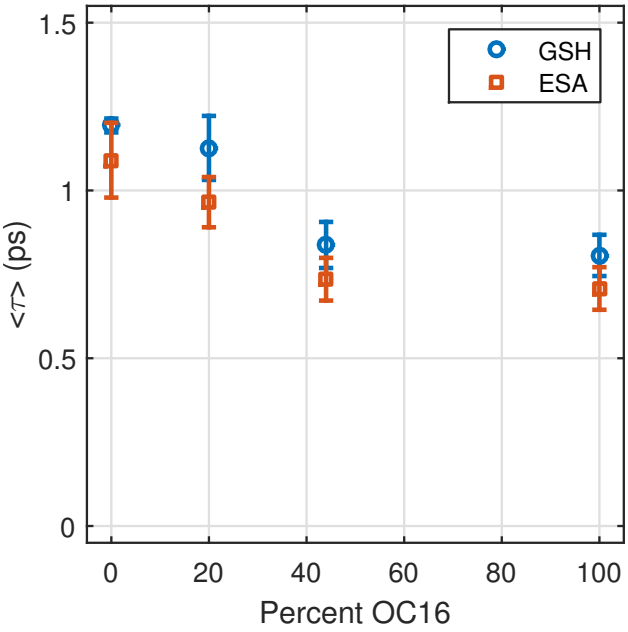

Figure 3.35: A plot of <τ> vs percent TBTV for the C16-OC16 polymer series upon 400 nm photoexcitation.

Polymers consisting of C16-TV and OC16-TV units so no appreciable tunability in exciton lifetime. The increased lifetime in the C16-TBTV and OC16-TBTV polymer series lifetimes is thus likely due to the increased charge-transfer character of the exciton.

Chapter 4

Exciton Annihilation in Subphthalocyanine Thin Films

4.1 Introduction

In recent years, much scientific effort has been exerted in the field of organic optoelectronics, which utilizes an array of organic based materials with custom-tailored properties in such devices as organic light emitting diodes, field effect transistors, and photovoltaics.[20,23] Relating the molecular properties of these materials to parameters regarding device performance has been of great interest to researchers.

Organic photovoltaics have emerged as an alternative to traditional silicon based devices, and possess a number of advantages such as mechanical flexibility, semi-transparency, and in some cases solution processability. In OPVs, a photon incident upon the cell is

absorbed by an organic chromophore, promoting an electron to an excited state and generating a Coulombically bound electron-hole pair known as an exciton. In order to generate a current capable of doing work, the attraction between the electron and whole must be overcome so that free charges may arise. This is typically achieved at an interface between two different organic materials, where the difference in energy levels between the two molecules provides the driving force for exciton dissociation and charge transfer. One of the key factors governing device performance, then, is the process of diffusion of the initially generated exciton to a heterojunction.

Exciton diffusion lengths in singlet materials have often been measured by means of fluorescence quenching experiments. In this method, a thin film of the organic material is prepared with a layer of an exciton quenching material (such as C60 fullerene). Excitons which undergo charge transfer will exhibit quenched fluorescence compared to a neat film. As the thickness of the organic material of interest is increased, excitons are statistically more likely to be generated farther from quencher interface and consequently will not diffuse to that boundary where the fluorescence is quenched before recombination. Careful modeling can then extract one-dimensional diffusion lengths by means of relating the quenched fluorescence to the thickness of the organic layer. While this technique possesses some advantages, it relies on two assumptions: that the material itself possesses measurable and substantial fluorescence, and that the fluorescence quenching occurs at the interface. For dark materials, that is, those that decay via predominantly non-radiative channels, fluorescence quenching is not a feasible means to evaluate diffusion length.

An alternative method to evaluate exciton diffusion processes has been through the use of time-dependent exciton annihilation studies by means of pump-probe spectroscopy.[45,126–128]

When exciton densities are high, typically on the order of 10^{18} cm^{-3} or more, excitons in close proximity may interact in such a way that leads to the recombination of one or both excitons. For example, two singlet excitons may annihilate, resulting in the decay of one exited singlet to the ground electronic state via non-radiative channels

$$S_1 + S_1 \longrightarrow S_0 + S_1 \tag{4.1}$$

The rate of exciton annihilation is dependent on two factors: the separation between excitons and the exciton diffusion rate. More mobile excitons are more likely to sample regions spatially close to one another, and thus exhibit accelerated annihilation compared to less mobile excitons. Various models have been developed to describe this behavior and have been used experimentally with good success.

Previously, Menke et al. reported on the influence of film composition on OPV device performance for vapor-deposited thin films of SubPc and UGH2.[129] The structures of these molecules are shown in Figure 4.1. Menke et al. observed an increase in device efficiency from 3.3% in neat SubPc to 4.4% in a 50% dilution of SubPc in UGH2. This was largely attributed to the dependence of excition diffusion length, L_D, on film composition, which was in part mediated by changing Förster Radii and mean separation between optically active SubPc chromophores. To gain further insight into the nature of this tunability, we

employ pump-probe spectroscopy to characterize the exciton diffusion dynamics of SubPc in UGH2.

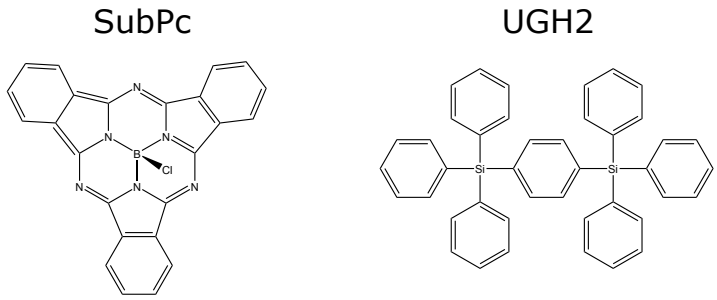

Figure 4.1: Chemical structures of SubPc and UGH2

4.2 Experimental

SubPc was purchased from Sigma-Aldrich and UGH2 was obtained from Lumtec; both were used without further purification. Quartz substrates were first cleaned by sonication in tergitol and acetone, before being boiled in an isopropyl alcohol bath. Thin films of SubPc and SubPc diluted in UGH2 were prepared by vacuum deposition of the materials onto the cleaned substrates. Materials were deposited at pressures below 10^{-6} Torr with a total deposition rate of 0.2 nm s^{-1}. In the mixed films, SubPc and UGH2 were simultaneously deposited by separate sources. Film thicknesses were verified by spectroscopic ellipsometry.

UV/Vis experiments were conducted using a Cary 14 spectrometer. For temperature dependent measurements, the sample was placed in recessed cavity inside an aluminum

block. Two glass windows on either side of the sample permitted light to transmit and sealed the interior cavity. A thermocouple was placed inside the cavity in order to measure the temperature. The aluminum assembly was heated with a heating element at a rate of approximately 0.2 °C min^{-1}. The differential spectra were calculated by subtracting the room temperature spectrum from the spectra collected at higher temperatures. Spectra were also collected as the sample cooled back to room temperature in order to check for hysteresis, which was not observed.

Ultrafast pump probe spectroscopy was performed using a home built Ti-sapphire oscillator, stretcher-compressor, and regenerative amplifier similar in design to one previously described in greater detail.[71] A noncollinear optical parametric amplifier was used to generate the visible pump beam (with photon energy of 2.36 eV (525 nm)). The probe beam was generated by focusing 810 nm light into a 2 mm sapphire, creating a white light continuum. For all experiments reported herein, the pump polarization was set to the magic angle (54.7°) with respect to the probe polarization in order to isolate isotropic dynamics. The pump and probe beams were focused and crossed at the sample with a parabolic mirror. At the intersection of the beams, the pump had a beam waist of approximately 150 μm (full-width half-max) while the probe had a waist of approximately 50 μm (full-width half-max). After transmitting through the sample, the probe beam was first collimated and then focused into a monochromator (Princeton Instruments SP2150, 150 g/mm grating) and then detected using a 256 pixel diode array (Hamamatsu, S3901-256Q Si array with C7884-20 driver). The full-frequency wavelength axis was calibrated using a series

of spectrally well-defined band-pass filters. During full-frequency data collection, samples were placed in a sealed box of nitrogen under pressure greater than the surrounding atmosphere in order to minimize the effects of oxidation on the observed kinetics. Additionally, the substrates were rotated at a rate of approximately 5 Hz to replace the sample volume between laser shots. All transient spectra were collected at room temperature.

4.3 Results and Discussion

4.3.1 UV/Vis Absorption Spectra

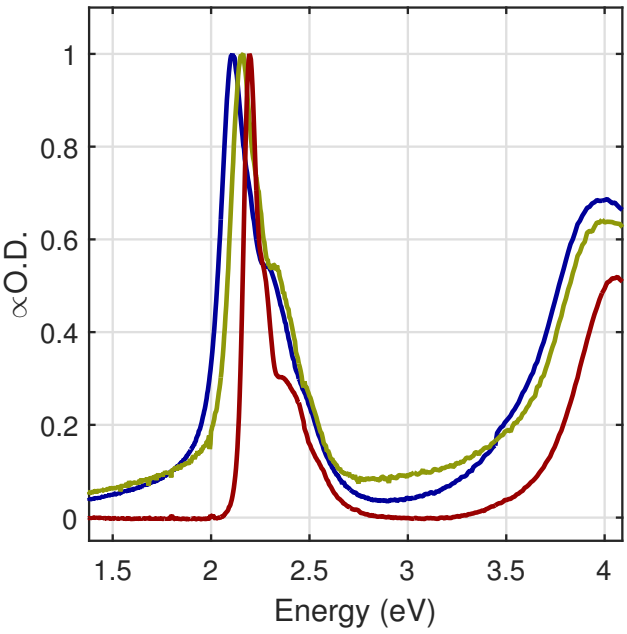

Figure 4.2: UV/Vis spectra of representative SubPc thin film samples (blue, film of 100% SubPc by mass; yellow, film of 27.4% SubPc by mass) normalized to have equal height. The spectrum in dilute chloroform solution (red) is shown for comparison.

The optical absorption spectra for representative SubPc films are depicted in Figure 4.2. All thin films all show the same general features typical of phthalocyanines and other porphyrin-like materials: the Soret band around 4 eV, q-band around 2.15 eV. Structure

in the Q-band is likely due to x. As the SubPc is diluted in the UGH2 matrix, the absorption undergoes a relatively linear hypsochromic shift with respect to SubPc concentration, with the peak shifting approximately 0.1 eV to lower energy from dilute solution to neat film. The shifting of the absorption maximum with respect to solid state dilution is well documented and has been attributed to the increased aggregation observed in neat films. The Q-band broadens as the SubPc concentration is increased, indicative of the relatively amorphous and disordered nature of the thin films.

4.3.2 Transient Absorption Spectroscopy

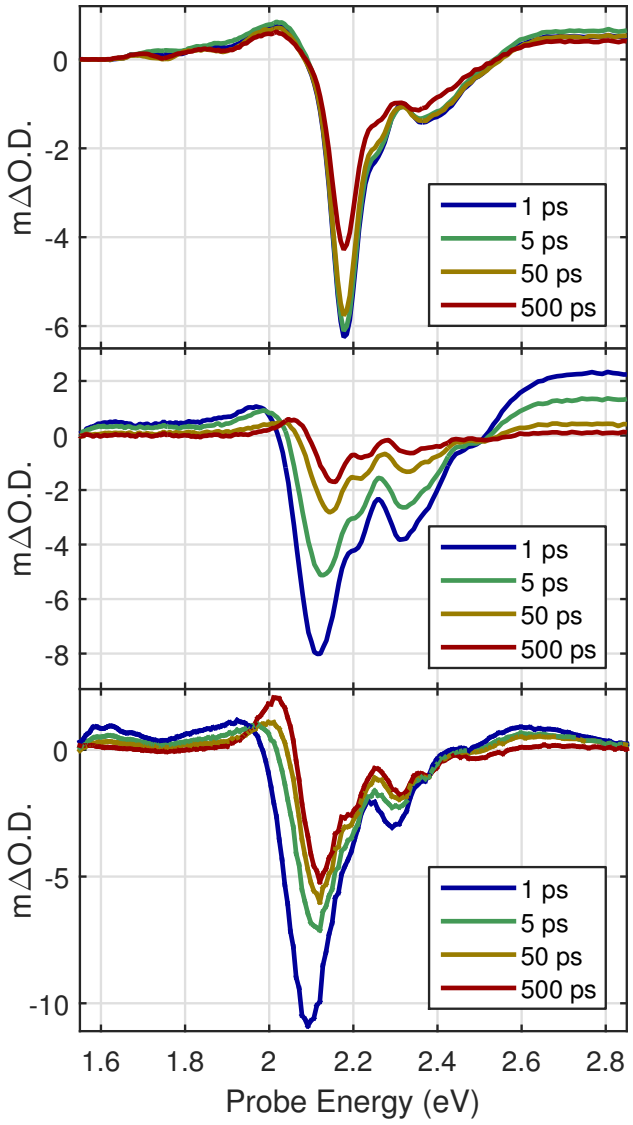

Figure 4.3: Selected full frequency transients for top: 0.5% SubPc; middle: 27.4% SubPc; bottom: 100% SubPc. All samples were excited with 525 nm pump light.

Selected full frequency spectra are shown in Figure 4.3. The spectral shapes are similar for each concentration of SubPc. Each possesses a negative bleach feature due to loss of absorption resulting from depopulation of the ground state. Positive excited state absorption features are prominent in the spectra at probe energies below 2.1 eV and above 2.3 eV. For 0.5% SubPc, very little spectral evolution occurs; the signal decays slowly, and the shape of the spectrum remains relatively constant throughout the exciton lifetime.

The spectra of 27% SubPc initially appear similar to those of the dilute solution, with two excited state absorption on either side of a ground state bleach. There appears to be subtle shifts in the overall shape of the transient spectra, with the low probe energy transient absorption shifting roughly 0.2 eV by 500 ps.

The spectral changes are most dramatic in the 100% SubPc transients. The GSH feature shifts to higher energies, with the trough position increasing by approximately 0.05 eV at 500 ps. Additionally, the ESA above 2.4 eV and below 1.9 eV decays nearly completely, while another narrow absorptive feature grows in at approximately 2.05 eV.

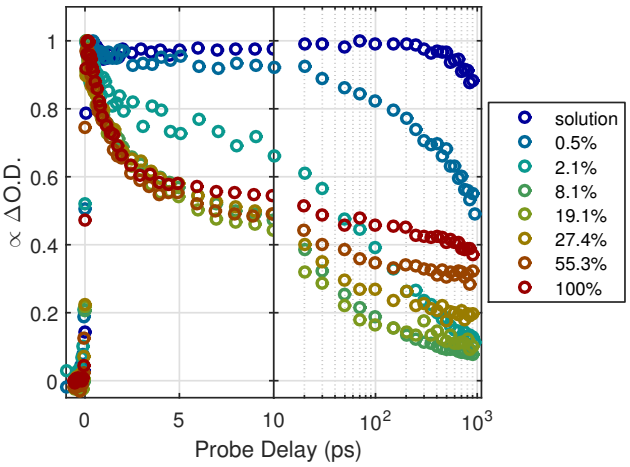

Figure 4.4: Decays of the transient absorption signal for different concentrations of SubPc in UGH2. The slices were taken from within the GSH (around 2.15 eV).

Figure 4.4 depicts the normalized intensity from within the GSH for each concentration of SubPc in UGH2. Ratios above ∼8% SubPc exhibit a similar fast reduction in signal amplitude prior to 10 ps, after which the signal decay rate begins to diverge, with slower rates at higher concentrations of SubPc. Only the dynamics of the dilute solution of SubPc are well characterized by a single exponential fit, with the mixed and neat films requiring three or four exponential terms at a minimum in order to adequately capture dynamics at all times. The complicated decay dynamics coupled with shifting spectral features suggest a complex electronic landscape for the exciton.

Previously, such shifts in spectral features have been attributed to a number of physical phenomenon, such as oxidized sates or trapping of excitons on aggregate domains. In one

recent paper, triplet fusion and charge transfer to a metal centered ^{3}(d,d) state was given as the explanation for similar shifts in full-frequency spectra in a Platinum Octa-ethyl Porphyrin thin film.[130] We will endeavor to demonstrate in the proceeding sections that the origin of this shifting feature observed in the SubPc films is not purely electronic in nature, but instead results from a changing vibrational environment experienced by the chromophores in the thin film. This changing vibrational environment is the direct result of energy released through non-radiative decay channels, predominantly internal conversion and exciton-exciton annihilation.

4.3.3 Temperature Dependent UV/Vis

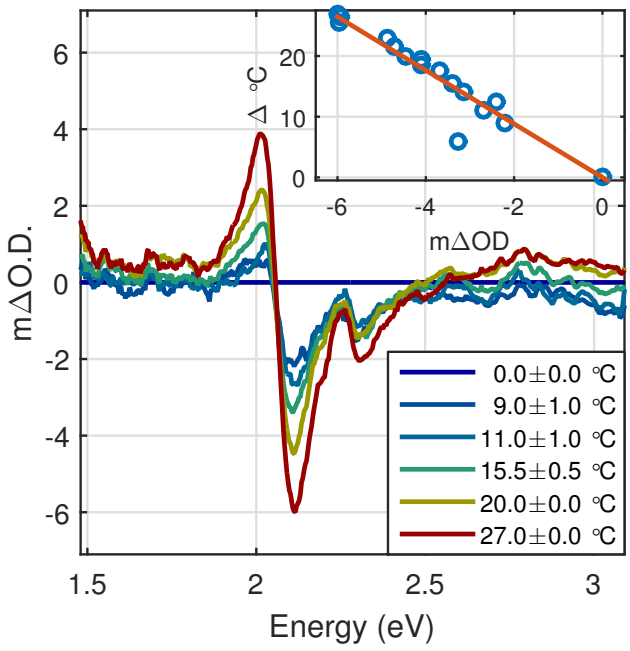

Figure 4.5: Temperature dependent UV/Vis spectra of neat SubPc. Inset: the amplitude of the negative feature vs change in temperature.

Temperature-dependent UV/Vis absorption measurements were made on a neat film of SubPc. A differential spectrum was calculated by subtracting the spectrum obtained at room temperature from that of the elevated temperature. Selected difference spectra are plotted in Figure 4.5. As the film is heated, differential features mimicking those observed in transient absorption experiments are observed. Additionally, the magnitude of these differential features are on the order of 1 to 4 mΔO.D., again comparable to the magnitude of our pump probe experiments. The amplitude of the negative feature centered at

approximately 2.1 eV increases linearly with temperature (shown in the inset of Figure 4.5).

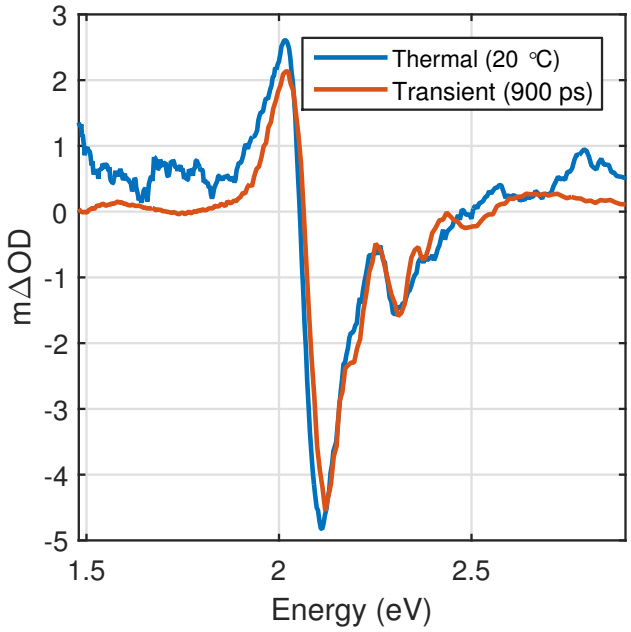

Figure 4.6: A comparison of the temperature dependent UV/Vis differential spectrum collected at 20 °C and the transient absorption spectra (900 ps probe delay) of neat SubPc.

Figure 4.6 compares the thermal differential spectrum taken at $\Delta T = 20°C$ with the transient absorption spectra collected at a probe delay of 900 ps. Both spectra are plotted in real, measured units without relative scaling. There is significant agreement between the two spectra, both in the positioning of the peaks and troughs as well as the signal amplitude. As the excitons annihilate and decay via non-radiative pathways, the heat is deposited into the surrounding SubPc chromophores. SubPc chromophores are promoted

to vibrationally exicted states within the ground electronic state. Because the distribution of molecules among vibrational states has been altered, the bulk electronic absorption undergoes a shift as well. It should also be noted that the thermal contribution is non-zero throughout most of the range of observed probe energies, making it difficult to select any particular spot from the transient absorption experiments that could be expected to be free of the thermal influence.

To evaluate whether or not the apparent temperature increases are reasonable, an upper bound of the temperature rise in the sample given a specific experimental condition can be estimated by assuming that all of the energy in the pump pulse is converted to heat. This is a reasonable assumption in SubPc thin films, as even in the low exciton density limit the majority of SubPc excitons decay via non-radiative decay channels (neat films of SubPc possess a photoluminescence quantum yield of only 0.01). Previously determined exciton diffusion rates for SubPc would suggest that up to 98% of excitons would decay via annihilation under the experimental conditions employed in this study, further supporting this hypothesis. An upper bound for the maximum temperature fluctuation that would be expected can be calculated by the following equation

$$\Delta T = \frac{F\alpha}{lc\rho} \tag{4.2}$$

where F is the laser fluence ($3.8\times\ 10^{-4}$ J m^{-2}), α is the fraction of the incident power absorbed by the sample (0.206), l is the film thickness (36.21 nm), c is the specific heat

capacity of SubPc, and ρ is the molecular density (1.624 g cm^{-3}). While the exact heat capacity of SubPc is not known, similar organic molecules have specific heats on the order of 500 J mol^{-1} K^{-1}. Using Equation 4.2 and the values indcated above, we obtain an approximate estimate of 23 °C for the temperature increase in the neat SubPc film.

4.3.4 Annihilation Modeling

Spectral Deconvolution

The presence of the thermally induced change in ground state absorption complicates interpretation of the full frequency spectra. In order to accurately model exciton population dynamics, the two components, excitonic and thermal, must be separated. We assume that for an given delay time t the transient signal S is a linear combination of the excitonic and thermal components, i.e.

$$S(t, \lambda) = \epsilon_e(\lambda)C_e(t) + \epsilon_t(\lambda)C_t(t) \tag{4.3}$$

where ϵ_e and ϵ_t represent the frequency dependent portion of the excitonic and thermal components, respectively, and C_e and C_t represent the time dependent portion of the same. To model the data, we first need to identify ϵ_e and ϵ_t.

For the excitonic component, ϵ_e can be estimated by using one of the transient spectra at early delay times (200 fs), before any appreciable exciton decay has occurred. The thermal component is estimated by using a late transient spectra (900 ps), where it is

assumed that annihilation has resulted in the loss of all or nearly all exciton population, and the excitonic contributions to the transient signal are negligible. C_e and C_t are then optimized via an iterative least squares process to minimize the residual between the fit and the raw data.

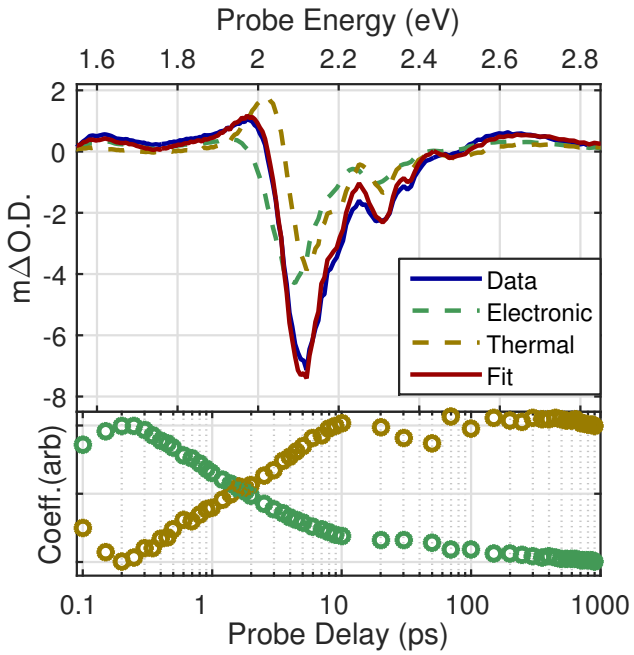

Figure 4.7: Deconvolution of the thermal and excitonic signals in neat SubPc full frequency spectra. Blue: transient collected at 5 ps. Green: Excitonic component. Yellow: Thermal Component. Red: Optimized fit of the data. Below: The coefficients (arbitrary scaling) for each portion of the spectrum as a function of probe delay time.

The result of this optimization is shown for the transient spectra of neat SubPc at a probe delay of 5 ps is shown in Figure 4.7. By optimizing the coefficients C for each probe

delay, we can obtain a measure that is proportional to the exciton population, and free of any interference from the changes in ground state absorption due to heating of the film. Isolating the excitonic signal allows us to accurately capture the exciton dynamics using an exciton annihilation model.

The resulting coefficients for given probe delay times are depicted in Figure 4.7. Initially, the full frequency spectra consist almost entirely of the excitonic spectrum. The growth of the thermal contribution is correlated with the decay of the excitonic contribution, which further corroborates the hypothesis that the signal at long delay times is a result of the deposition of thermal energy in the film. After about 10 ps, there is relatively little change in the amplitude of C_t, while C_e continues to trend towards zero.

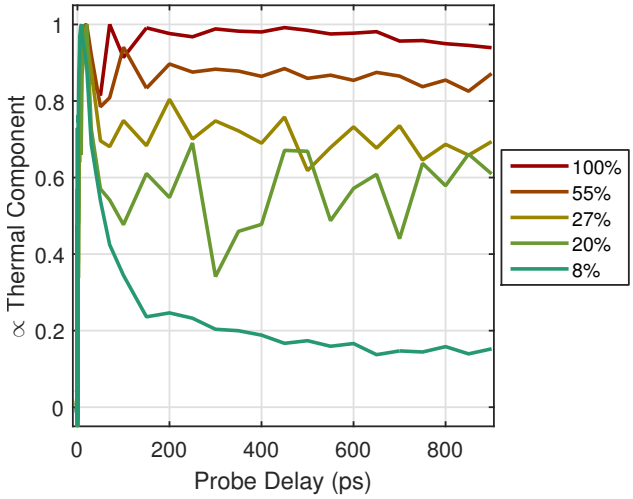

Figure 4.8: The normalized amplitude of the thermal coefficient as a function of probe delay time for each of the SubPc:UGH2 films.

The decomposition fitting was performed in mixed SubPc/UGH2 films as well. The normalized amplitude of the thermal coefficient at each delay time is plotted in Figure 4.8. In each of these samples, a rise in the magnitude of the thermal coefficient is observed on a timescale less than 100 ps, similar to that of the electronic decay. This suggests the decay of the excitonic component is correlated with that of the thermal component, as would be expected due to the majority of the heat deposition resulting from exciton annihilation. In the neat SubPc film, the coefficient levels out near one, with only minimal decay over the course of the first 900 ps. However, as the concentration of SubPc is diluted we observe an initial rapid rise followed by a subsequent decay of the thermal coefficient, which then levels out after roughly 150 ps. This is again consistent with our hypothesis of the thermal influence on the ultrafast spectra. After annihilation, large amounts of vibrational energy are initially localized on SubPc molecules. However, the excess vibrational energy is quickly dissipated among neighboring molecules. As the SubPc concentration is diluted, the chromophore neighbors are increasingly likely to be UGH2. The shifts in the UGH2 spectra due to increased vibrational energy do not occur in the visible region of the spectrum, and do not manifest themselves in our detected range. Overall, the magnitude of the thermal coefficient remains relatively constant after 200 ps due to the much slower diffusion of heat. Over the nanosecond timescale of the experiment, only a minimal amount of vibrational energy is dissipated out of the probe beam spot.

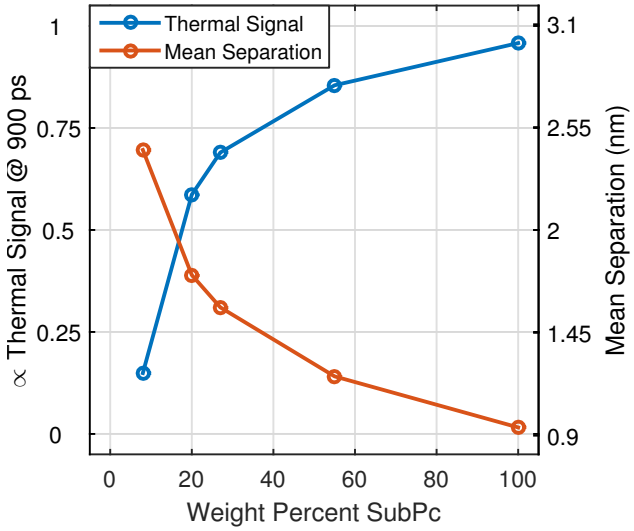

Figure 4.9: Blue, left axis: The contribution of the thermal spectra as a fraction of its maximum contribution plotted as a function of film composition. Orange, right axis: The mean separation (nm) between SubPc molecules in the film plotted as a function of film composition.

Figure 4.9 shows the thermal signal remaining as a fraction of the maximum amplitude of the thermal coefficient determined during the deconvolution (blue) and the mean molecular separation between SubPc molecules (orange). The thermal signal remaining trends in the opposite direction as mean separation, indicating that as the spacing between SubPc molecules increases, a greater percentage of the thermal energy is deposited on neighboring UGH2 instead.

Exciton Annihilation Modeling

Exciton annihilation is usually considered as analogous to that of a bimolecular rate equation and is solved as such.

$$\frac{dn(t)}{dt} = -kn - f\gamma(t)n(t)^2 \tag{4.4}$$

Here $n(t)$ is the exciton density as a function of time, k is the intrinsic decay rate of the exciton (that is, the unimolecular decay rate which is governed primarily by non-radiative and radiative decay processes), $\gamma(t)$ is the rate coefficient of the annihilation process. The factor f depends on the survival of excitons after the annihilation event. In the circumstance where both excitons are annihilated, for example, if the event results in an ionization, f equals 1. If only one exciton remains, then f is equal to 1/2. In this chapter we assume that only one exciton is lost during a single annihilation event (therefore f is equal to 1/2).

Exciton annihilation can be described as a diffusion-limited process. To determine the appropriate physical model, the data was fitted to both a one-dimensional and three-dimensional diffusion model. When fitted with the one-dimensional model, highly unphysical diffusion parameters were determined. In contrast, a three-dimensional diffusion model provided feasible diffusion parameters.

The functional form of $\gamma(t)$ for isotropic three-dimensional diffusion is

$$\gamma(t) = 8\pi D R_c \left(1 + \frac{R_c}{(\pi(2Dt)^{1/2}}\right) \tag{4.5}$$

By evaluating Equation 4.4 with $\gamma(t)$ as defined by Equation 4.5, a time-dependent functional form for the exciton population can be determined.

$$n(t) = \frac{n(0)e^{-kt}}{1 + \frac{4\pi D R_c n(0)(1-e^{-kt})}{k} + 2\pi\sqrt{\frac{2D}{k}} R_c^2 n(0) erf(\sqrt{kt})} \tag{4.6}$$

In practice, many of the variables in Equation 4.5 can be determined independently, and are not set as fitting parameters. $n(0)$ can be determined from the laser fluence and absorption of light by the sample. k can be independently measured by time correlated single photon counting techniques. While not precisely known, the annihilation radius can be reasonably assumed to be on the order of the lattice spacing. Thus, D is the major parameter optimized during the fitting routine.

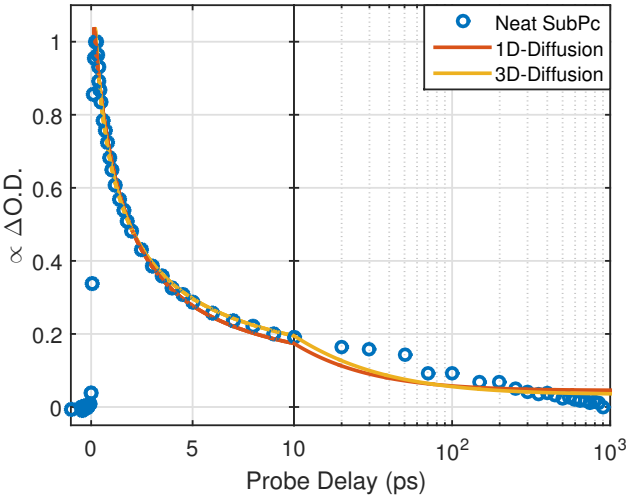

Figure 4.10: Comparison of 1D and 3D annihilation models for neat SubPc.

Figure 4.10 shows the fitting of the electronic coefficient in neat SubPc films using Equation 4.6. The 3D-Diffusion coefficient is determined to be 2.6×10^{-3} cm^2 s^{-1}. Using the low exciton density lifetime obtained from time correlated single photon counting, the average diffusion length L_D can be obtained from the following equation

$$L_D = \sqrt{6D\tau} \tag{4.7}$$

Using Equation 4.7, we obtain a diffusion length of 11.3 nm in the neat film of SubPc. This length is consistent with those measured using photoluminescence quenching to determine exciton diffusion lengths in neat films of SubPc.

4.3.5 Implications for the neglect of the thermal component

In order to evaluate the importance of accounting for the ultrafast growth of the thermally induced transient signal, the 3D annihilation model was also used to fit raw, unadjusted transient data. The amplitude of the full frequency component as a function of probe delay time at various probe energies was fit to this model. The diffusion length was then calculated from the resulting fit parameters, and is plotted in Figure 4.11.

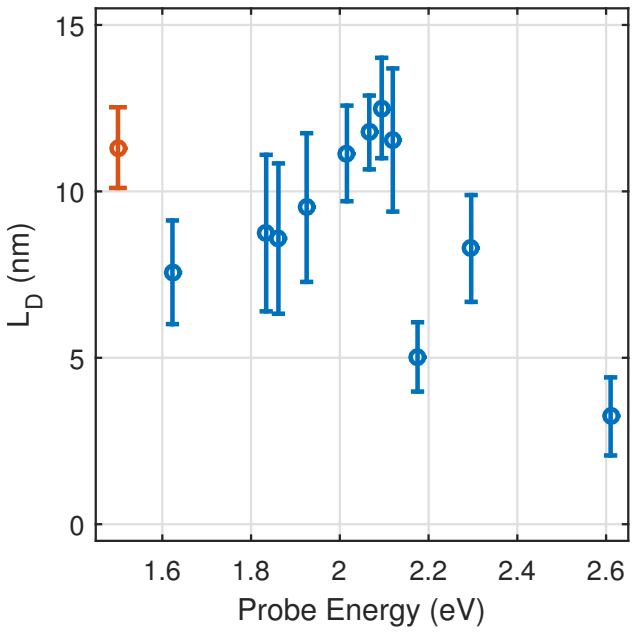

Figure 4.11: L_D obtained from fitting slices of the transient absorption at the indicated probe energy to a 3D-Diffusion model. The L_D obtained from the spectral deconvolution analysis is plotted in red for comparison.

The calculated diffusion length exhibits significant dependence on the probe wavelength

in uncorrected data, ranging from a low of 3.2 nm when probed within the ESA to a high of 12.5 nm probing within the GSH. The relative growth and decay of the thermal and electronic signals, respectively, at each wavelength therefore plays considerable influence in the dynamics observed at any given color. A diffusion length of 11.3 nm is determined from fitting the coefficients of the electronic component after spectral deconvolution, in relatively good agreement with previous measurements for the diffusion length in neat films of SubPc (10.7 nm). It should be noted that there is a narrow range of probe energies (ca. 2.05-2.15 eV) where the measured diffusion lengths correlate well with those obtained from alternative measurements. Unsurprisingly, this corresponds to a region of the spectrum where the thermal contribution happens to intersect zero. It is thus possible that judicious choice of a probe wavelength might be useful in isolating desired electronic signals from thermal contributions.

4.3.6 Excitation Density Dependence

One method towards investigating exciton annihilation involves changing the initially excited population $n(t)$ by reducing pump fluence. Reducing the excitation density will decrease the rate of exciton annihilation, and thus a slowed decay is expected as fluence is decreased. At low enough excitation densities, the transient decay can modeled as a first-order process. Often, attempts are made to escape the exciton annihilation regime by probing single-color transient signals using lock-in detection or balanced photodetection.

This allows for many orders of magnitude smaller to be detected, thus permitting a lowering of pump fluence. By lowering pump fluence, lower initial exciton densities can be achieved using these methods than full frequency detection using a CCD array. However, this comes at the cost of losing any means to effectively separate thermal contributions to transient signal from excitonic sources.

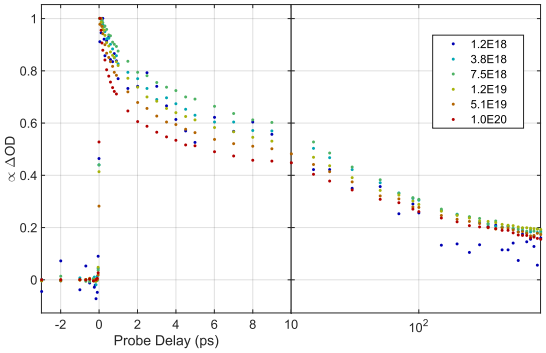

Figure 4.12: Decay of transient signal measured at 560 nm for neat film of SubPc as a function of initial exciton density.

Figure 4.12 shows the excitation density dependence of the transient decay measured at 560 nm for a neat film of SubPc. As expected, the lowering of pump fluence results in a slowing of the initial decay from the excited state. However, at long times the decays at all excitation densities converge to the same value. This suggests that the thermal contribution is still manifesting itself in the transient signals, even at excitation densities less than 0.2% of the molecular density.

4.3.7 Influence of film composition on measured diffusion lengths

The methodology described for deconvoluting the thermal and electronic signals in the transient absorption spectra of neat SubPc can be employed in the dilute films as well. Here, however, there are two considerations to make. In diluting the films, the average number of nearest-neighbor SubPc molecules decreases. Molecules of UGH2 become potential acceptors for the vibrational energy released during exciton annihilation. Thus, we expect to see decreasing contributions of the thermal component as the proportion of SubPc in the film decreases, with more of the excess vibrational energy deposited into UGH2. This will increase the inherent uncertainty for the analyses, as the thermal contribution becomes less distinguishable from the electronic. Second, we must also consider the validity of the exciton diffusion model at low weight percent SubPc films. At larger separations between SubPc molecules, efficient energy transfer is hindered. Thus, sufficiently dilute samples may show little to no decay in the transient absorption spectra as excitons become trapped on isolated SubPc sites. Annihilation may then only occur via static methods, as opposed to the diffusive model employed within this chapter.

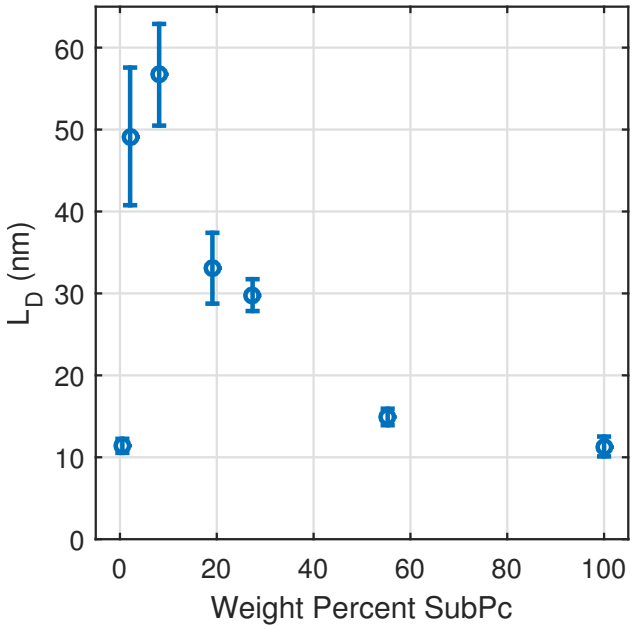

Figure 4.13: Diffusion Length obtained from annihilation models versus weight percent SubPc.

The calculated diffusion lengths are presented as a function of SubPc film composition in Figure 4.13. The relative trends in this plot are comparable to those previously determined by Menke et al.[129] The measured diffusion lengths are fairly reasonable and are within a factor of two from previous measurements, with the exception of the 2% and 8% film compositions. It is possible that the exciton annihilation model is no longer valid at these low chromophore concentrations, with exciton diffusion hindered due to the physical separation between donor and acceptor. The inadequacy of this model may result in the ca. 50 nm diffusion length measurements.

There are clear, measurable trends in the measured diffusion length as a function of film composition. As the concentration of SubPc in the film is diluted from 100% to 20%, the diffusion length triples, increasing from approximately 11 nm in the neat film to 33 nm in the 27% film.

4.4 Conclusions and Implications for Ultrafast Measurements

Consideration of the effects of thermal contributions to ultrafast spectra is not a novel concept. Friend et al have reported at length the influence of these signatures in thin films of pentacene.[131] However, these effects are typically assumed to be negligible on sub-nanosecond timescales due to the much longer timescales associated with heat diffusion. We demonstrate above that the thermal contributions to transient absorption spectra are indeed non-negligible on these timescales, and failure to account for them may result in serious misinterpretation of the ultrafast phenomena occurring.

While the influence of thermal contributions to transient spectra has been discussed here primarily in the context of high exciton densities, and in particular the role of exciton annihilation, the analysis remains valid for any transient pump probe experiments of solid state materials where non-radiative decay processes are an important part of exciton decay. Vibrationally excited chromophores in thin films can give rise to transient signals similar to that of electronically excited chromophores. The overlap between these signals can complicate interpretation of pump-probe transients and population dynamics, in particular

within high exciton density regimes.

After extracting the thermal contributions, the exciton diffusion length could be extracted as a result of fitting a three-dimensional diffusion-limited annihilation model to the transient decay signal for each of the film compositions. The trends in diffusion length match those determined using photoluminescence quenching experiments, which further establishes the validity of these methods.

Chapter 5

Energy Transfer in Subphthalocyanine/Subnaphthalocyanine Films

5.1 Introduction

Advances in OPV performance have often come at the result of modifying the device architecture.[132–134] One such approach consists of using multiple absorbing layers of different chromophores to generate a cascade architecture.[135,136] Depending on the energy levels of the materials used, a cascade photovoltaic can employ either a charge cascade or energy-relay cascade architecture. A charge cascade architecture, shown in Figure 5.1,

employs three or more active layers, each with progressively offset band-gaps, in order to create multiple heterojunctions within a single device.[137–139] The absorption of the materials is selected such that the donor layer and interlayer combined achieve high spectral coverage.[134] The interlayer simultaneously serves as both a donor and acceptor material. In an energy-relay cascade structure (Figure 5.1), the energy levels between the two donors are not sufficiently mismatched to create a heterojunction, and excitons from the donor with a larger bandgap may be transferred to a donor with a smaller bandgap, which can then subsequently be dissociated at the donor-acceptor interface.[140,141] This advantageous architecture requires only a single exciton dissociating layer, which can result in improved efficiencies.[142] In a cascade architecture, excitons cannot be transferred from the lower bandgap donor material to the higher bandgap donor material unless thermally activated, which serves to help direct exciton migration towards the donor/acceptor interface and prevent diffusion to the anode.[143] While an energy-cascade structure can be employed in a planar multilayer architecture, the two absorbing donor layers may also be blended together in a host-guest structure.[144]

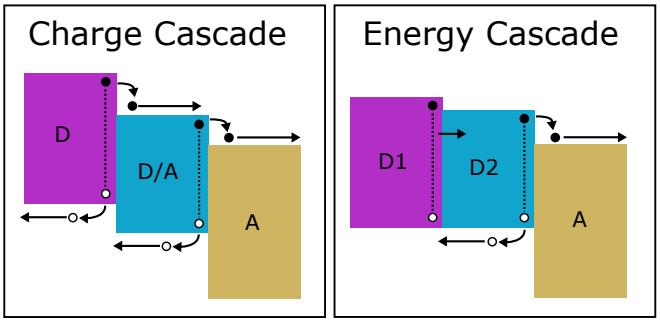

Figure 5.1: A diagram depicting two types of Cascade PV structures: charge cascade (left) and energy cascade (right.) Black circles represent electrons, while white circles represent holes. A dashed black line connecting an electron and hole indicates an exciton. Arrows depict pathways for excitons and free charges.

Chloroboron (III) subnaphthalocyanine (SubNc) is an analogue of SubPc, possessing an additional benzene ring structure, and prominent absorption of photons above 700 nm(<1.77 eV) in the near-IR range.[145,146] SubNc is known for possessing a robust thermal stability, and a number of devices have been constructed using SubNc as the donor layer, in cases demonstrating conversion efficiencies of 4% and higher.[147,148] The complementary absorption of SubNc and SubPc make them promising candidates for energy-cascade photovoltaic devices. Indeed, the two have been used conjointly to create a device achieving 8.4% power-conversion efficiency, without the use of the ubiquitous fullerene acceptor material.[140]

Menke et al. sought to create an efficient energy-cascade device containing a mixed

SubPc-SubNc host-guest layer. Dilution of SubPc and SubNc in the wide bandgap UGH2 improved device efficiency by optimizing exciton diffusion lengths.[129,144] In theory, creating a single blended layer of both donors would allow the device to take advantage of the broad combined spectral absorption of the two molecules, employing both the cascade energy transfer and enhancement of diffusion length by optimizing dilution of the host-guest system. However, it was determined that exciton diffusion in the SubPc-SubNc host-guest systems was suppressed compared to diffusion when the chromophores were diluted in UGH2, and that the enhancements observed in overall device efficiency came due to improvements in the charge collection efficiency.[144]

This study will make use of pump-probe spectroscopy and other optical characterization techniques in order to provide insight as to the mechanism for the suppressed diffusion lengths in these mixed-film systems.

5.2 Experimental

5.2.1 Sample Preparation

SubPc and SubNc were purchased from Luminescence Technology Corporation and used as received without further purification. The structures of SubPc and SubNc are shown in Figure 5.2.

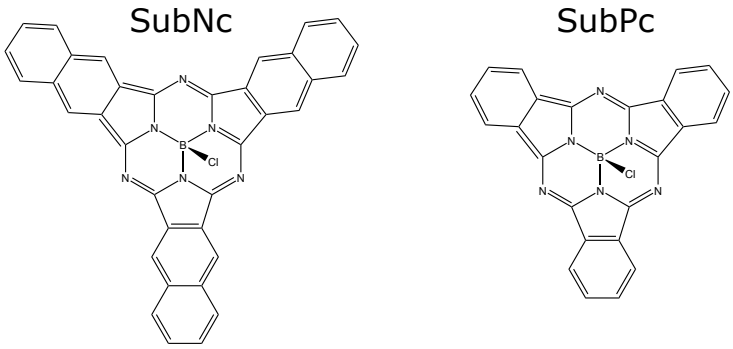

Figure 5.2: Chemical structures of SubPc and SubNc.

Mixed films were vapor deposited onto 1.5 inch diameter quartz disks by thermal deposition under high vacuum (10^{-7} Torr) at a nominal rate of 0.2 nm/s. Film thickness l for each of the ratios was determined by ellipsometry and are presented in Table 5.2.1. The ratios are given as approximate weight percent SubPc in the film mixture.

Percent SubPc	0%	25%	50%	75%	90%	100%
l (nm)	22.0	20.8	20.2	35.2	44.2	25.3

Table 5.1: Film thicknesses corresponding to each of the SubPc/SubNc mixed films employed in this study.

5.2.2 Steady-State Spectroscopy

Absorption measurements were made using an Olis Cary 14 spectrometer as described in Chapter refinstrumentation. The bare quartz substrate was used for baseline subtraction measurements.

Photoluminescence measurements were conducted using a SPEX Fluorolog 1680. All measurements were collected on the same day and with the same detection geometry and incident light fluence. Samples were excited with 2.48 eV (500 nm) light. Photoluminescence was detected in a front-face geometry.

5.2.3 Pump-Probe Spectroscopy

Pump-probe experiments were conducted using the home-built Ti:Sapphire laser system described in Chapter refinstrumentation, which produced 80 fs 810 nm pulses as measured by auto-correlation. The pump pulses were generated using the NOPA also described in Chapter refinstrumentation. Two different excitation frequencies were chosen, 1.98 eV (625 nm), and 2.36 eV (525 nm), both possessing pulse widths of 75 fs as measured by cross-correlation with the 820 nm fundamental. The pump was chopped at a rate of 500 Hz, half that of the probe repetition rate. The probe beam was generated by focusing 820 nm light into a 2 mm sapphire, creating a white light continuum. Pump polarization was set to the magic angle (54.7°) relative to the probe polarization in order to isolate isotropic exciton dynamics. Pump powers were typically set to 20-30 μW prior to incidence upon

the sample.

Thin film samples were placed at the beam focus, where the pump had a beam waist of approximately 150 μm and the probe had a waist of approximately 50 μm. Films were rotated at a rate of approximately 5 Hz to replace sample volume between laser shots. The samples were placed in a box purged under positive pressure of nitrogen to prevent oxidation of the sample. No evidence of laser-illumination induced degradation was observed as determined by steady-state absorption measurements conducted before and after the pump-probe experiments.

5.3 Results and Discussion

5.3.1 Steady State

The absorption spectra of the SubPc/SubNc mixed films are plotted in Figure 5.3. The spectra have been scaled such that the OD is divided by the total film thickness as presented in Table 5.2.1.

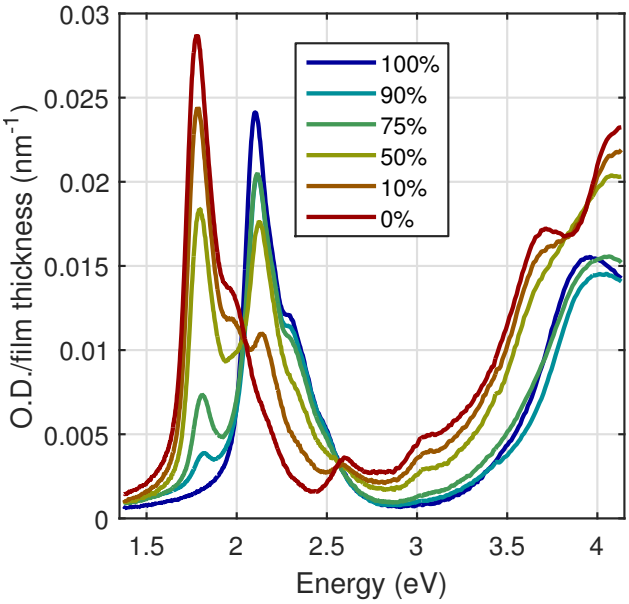

Figure 5.3: Absorption spectra of the SubPc/SubNc mixed films, with OD scaled by film thickness plotted versus photon energy. Each color plot represents the absorption for the mixed film with the weight percent of SubPc given by the figure legend.

The absorption of SubPc, SubNc, and other porphyrin-like materials have been well studied. Both SubPc and SubNc possess an intense band in the UV region, around 4 eV, corresponding to $S_0 \rightarrow S_2$ absorption. This feature is referred to as the Soret band or often the B band.[149–151] The Q-band is the lower energy band, peaking at 1.8 eV in SubNc and 2.1 eV in SubPc, and corresponds to the $S_0 \rightarrow S_1$ absorption. The mixed films exhibit a broad absorption, efficiently capturing photons over a broader range of the visible and near-IR portion of the electromagnetic spectrum than either molecules alone. Upon

mixing, the film absorption undergoes a hypsochromic shift, with the SubPc Q-band peak moving approximately 0.04 eV. This shift arises from a well-known solid-state solvation effect.[152–154]

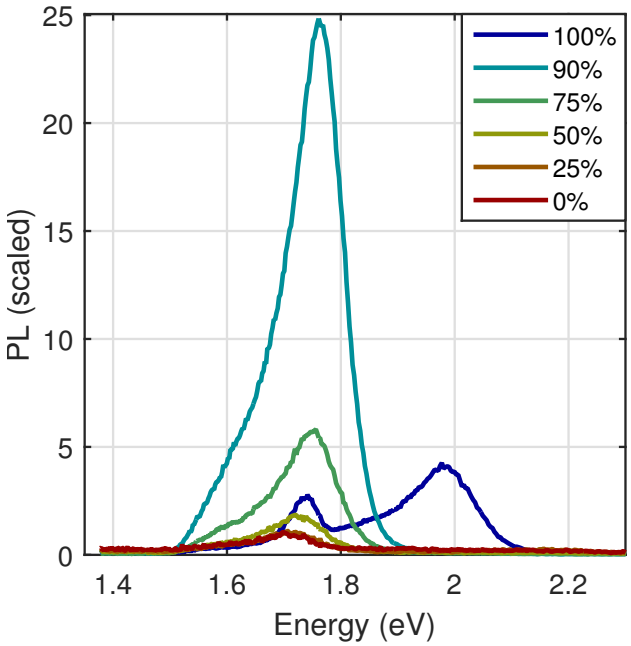

Figure 5.4: Scaled photoluminescence spectrum of SubPc/SubNc thin films upon excitation by 2.48 eV light.

For photoluminescence measurements, films were excited with 2.48 eV light, on the higher energy shoulder of the SubPc absorption feature but corresponding to a spectral region with relative low SubNc absorption. Figure 5.4 depicts the photoluminescence intensity for each of the film ratios. PL intensity was first scaled by the amount of light absorbed at the excitation frequency and then normalized relative to the integrated photoluminescence

area of the neat SubPc film emission. The neat SubPc film (plotted in blue) emits most strongly at 2 eV, broadly tailing off towards the near-IR. Neat SubNc (shown in red) emits very weakly, peaking at 1.7 eV, likely a result of the very reduced photon absorption at 2.48 eV compared to SubPc.

The photoluminescence spectrum is dramatically changed upon incorporation of as little as 10% SubNc (plotted as light blue) into the film mixture. The emission at 2 eV from SubPc is nearly completely extinguished, replaced with a large peak at 1.7 eV. This suggests highly efficient energy transfer from SubPc to the SubNc molecules. A similar trend is observed in the 75% SubPc film, though the intensity of the emission band is reduced. While the number of potentially emissive SubNc molecules is increased in the 75% SubNc film, the reduction in absorbing SubPc chromophores means fewer excitons would ultimately be funneled to SubNc, resulting in reduced emission. This trend in reduced total energy transfer continues at lower ratios of SubPc, as the absorption efficiency at 2.48 eV decreases further.

5.3.2 Pump-Probe

In Chapter 4, it was shown that experimental conditions with high excitation densities resulted in rapid exciton annihilation. This process resulted in the deposition of heat within molecules in the ground electronic state, producing shifts in ground state absorption that manifested themselves in pump-probe signals. The same considerations remain valid here. Exciton annihilation will result in thermal signatures on both timescales and of magnitudes

comparable to pump-probe experiments. Moreover, the situation in the case of optically active host and guest material is much more complicated than that of the wide band-gap host. As the amount of SubPc was diluted in the UGH2 matrix, excess vibrational energy could be deposited in neighboring UGH2 molecules. The shifts in steady state absorption of UGH2 were not detected by previous experiments because UGH2 does not absorb strongly in the visible region of the electromagnetic spectrum. The solid state solvation effect results in shifting of the SubNc and SubPc absorption, which also manifests in offset transient features. Pump-probe spectra of the mixed films will therefore have, at a minimum, four spectral components: excitonic signals from both SubNc and SubPc, as well as thermal contributions from both.

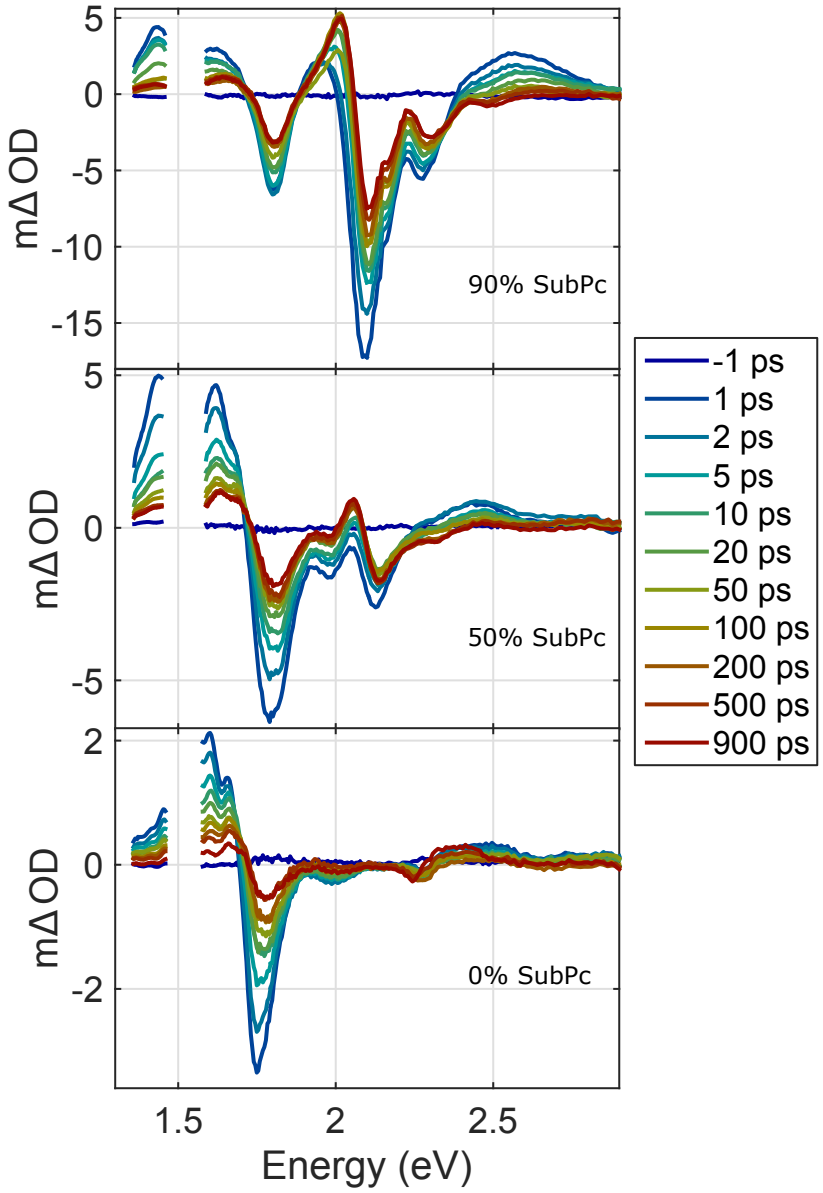

Figure 5.5: Selected full-frequency pump-probe spectra upon 2.36 eV photoexcitation. Top: 90% SubPc. Middle: 50% SubPc. Bottom: 0% SubPc. Each color trace depicts the pump-probe spectrum collected at the probe delay time indicated by the legend.

Mixed films of SubNc and SubPc were excited at both 1.98 eV and 2.36 eV, the former photon expected to predominantly generate excitons on SubNc and the latter on SubPc. In practice, direct photo-excitation of both molecules occurred at both pump energies. Figure 5.5 depicts the full-frequency pump-probe spectra upon 2.36 eV photoexcitation for three of the film compositions. The spectral shapes and general features are for the most part unaffected by choice of pump frequency. The spectra consist of two main negative features: the ground state hole (GSH) of SubNc, peaking at approximately 1.75 eV, and the GSH of SubPc, peaking at 2.1 eV. The relative strength of these two features depends on the relative concentrations of SubNc to SubPc within the film which exist in an excited state (either electronically excited as an exciton or thermally excited as a hot ground state). The spectra also possess several ESA bands, one arising from predominantly SubNc contributions at probe energies below 1.6 eV and a SubPc ESA above 2.3 eV. In the neat SubNc film (0% SubPc), small contributions to the ESA at 2.3-2.5 eV are also observed. The SubNc spectra features appear to undergo a less pronounced shift as probe delay time is increased compared to the SubPc spectral features. This could imply more efficient thermalization of excess heat released in exciton-exciton annihilation, with heat rapidly diffusing out of the probe beam waist, or it could imply that the temperature dependence of the steady-state absorption spectrum is markedly less in SubNc than in SubPc.

In order to compare the excited state processes occurring within the films, the amplitude of the SubNc and SubPc GSH features are monitored as a function of probe delay time. The decays of these features are plotted in Figures 5.6 through 5.9.

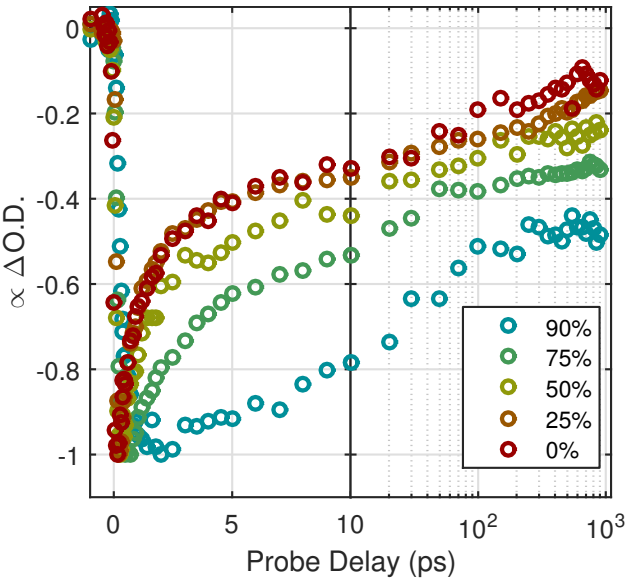

Figure 5.6: SubNc feature transient decay upon excitation by 2.36 eV light. Each circle color depicts a different film, described in the legend as weight percent SubPc.

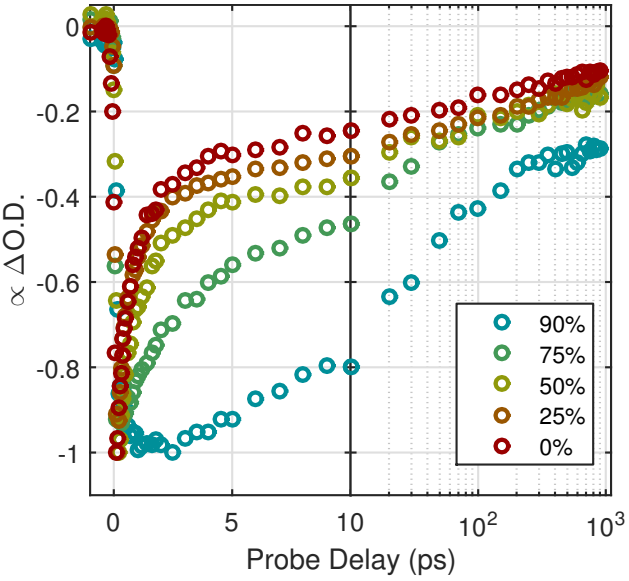

Figure 5.7: SubNc feature transient decay upon excitation by 1.98 eV light. Each circle color depicts a different film, described in the legend as weight percent SubPc.

In the 0% SubPc film, containing only SubNc, 70-80% of the initial signal intensity has decayed within the first 10 ps. This is in contrast with the relatively long lifetime observed for SubNc in dilute solution.[155] This fast decay is consistent with exciton-exciton annihilation.[45,156] As the concentration of SubNc in the film is decreased, the decay of the SubNc signal is slowed. This differs from the general behavior of SubPc when diluted in UGH2 as reported in Chapter 4, in which the apparent decay accelerated before slowing down. In SubPc, this was attributable to the growth of the thermal component in each film composition. There are two possible explanations for the behavior observed here. First, the SubNc signal decay may be slowed as excitons transfer from SubPc to SubNc, providing an

additional generation of GSH. The second potential explanation could be that annihilation of excitons on SubNc occurs at a reduced rate due to decreased exciton diffusion. The reduction in exciton mobility coupled with lower SubNc concentrations would result in reduced exciton annihilation, and consequently longer-lived transient features.

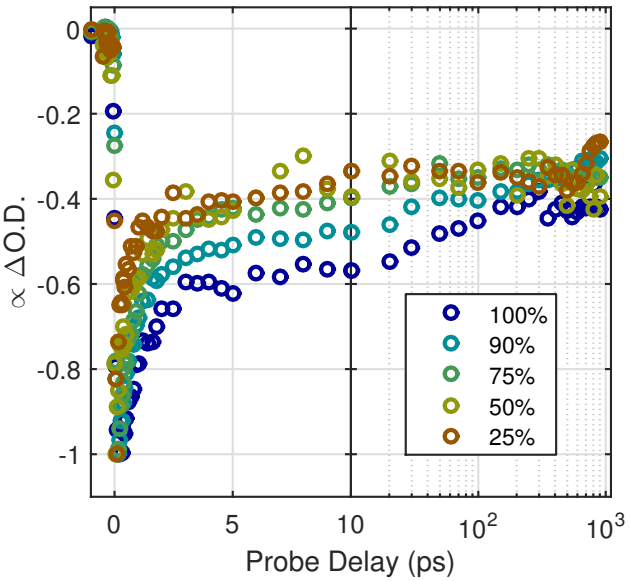

Figure 5.8: SubPc feature transient decay upon excitation by 2.36 eV light. Each circle color depicts a different film, described in the legend as weight percent SubPc.

When excited by 2.36 eV pump photons, the SubPc signal in the mixed films undergoes a rapid initial decay, and then a much slower decay after approximately 3 ps. As the weight percentage of SubPc is decreased, the initial signal is reduced more rapidly, suggesting that additional decay pathways from the excited state become present. One such potential decay pathway includes energy transfer from SubPc to SubNc. At longer delay times, the ratio

of the SubPc signal to that of the initially generated signal converges to approximately 0.4 for each of the film compositions. This suggests that vibrational energy is thermalized over the SubPc molecules, even after electronic energy transfer.

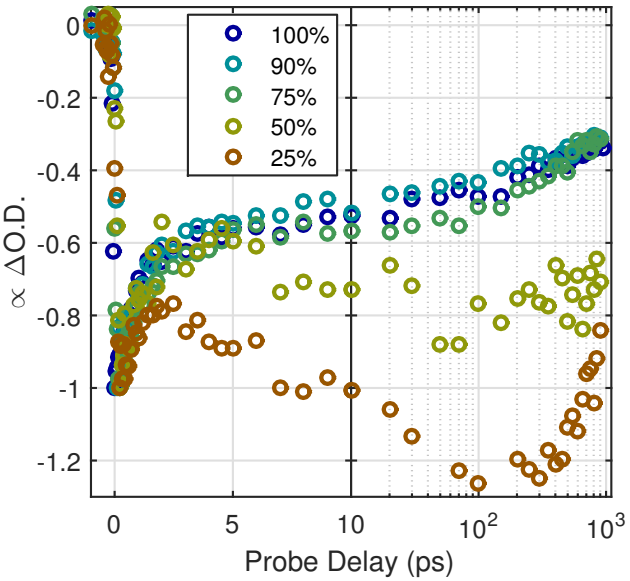

Figure 5.9: SubPc feature transient decay upon excitation by 1.98 eV light. Each circle color depicts a different film, described in the legend as weight percent SubPc.

Upon 1.98 eV photoexcitation, the dynamics of the SubPc signal paint a different picture. At high concentrations of SubPc (>50%), a significant amount of direct excitation of SubPc is responsible for the initial transient signal. Exciton annihilation and energy transfer to SubNc, coupled with a growth of a thermal contribution, result in similar decay profiles. At 50% SubPc and below, the decays begin to diverge, leveling out and in the case of 25% SubPc, even increasing in signal amplitude. At these ratios, a substantial portion of

the incident light is absorbed by SubNc, and direct excitation of SubPc molecules is limited. Because the energy gap between SubNc and SubPc is sufficiently large, excitons generated on SubNc cannot migrate to SubPc via energy transfer. The increase in SubPc signal must therefore be thermal in nature, a result of vibrational energy from SubNc exciton annihilation thermalizing over SubPc molecules. When excited by 2.36 eV, substantial exciton population is still generated on the SubPc molecules, even at low concentrations.

The steady state absorption spectra of SubNc and SubPc overlap significantly between 2.05-2.25 eV. Additionally, solid-state solvation effects cause the absorption features to shift when mixed films are prepared. The thermal contribution for each individual component cannot be readily determined simply by temperature dependent measurements of the steady-state absorption of the mixed films due to this overlap. Moreover, temperature dependent steady-state spectra assume a uniform distribution of heat throughout both molecules within the film, a condition not guaranteed on ultrafast time scales. As exciton annihilation occurs, energy is released in the form of vibrational energy. This energy need not be uniformly distributed over the constituent molecules at any given point. For example, if photoexcitation generates excitons on SubPc molecules, the vibrational energy might be immediately released upon exciton annihilation, to be absorbed by the other SubPc molecule involved in the annihilation process. At this point, the contribution to the thermal signature in SubPc would exist, whereas it would not yet exist for SubNc. As the energy is thermalized, it may be distributed to neighboring SubNc molecules. In other words, on ultrafast time scales SubPc and SubNc might not be experiencing the same

"temperature." Using one steady-state differential spectrum imposes the restriction that the amplitude of the SubPc thermal signal is constant relative to the SubNc thermal signal. The heat from annihilation will eventually thermalize, yielding transient spectra comparable to that of the steady-state temperature differential spectrum, but in the interim time scales the differential spectrum cannot be used.

Interpretation of the mixed films is therefore limited to probe delay times when thermal contributions are expected to be small or negligible. Fortuitously, this allows us to examine energy transfer from SubPc to SubNc in at least one composition of mixed films.

5.3.3 SubPc to SubNc Energy Transfer

The 90% SubPc film provides a meaningful venue for investigating energy transfer from SubPc to SubNc. The early time dynamics for the rise of the SubNc signal in the 90% SubPc films were fitted with a single exponential rise convoluted over the instrument response. The fit was given by the functional form shown in Equation 5.1.

$$S(t) = C\left(1 - e^{-\frac{t}{\tau}}\right) \tag{5.1}$$

Figure 5.10 plots the early time rise signal for 2.36 eV excitation (blue circles) and 1.98 eV excitation (red circles). An instrumental response is shown as the dashed green line. The signal continues to grow in outside of the excitation pulse width, suggesting that the additional growth in signal intensity is due to energy transfer from SubPc to SubNc.

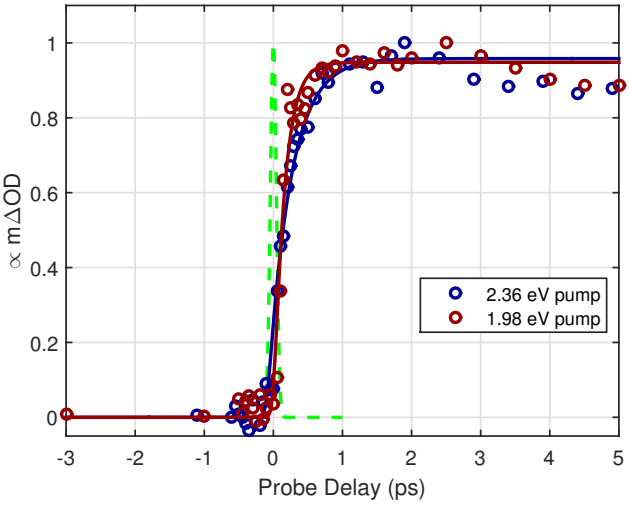

Figure 5.10: Early time rise dynamics of SubNc signal in 90% SubPc film. The signals are plotted as the negative of the measured signal and scaled to a maximum value of 1. Blue: 2.36 eV pump. Red: 1.98 eV pump. The green dashed line indicates the temporal profile of the pump.

Values of 960±20 fs and 950±20 fs were obtained for τ for the 2.36 eV and 1.98 eV photoexcitation signals, respectively. These values agree very well, though the slightly faster rise upon 1.98 eV photoexcitation may be explained by a slightly greater amount of direct photoexcitation of SubNc by the pump beam. To test whether this might be energy transfer from SubPc, the early time dynamics of the SubPc GSH were fitted with a single exponential decay. The results of these fits yielded values of τ equal to 970±20 fs and 900±20 fs for 2.36 eV and 1.98 eV photoexcitation, respectively. While it is inevitable that exciton annihilation is occurring over this time scale, the similar timescales of the fits

do suggest a correlated process, and that Förster energy transfer is a plausible mechanism explaining the delayed growth of the SubNc feature. Other studies have also reported Förster-like energy transfer with time constants on the order of 1-2 ps.[157] Interestingly, the rate of self-Förster transfer in neat SubPc films has a time constant of approximately 5.3 ps, which is roughly 5 times slower than the rate of energy transfer observed here.[129] The greater spectral overlap between SubPc emission and SubNc absorption generates a larger Förster Radius, increasing the energy transfer efficiency when compared to neat SubPc.

In thin films of neat SubPc, the radiative rate of decay has been observed to be 20×10^6 s^{-1}.[129] We can calculate the Förster Radius R_0 for energy transfer from Equation 1.25.[38] The distance r between the donor and acceptor can be estimated from the Wigner-Seitz radii of the two molecules in neat films, 0.47 nm in neat SubPc and 0.53 nm in neat SubNc. The separation r between the the two is given as the sum of the two radii, 1 nm. Using 1/950 fs^{-1} as the Förster energy transfer rate, and the values previously stated, we obtain for R_0 a value of 6.1 nm. This is in good agreement with the value for R_0 of 7.5 nm previously determined for energy transfer from SubPc to SubNc in planar heterojunctions.[140]

5.3.4 Exciton Annihilation in neat SubNc film

While disentangling the thermal and electronic contributions to the transient signal may prove intractable for the SubPc/SubNc mixed films, the neat film of SubNc may still be reasonably separated into electronic and thermal components. Using the method described

in Chapter subpcchapter, the thermal and excitonic components of the transient spectra can be deconvoluted. The coefficient of the electronic component at each probe delay time can be fitted with a 3D-diffusion limited exciton annihilation model, where, as before, only the diffusion coefficient D is optimized. The excitonic coefficient component and the resulting fit is shown in Figure 5.11. This results in a 3D-diffusion length L_{3D} of 14.2±1.8 nm. Previous measurements for the diffusion length in neat SubNc thin films yielded an approximate diffusion length of 11 nm.[144]

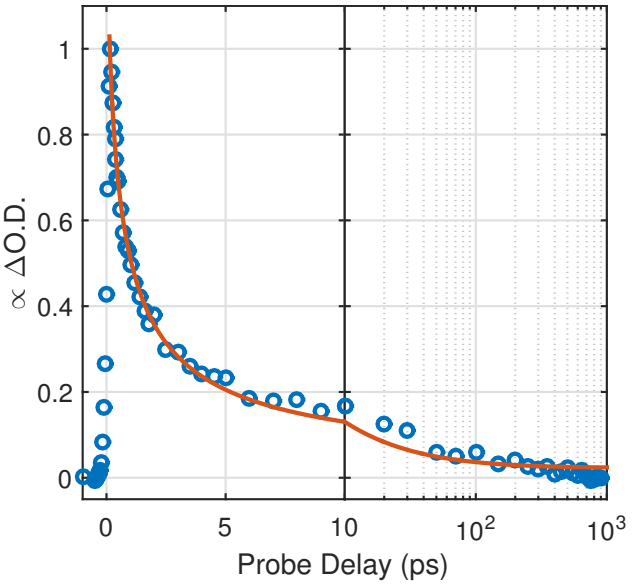

Figure 5.11: SubNc electronic component fitted by a 3D-diffusion limited annihilation model.

5.4 Conclusions

The ultrafast dynamics of mixed SubPc/SubNc films following photoexcitation at 1.98 and 2.36 eV were characterized. In neat SubNc films, the diffusion length was determined to be 14 nm, agreeing with previous measurements.[144] The time constant for Förster energy transfer from SubPc to SubNc was determined to be 1 ps. Coupled with the photoluminescence measurements, this suggests that energy transfer from SubPc to SubNc is in fact very efficient. The decreased device efficiency observed in the OPVs containing a single mixed donor layer as compared to those devices employing a cascade architecture containing multiple donor layers is thus likely due to a reduction in the energy transfer rate from SubNc to other SubNc molecules in the SubPc/SubNc mixed films. Dilution of SubNc in SubPc appears to result in a blueshift of the SubNc absorption feature, which could reduce overlap with SubNc emission, effectively reducing the SubNc self-Förster Radius and diminishing further exciton diffusion after the initially highly favorable energy transfer from SubPc to SubNc. However, the shift is small (<0.02 eV), and the reduction in exciton diffusion may not entirely be due to reduced R_0 in SubNc.

Separating the thermal and electronic contributions in the transient absorption spectra of mixed films remains an important hurdle to overcome in order to increase understanding of how the dilution of SubNc in SubPc affects exciton transport, in particular transport that occurs after the initial energy transfer from SubPc to SubNc. Obtaining temperature dependent steady-state spectra of SubNc and SubPc diluted in wide band-gap UGH2,

which does not absorb light strongly in the visible region, may be one avenue towards obtaining the independent signatures of the thermal signals of SubNc and SubPc to the transient spectra.

Additionally, exciting with lower photon energy pumps may provide a path to generate the excitonic component of SubNc alone in the mixed films. At the time of these experiments, the NOPA used to generate the pump beam was limited in the photon energy it could successfully amplify. This resulted in generation of photons that would directly photoexcite SubPc, even at 1.98 eV pump energy. Moving to lower frequency photons would allow for only photoexcitation of SubNc to occur. Because energy transfer from SubNc to SubPc is not favorable, any SubPc signals that arise would be due to SubNc exciton annihilation followed by thermal energy transfer, and the initial transient signal prior to exciton annihilation would be comprised only of the SubNc excitonic component. This may provide an effective means to reduce the number of signal sources, simplifying interpretation of transient spectra and allowing a means to probe exciton migration between SubNc molecules in the mixed films. Since only SubNc excitons will be generated, it will allow for completion of the understanding of how exciton transport in SubPc/SubNc mixed films is impacted after the initial step of energy transfer from SubPc to SubNc.

Chapter 6

Novel Boron Dipyrromethane Derivative Excited State Dynamics and Photoluminescence Quenching

6.1 Introduction

Boron dipyrromethane (BODIPY) (IUPAC name 4,4-Difluoro-4-bora-3a,4a-diaza-s-indacene) based structures form the core of an incredibly diverse and versatile array of molecules, with applications ranging from laser dyes, electroluminescent films, fluorescent probes, and of course, light-harvesters.[158,159]

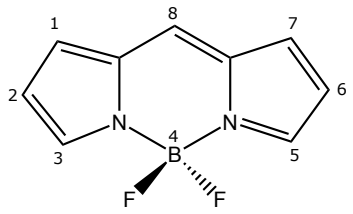

Figure 6.1: Chemical structure of the BODIPY core. α position refers to substitutions in positions 3 and 5, while β position refers to substitutions at positions 1, 2, 6, and 7. The meso position is indicated by 8.

The structure of BODIPY (Figure 6.1 allows for the creation of a variety of derivatives with custom-tailored chemical properties. Indeed, BODIPY has even been called "El Dorado" of fluorescent tools.[160] Early BODIPY based cells achieved efficiencies of 0.5-1.6%, with more promising recent research resulting in devices with 5.31% overall conversion efficiency.[161–163] Because generation of a charge separated state is a crucial component for efficient conversion of solar energy into electricity, extensive research efforts have been focused towards creating molecules and supramolecular assemblies with donor-acceptor character. A common motif for generating this charge-transfer character has been through the incorporation of ferrocene into the molecular structure. Various donor-acceptor assemblies have been created using ferrocene in such a manner, including systems such as porphyrins, subphthalocyanines, BODIPYs, and aza-BODIPYs.[164–169]. In BODIPY systems, a metal-to-ligand charge transfer band is commonly observed at low energies, <1.7 eV.[168,170,171]

This first part of this study will focus on understanding the influence of structural modifications of the BODIPY core to that of the exhibited excited state dynamics. The second part of the study, and larger overall focus, will investigate the nature supra-molecular adducts formed by the complexation of BODIPYs with buckminsterfullerene (C60) in solution. These types of complexes have received increased attention in recent years for their ability to mimic natural photosynthetic systems with light harvesting antennae.[170,172–179] Traditionally, optical techniques such as photoluminescence quenching and transient absorption spectroscopy have been used to determine the existence of these complexes.[180–182] These techniques will be used again here.

Experiments were conducted using BODIPY structures as shown in Figure 6.2.

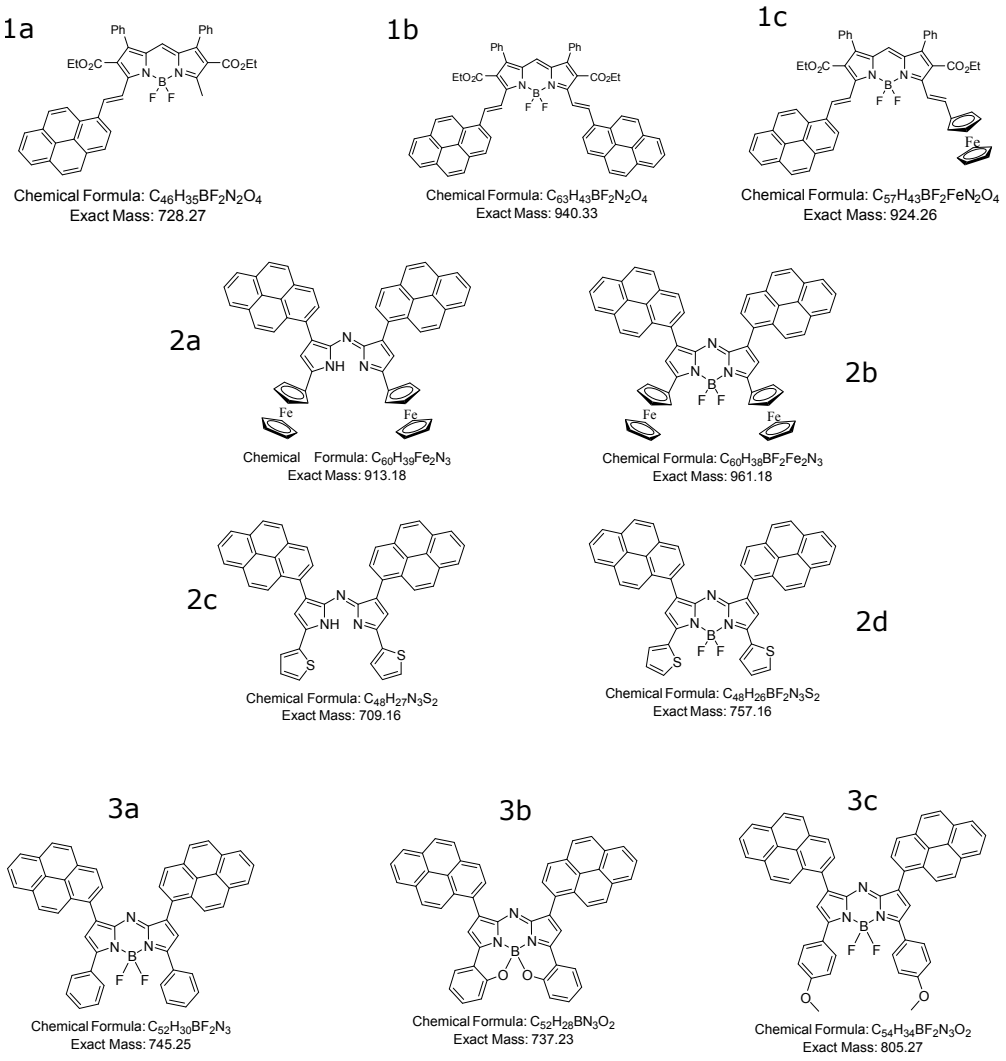

Figure 6.2: Chemical structure of the BODIPY and dipyrromethane based compounds employed in this study.

Series 1 consists of three BODIPYs with phenyl substitutions in the 1 and 7 positions and ethyl ester substituents in the 2 and 6 possessions. In the α positions (3 and 5),

the BODIPYs had vinyl-linked pyrenes attached. In order to facilitate the formation of a charge-transfer state, 1c had one of these pyrenes replaced with a vinyl-linked ferrocene moiety.

Series 2 consisted of molecules with an aza-dipyrromethane and aza-BODIPY core. In aza-BODIPYs and aza-dipyrromethanes, a nitrogen atom replaces the carbon in the meso position. The molecules in this series contain pyrenes directly bound to the core of the molecule in the β 1,7 positions and either thiophene or ferrocene moieties in the α positions.

Series 3 consists of three separate β-pyrene substituted aza-BODIPYs, each with different substituents in the α positions. 3a posseses phenyl groups, 3b posseses meta-substituted oxygens on the phenyl rings, which displace the fluorines, bonding with the chelating boron to form a fused ring system. The final molecule, 3c, possesses para-methoxy substituted phenyl groups in the α position.

6.2 Experimental

Solutions for all experiments were prepared such that the maximum OD of the BODIPYs was around 0.1-0.2 in a 1 mm quartz cuvette. This typically resulted in solutions with approximately 20 μM BODIPY concentration in toluene. For C60 fluorescence quenching experiments, samples were prepared such that samples would possess the same BODIPY concentration both with and without the presence of C60. To investigate whether or not solvent plays a role in complex formation, samples were also prepared in DCM. Due

to the low solubility of C60 in DCM, stock solutions were first prepared of the desired BODIPY and C60 in toluene, with proper volumes selected to achieve the desired mole ratios. The toluene solvent was removed through rotary evaporation, and the dried film was resuspended in DCM. Samples were sonicated to encourage complete dissolution of the C60, and UV/vis spectra confirmed the presence of C60 in solution in the appropriate quantities.

Pump-probe experiments were conducted as described previously throughout these experiments. A NOPA was used to generate 650 nm light for the pump beam, which possessed a pulse width of 75 fs as measured by cross-correlation techniques. The polarization of the pump was set to the magic angle (54.7°) relative to that of the probe polarization in order to isolate anisotropic dynamics. TCSPC experiments were conducted as described in Chapter 2, with either a 475 nm or 650 nm laser head.

6.3 Results and Discussion

6.3.1 Steady-State Photophysics

The absorption of 1a, 1b, and 1c are shown in Figure 6.3. 1a, consisting of a single pyrene, peaks at 633 nm. Addition of the second pyrene results in a shift of the absorption band by nearly 90 nm, to a peak at 722 nm. 1c possesses one peak at approximately 650 nm, similar to that of 1a. Each of these bands is assigned to an $S_0 \rightarrow S_1$ transition. In 1c, however, there is an additional absorption band peaking at approximately 728 nm and

overlapping with the $S_0 \rightarrow S_1$ transition. This low energy broad absorption feature has often been linked to a charge-transfer exciton induced by the presence of ferrocene. Also noted is the broad, structured band present at approximately 400 nm, which is assigned to the $S_0 \rightarrow S_2$ transition. While this band is present in each BODIPY in the series, the relative strength compared to the main transition band is varied, as well as the individual band structure.

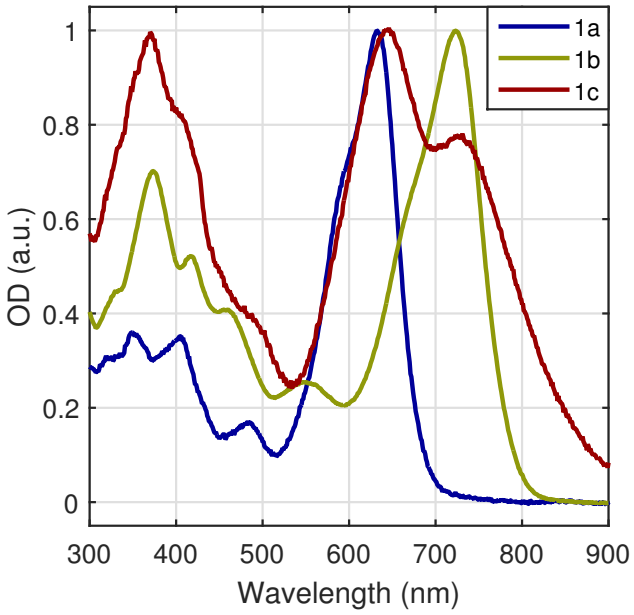

Figure 6.3: Steady state UV-Vis spectra of series 1.

The unsubstituted aza-DIPY 2c has a relatively wide $S_0 \rightarrow S_1$ absorption band, peaking at 644 nm. Upon addition of the ferocene moieties in 2a, this transition becomes obscured in a broad charge-transfer band, but appears to be blue-shifted to around 550 nm. The charge-transfer band in 2a is relatively intense, peaking at 690 nm. The unsubstituted

aza-BODIPY has a narrow absorption feature peaking at 738 nm, which upon addition of ferrocene moieties in 2b shifts the transition to approximately 640 nm. Coincidentally, the $S_0 \rightarrow S_1$ absorption band of 2b overlays with that of the unsubstituted dipyrromethane derivative, 2c. A broad charge-transfer band associated with the ferrocene peaks at 880 nm. In general, the addition of ferrocene to the aza-BODIPY and aza-dipyrromethane structures appears to shift the $S_0 \rightarrow S_1$ transition to higher energy wavelengths. The $S_0 \rightarrow S_2$ transition peaks at 345 nm in each of the molecules in this series, and appears to be relatively unaffected by the presence of the ferrocene moiety.

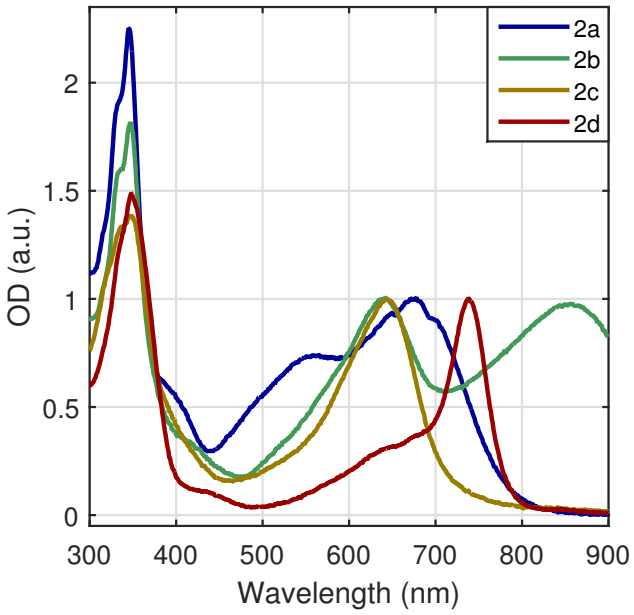

Figure 6.4: Steady state UV-Vis spectra of series 2.

In the third series, various substitions were placed on the α position of the aza-BODIPY. 3a, which has phenyl groups in the α position, exhibits an unusually broad (200 nm

FWHM) $S_0 \rightarrow S_1$ transition, peaking at 675 nm. In 3b, an oxygen on the phenyl ortho position bonds with the boron of the BODIPY core, forming a fused ring structure. This results in a substantial narrowing of the band, as well as a nearly 90 nm red-shift. 3c possesses a methoxy group at the para position of the phenyl group. The absorption here features a similarly narrow $S_0 \rightarrow S_1$ transition, but peaks at a lower wavelength, 714 nm.

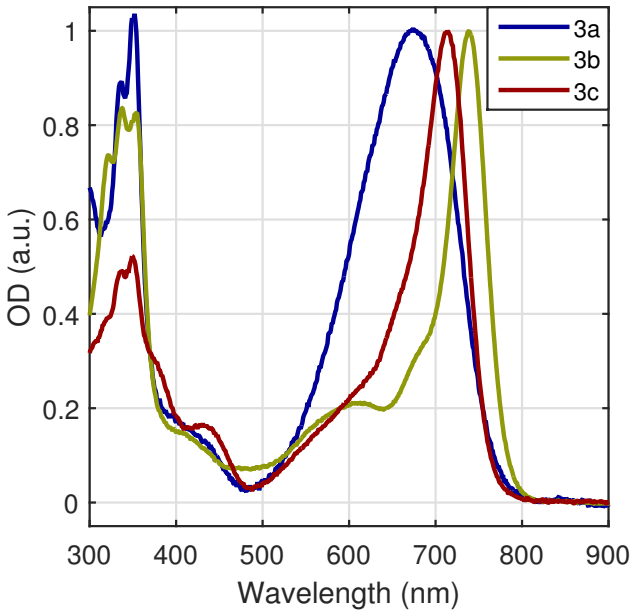

Figure 6.5: Steady state UV-Vis spectra of the series 3.

Fluorescence measurements were also conducted on each of the molecules. The fluorescence quantum yields ϕ_f are shown in Table 6.1 and were calculated in reference to Coumarin 153.[183] All of the molecules exhibit relatively low quantum yields, and little visible fluorescence, a surprising feature not typically characteristic of BODIPY based systems.[158,159] This could suggest that the additional functional groups provide a greater

number of vibrational relaxation pathways, quickly funneling the exciton away from the BODIPY core and increasing the rate of nonradiative decay. It is also noteworthy that the ferrocene substituted aza-BODIPYs exhibit ϕ_f an order of magnitude less than that of their unsubstituted analogs. This suggests that formation of a charge-transfer state which further extinguishes fluorescence as the ferrocene donates an electron to the aza-BODIPY and aza-dipyrromethane core.

Molecule	Φ_f	Molecule	Φ_f	Molecule	Φ_f
1a	0.16	2a	2.5×10^{-4}	3a	6.2×10^{-3}
1b	8.3×10^{-3}	2b	6.1×10^{-4}	3b	7.5×10^{-3}
1c	n.a.	2c	2.0×10^{-3}	3c	n.a.
		2d	0.02		

Table 6.1: The fluorescence quantum yields ϕ_f of each molecule, measured in reference to Coumarin 153 and excited at 470 nm.

6.4 Excited State Dynamics

To investigate the excited state dynamics of the BODIPYs, two techniques were used: time correlated single photon counting and ultrafast pump-probe spectroscopy. If a molecule was sufficiently emissive, then the lifetime was obtained by fitting the TCSPC traces measured at the peak emission wavelength to a single exponential decay convoluted over an instrument response. Alternatively, pump-probe spectroscopy was used to monitor the

excited state lifetimes of these materials, especially if they were not emissive or if the measured lifetimes from TCSPC were comparable to the instrument response. Generally, the molecules all possessed excited state absorption features (ESA) at wavelengths below 500 nm. The intensity of the ESA feature was monitored as a function of probe delay time, and then fitted by a single exponential decay, to generally good precision.

Molecule	τ	Molecule	τ	Molecule	τ
1a*	3.4±0.2 ns	2a*	1.9±0.4 ns	3a*	858±52 ps
1b†	2.41±0.01 ns	2b*	1.56±0.05 ns	3b†	1.60±0.02 ns
1c*	268±17 ps	2c*	44.4±2.1 ps	3c*	1.15±0.11 ns
		2d†	2.2±0.1 ns		

Table 6.2: Table presenting the various excited state lifetimes obtained for the BODIPY molecules. †Measured with TCSPC. *Measured with pump-probe spectroscopy.

In the first series, the mono-pyrene substituted BODIPY 1a possesses the longest excited state lifetime at 3.4 ns, while further incorporation of a second pyrene in 1b reduces the lifetime further to 2.4 ns. The addition of pyrene appears to increase available decay pathways when compared to the pyrene-free analog previously reported, which possessed a 6 ns lifetime.[171] Upon incorporation of the ferrocene moiety, the excited state lifetime decreases dramatically to 268 ps. Since the transient decays were well fitted by a single exponential decay, the proposed mechanism for decay in 1c from the excited state is rapid back electron transfer to the oxidized ferrocene.

In series 2, incorporation of ferrocene into the molecular structure reduces the lifetime in the aza-BODIPY 2b by approximately 700 ps when compared to the unsubstituted 2d, again suggesting back electron transfer. Curiously, in the unsubstituted azadipyrromethane 2c, rapid relaxation directly from the excited state occurs with a time-constant of 44 ps, whereas the ferrocene substituted 2a decays with a time constant of 1.9 ns. Back electron transfer to the ferrocene appears to be the rate measured in 2a. Here, the addition of the BF_2 chelating group in 2d appears to stabilize the excited state relative to that of 2c.

In series 3, the methoxy-phenyl substituted 3c exhibits a longer lifetime than 3a, which suggests that the slightly stronger electron-donating nature of the substituents better serve to stabilize the excited state than unsubstituted phenyl groups. This may enhance the ability of the exciton to delocalize across the entire molecule, forming a more stable excited state than that of 3a. The fused ring structure in 3b appears to stabilize the excited state, resulting in the longest lifetime of the three molecules in this series. Coupled with the increased quantum yield of 3b over the other molecules, the implied mechanism for the lifetime increase is a reduction in the vibrationally accessible decay pathways.

6.5 BODIPY-C60 Complex Formation

6.5.1 Pump-Probe Spectroscopy

Pump probe experiments were collected using a 30 μW pump beam centered at 650 nm. The polarization of the pump beam was rotated 54.7° with respect to the probe beam polarization. Samples were flowed through a 1 mm quartz flow cell and degassed prior to data acquisition. The resulting full frequency spectra are presented in Figure 6.6.

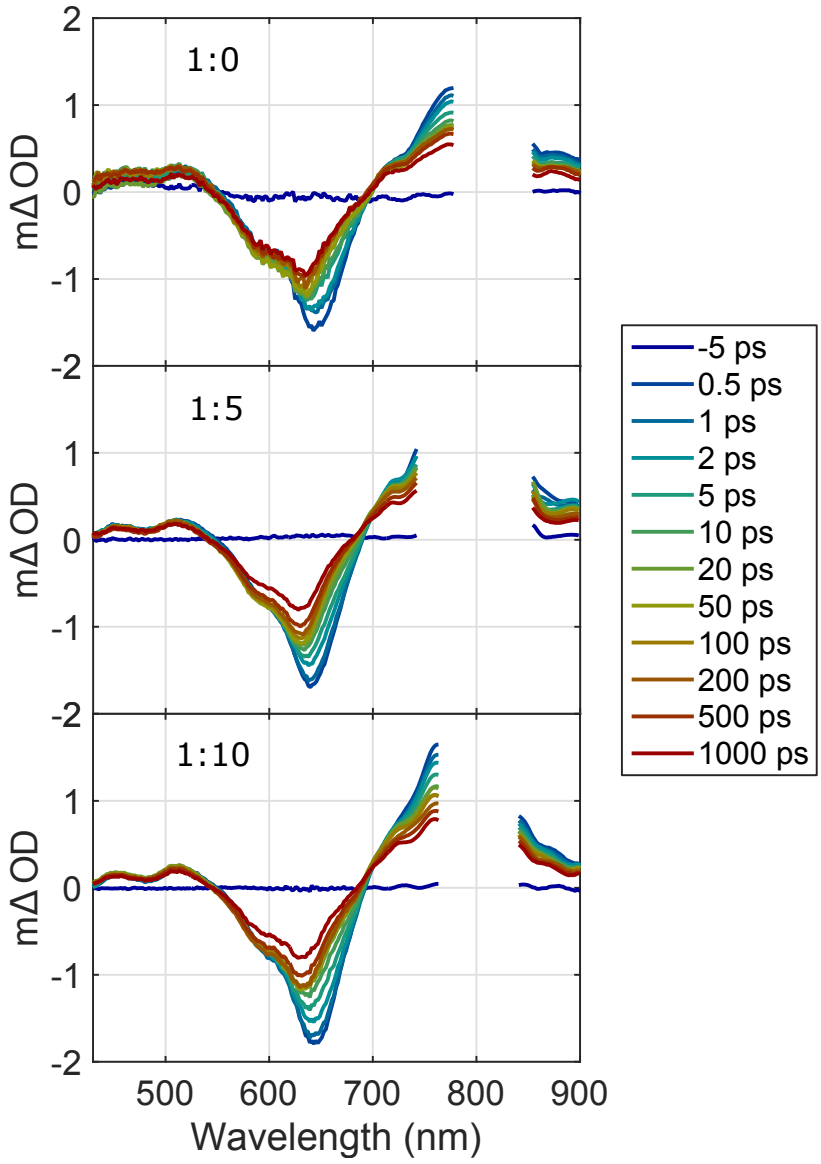

Figure 6.6: Full frequency spectra of 1a for selected time delays. Top: 1:0 1a:C60. Middle: 1:5 1a:C60. Bottom: 1:10 1a:C60.

The pump-probe spectra for all samples are qualitatively very similar, with a small

excited state absorption below 550 nm, a bleach due to missing ground state absorption consistent with the steady state UV/vis spectrum, and an excited state absorption above 700 nm. The minimum of the GSH feature shifts to lower energy wavelengths over the first 5-10 ps, likely due to spectral cooling and relaxation within the S_1 vibrational manifold. The transient features persist beyond our current maximum experimental probe delay time of 2.5 ns. Note that data is omitted where excess 800 nm light from the probe beam oversaturated the detector.

In order to test for charge transfer from 1a to C60, a quantitative comparison of the decay dynamics is necessary. To do so, the recovery of the ground state bleach was monitored at 632 nm. If electron transfer from 1a to C60 is occurring, then a slowed recovery might be observed as the electron can no longer recombine with the hole, instead depending on back electron transfer from the reduced BODIPY.

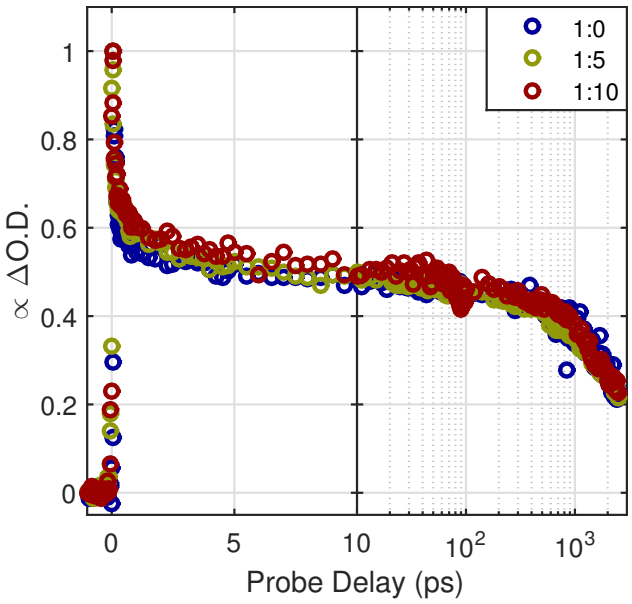

Figure 6.7: A plot of the decay of the GSB feature at 632 nm for solutions of 1a and C60. Note that the feature amplitude is normalized to a value of 1 at early times. Blue: 1:0 1a:C60. Yellow: 1:5 1a:C60. Red: 1:10 1a:C60.

As seen in Figure 6.7, the observed decay dynamics are virtually identical at each ratio of 1a to C60. At no point in the exciton lifetime do the decays appear to diverge from one another. To evaluate the lifetime of 1a, these decays were fit to a single exponential decay with no vertical offset. The resulting lifetimes are shown below in Table 6.3.

1a : C60	τ (ns)
1 : 0	3.4 ± 0.2
1 : 5	3.0 ± 0.1
1 : 10	3.1 ± 0.2

Table 6.3: The fitted lifetimes τ obtained for the differing ratios of 1a:C60 and the associated error bars of the fits at 95% confidence intervals.

Within error, the lifetimes agree well with one another and are not indicative of any strong influence due to the additional C60. To test whether the degree of complex formation depended on the nature of the BODIPY structure, pump-probe spectra were also collected for 2a:C60 and 2b:C60 solutions as well. The intensity of the ESA feature as a function of probe delay for solutions containing 1a:C60 is plotted versus that of neat 1a in solution in Figure 6.8, while the analogous plot for 2b is presented in Figure 6.9. As with 1a, the observed dynamics are indistinguishable upon addition of C60 at 10 times the BODIPY concentrations. For 2a, the observed lifetimes are 1.9±0.4 ns and 2.1±0.4 ns alone and in 1:10 ratios with C60, respectively. For 2b, the observed lifetimes are 1.56±0.05 ns and 1.64±0.07 ns alone and in 1:10 ratios with C60, respectively.

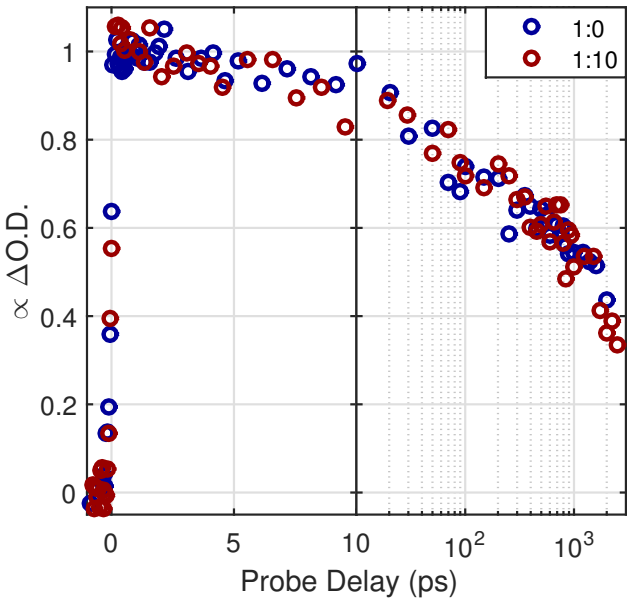

Figure 6.8: A plot of the decay of the ESA feature for 2a. Blue: 1:0 2a:C60. Red: 1:10 2a:C60.

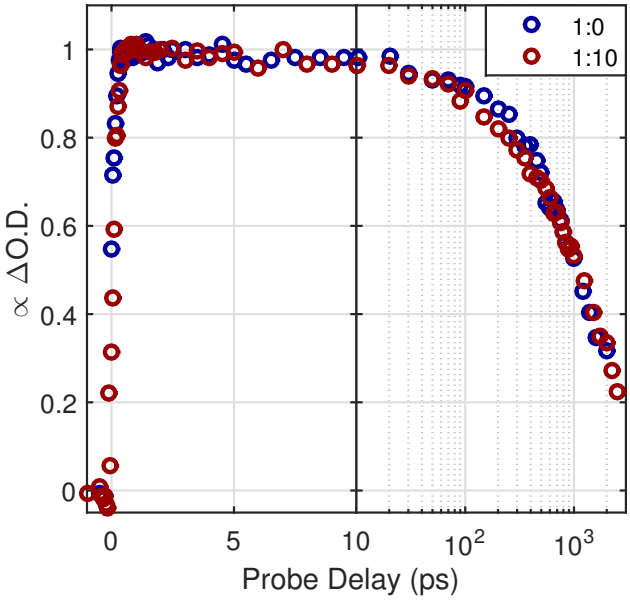

Figure 6.9: A plot of the decay of the ESA feature for 2b. Blue: 1:0 2b:C60. Red: 1:10 2b:C60.

If the contribution of a BODIPY-C60 complex to the observed transient signal is small, owing to either a low population of complex or excited state dynamics similar to that of the uncomplexed BODIPY, it might be masked by the constraints of single-exponential curve fitting. In order to test the sensitivity of a single-exponential decay model to the presence of secondary decay pathways, an artificial signal was introduced into the data in varying quantities according to the expression given in Equation 6.1.

$$S'(t) = (1 - X)\, S(t) + X e^{-t/\tau_e} \tag{6.1}$$

Here, X is the weighted fraction of the artificial component, $S(t)$ is the intensity normalized experimentally measured transient decay signal, and τ_e is a the lifetime of the decay for the artificial component. The resulting modified signal $S'(t)$ was then fitted by a new single-exponential decay function. By evaluating the value of τ obtained for the fit of $S'(t)$, we can examine the influence of both X and τ_e. Figure 6.10 depicts the resulting analysis for an artificial component introduced into the 2b transient decay signal.

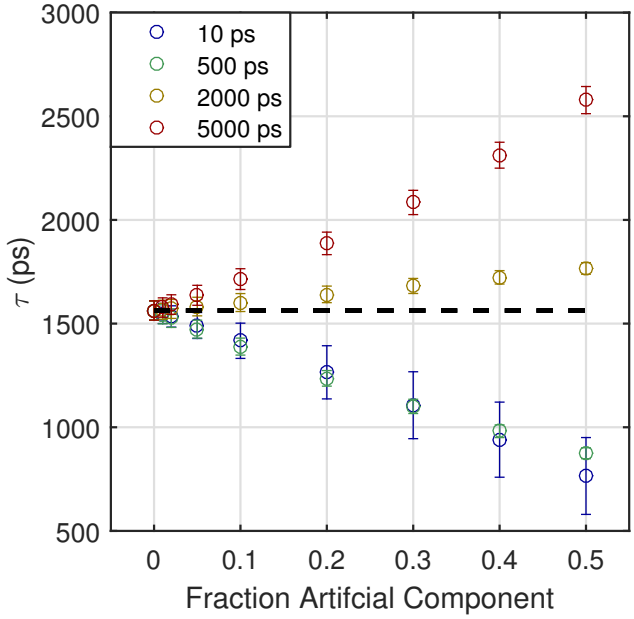

Figure 6.10: A plot of the resulting values of τ determined from the analysis of Equation 6.1 vs the fraction of the artificial component in $S'(t)$. The color of each point depicts the value of τ_e, and the error bars result from a 95% confidence interval. The dashed-black line shows the value of the measured lifetime of 2b with no artificial component introduced.

When the artificial component accounts for 5% or less of the total modified signal,

the measured lifetimes are indistinguishable (within reasonable error bounds) from that obtained by fitting the signal $S(t)$ alone, regardless of the value of τ_e. At contributions above 5%, the value of τ_e becomes important in distinguishing dynamics.

If the C60 and BODIPY are forming supramolecular complexes, then an accelerated decay of the BODIPY excited state signal might be expected, as the additional charge transfer pathways serve to depopulate the excited state. The ground state bleach recovery might be expected to recover more slowly, as the oxidized dye needs an alternative electron source, which may come from back electron-transfer from the acceptor or collisional interactions with other molecules in solution. However, previous results relying on fluorescence quenching as proof of complex formation often report nearly quantitative quenching, suggesting that the concentration of the complex should be much higher than that of the uncomplexed BODIPY, or at least comparable. D'Souza et al reported efficient (90%) energy transfer from a BODIPY-porphyrin core to a fullerene.[179]

The results here are generally indicative that BODIPY-C60 complex formation is not occurring, however there are a few scenarios where BODIPY-C60 complex formation could be occurring and remain consistent with our observed dynamics. One option is that the energy transfer from BODIPY to C60 could occur faster than our instrumental time resolution (within 80 fs of initial excitation), with the remaining signal coming entirely from uncomplexed BODIPY; however, the signal amplitudes in series of 1a:C60 solutions are nearly identical under the same experimental conditions (identical pump beam fluences,

beam waists, and BODIPY concentrations), which suggests that the number of uncomplexed BODIPY molecules is the same between the different solutions in the series, which would not be true if complex formation occurred. An alternative possibility is that the excited state decay dynamics of BODIPY-C60 complexes are identical to that of the uncomplexed BODIPY, but this must hold true for several different variations of BODIPY chemical structure.

6.5.2 Photoluminescence Extinguishing by the Inner-Filter Effect

Ultrafast measurements on solutions of BODIPY and C60 did not provide evidence for supra-molecular complex formation. Steady-state fluorescence quenching has previously been employed to determine the efficiency of supra-molecular complex formation.[179]

It is important to first distinguish between fluorescence quenching, which refers to physical or chemical interactions which reduce the fluorescence quantum yield of a molecule, and inner filter effects, which refer to experimental conditions which result in fluorescence is extinguished. Fluorescence quenching may include a number of fundamental processes inherent to the system which serve to activate other decay channels for molecules which absorb light, such as internal conversion, collisional deactivation, and of course, energy transfer from a luminescent molecule to one that is not luminescent (such as C60). Inner filter effects serve only to reduce the intensity of luminescence, typically by absorption of the excitation and emission photons.[55]

Competitive absorption by the C60 will serve to reduce the observed fluorescence of

the various BODIPY molecules. The non-negligible absorption of incident excitation light means that molecules at the back of the cuvette will be exposed to a lower intensity of light than those at the front, which will serve to reduce the observed fluorescence. The absorption of excitation light is known as the primary inner filter effect and is a well-recognized phenomenon.[56,184–187] In practice, a number of methods have been used to address this experimentally.[188–191] More typically, a mathematical correction factor is applied to adjust the observed fluorescence and calculate a corrected fluorescence.[192–197]

A simplified derivation of the correction factor is replicated here. By definition, the rate of emission of fluorescence, F, is equal to the product of the quanta of light absorbed I_A and the fluorescence quantum yield, ϕ_f. Assuming that absorption of light by the sample holder is negligible, and neglecting the effects of any reflections, we may write this expression in terms of the incident light I_0 and the light transmitted I through the sample

.

$$F = I_A\phi_f = (I_0 - I)\phi_f = I_0\left(1 - \frac{I}{I_0}\right)\phi_f \tag{6.2}$$

Using Equation refeq:odfrominstrumentation, Equation 6.2 may be recast in terms of the parameters used for calculating optical density (OD).

$$F = I_0(1 - e^{-\ln(10)\epsilon c l})\phi_f \tag{6.3}$$

Here, ϵ is the decadic molar absorption coefficient of the system at the excitation wavelength, c is the sample concentration, and l is the path length through the cell. Equation 6.3 can be expanded as a Taylor series about the exponent.

$$F = I_0(1 - 1 + \ln(10)\epsilon cl - (\ln(10)\epsilon cl)^2/2! - (\ln(10)\epsilon cl)^3/3! + \mathrm{O}((-\ln(10)\epsilon cl)^4)\phi_f \quad (6.4)$$

For dilute solutions, $\ln(10)\epsilon cl$ is small (<0.01), and the higher order terms can be neglected. This results in Equation 6.5, an expression for F that is linear with OD.

$$F = I_0 \ln(10)\epsilon cl\phi_f \quad (6.5)$$

When samples have a greater concentration, and consequently absorb more of the excitation light, the linear relationship between F and OD is lost, and Equation 6.3 must be employed instead. The correction factor is used to calculate what the fluorescence would be if it maintained a linear relationship with the sample OD. The ratio of the corrected fluorescence F_c to that of the observed fluorescence F_o under conditions of the primary inner filter effect is given by equation 6.6.

$$\frac{F_c}{F_o} = \frac{\ln(10)\epsilon cl}{1 - e^{-\ln(10)\epsilon cl}} = \frac{\ln(10)OD(\lambda_x)}{1 - 10^{-OD(\lambda_x)}} \quad (6.6)$$

Here, $OD(\lambda_x)$ is the optical density over the entire sample cell at the excitation wavelength λ_x. There are a few things to note with this correction factor. First, it assumes that

emission from all fluorophores within the propagation of the beam are detected. Experimentally, this is often not the case, as equipment geometry often serves to mask certain regions from being excited, and certain regions from being detected. The region coinciding with fluorophore excitation and subsequent emission that reaches the detector is known as the interrogation zone. If the size of the interrogation zone is known precisely, a more accurate correction factor can be calculated using the precise cell dimensions interrogated.[55,184,194,198,199].

The secondary inner-filter effect refers to absorption of emitted fluorescence by the species in solution.[55] A similar treatment as above is employed for the absorption of emission wavelengths, and generally a second correction factor is multiplied by the primary inner-filter effect fluorescence to create the completely corrected fluorescence.[193,200] Generally, solutions for the secondary inner-filter effect are presented under the assumption of right angle fluorescence detection geometry.[193–195] Calculating a correction factor for the secondary inner-filter effect is more cumbersome when fluorescence is collected in a front-face geometry, where the interrogation zone is not as well-defined. A thorough derivation accounting for the correction of both primary and secondary inner-filter effects by a quencher for a polychromatic excitation beam is provided by Leese and Wehry, to which the reader is directed for further reading, though cautioned that Leese and Wehry do make assumptions of their own regarding the path traveled by the emitted fluorescence within the sample cell.[192] Alternatively, one may use a variation of the correction factor proposed by Lakowicz, which assumes that the fluorescence intensity detected is proportional to that

of a fluorophore situated within the center of the cell.[56] The photoluminescence from this fluorophore is assumed to be proportional to the intensity of the attenuated excitation light along a path length d_x to the center of the cell by the absorption of the other chromophores. The emission from this fluorophore is also attenuated along a path d_e, again by absorption of other chromophores. The corrected fluorescence F_c is obtained by multiplication of a correction factor with the observed fluorescence F_o.

$$F_c = F_o 10^{OD(\lambda_x)d_x/l} 10^{OD(\lambda_e)d_e/l} \tag{6.7}$$

Here, $OD(\lambda_x)$ and $OD(\lambda_e)$ are the measured OD of the entire cell length l at the excitation wavelength λ_x and emission wavelength λ_e, respectively. In a front-face collection geometry, d_e may not necessarily equal d_x (as it is indicated by Lakowicz), and in the experimental set-up employed here it is actually longer by a factor of $1/\cos(30°)$.

However, in these experiments absorption of emission by C60 is assumed herein to be negligible due to its relatively weak absorption over the BODIPY emission range, but for a more rigorous treatment this reabsorption should also be taken into account. As such, the fluorescence reported herein was corrected using Equation 6.6, though Equation 6.7 has also been employed with satisfactory results. Any reduction in photoluminescence intensity upon introduction of C60 to the sample could be interpreted as evidence of complex formation, while identical corrected fluorescence between the neat sample and sample with C60 would suggest against complex formation.

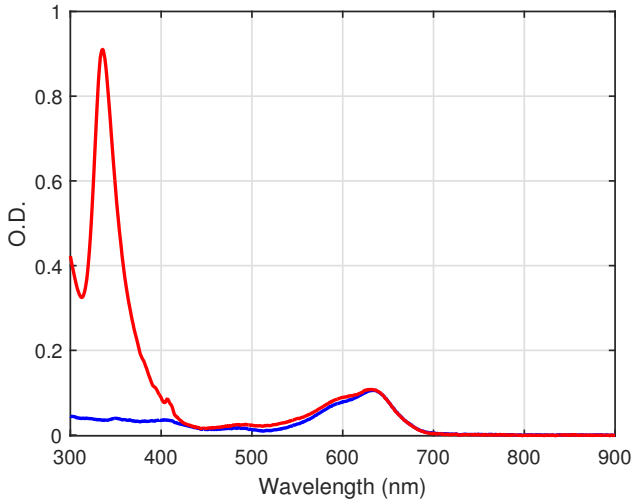

Figure 6.11: A plot of the absorption spectra of neat 1a (blue) and 1a:C60 (1:10 ratio, red) used for PL quenching experiments.

The absorption of neat 1a in solution and 1a:C60 prepared at a 1:10 ratio are plotted in Figure 6.11. The similar OD between the two samples is evidence of similar BODIPY concentrations in both samples, while the sharp peak at approximately 350 nm is indicative of the C60 presence in solution. The absorption spectrum of the 1:10 1a:C60 sample can be accurately modeled as a sum of the independent absorption spectra of 1a and C60 in solution, which suggests against spectral changes induced by aggregate formation.

Photoluminescence measurements were collected for each of these samples at two excitation wavelengths, 410 nm (Figure 6.12) and 620 nm (Figure 6.13).

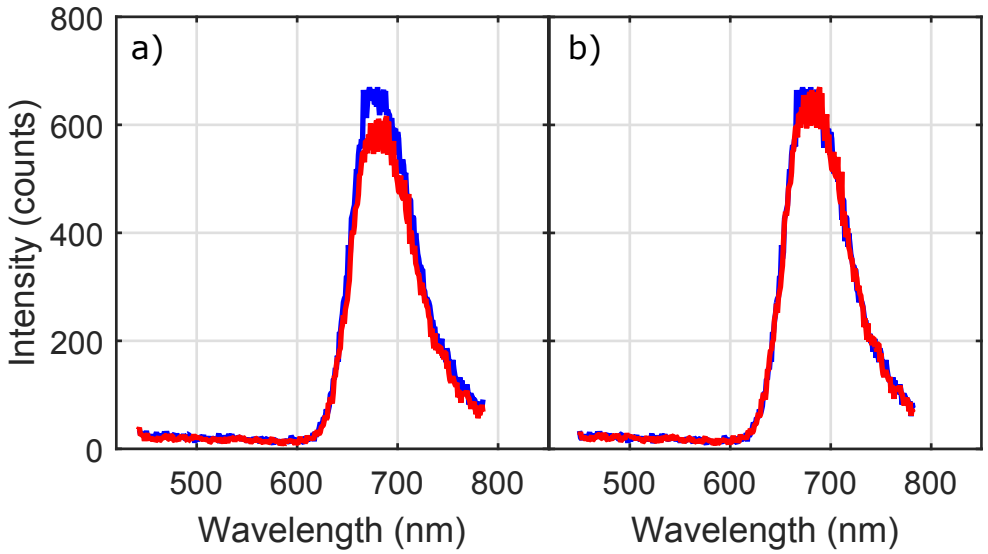

Figure 6.12: Photoluminescence of 1a upon excitation with 410 nm light. a) Plot depicting the uncorrected emission from 1:0 1a:C60 (blue) and 1:10 1a:C60 (red). b) Plot depicting the corrected emission from 1:0 1a:C60 (blue) and 1:10 1a:C60 (red).

When excited at 410 nm, the shape of the emission spectra is similar in both the neat sample and the solution containing C60 in the uncorrected emission spectra. However, the total fluorescence area of the 1:10 1a:C60 solution is approximately 90% that of the neat sample. However, this difference is completely eliminated when the correction from Equation 6.6 is applied to both samples (Figure 6.12b.).

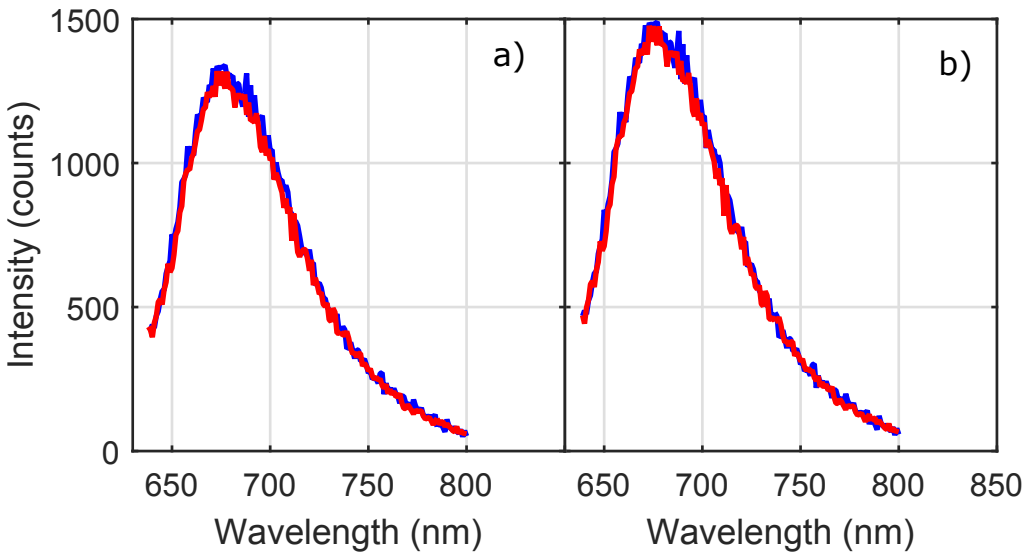

Figure 6.13: Photoluminescence of 1a upon excitation with 620 nm light. a) Plot depicting the uncorrected emission from 1:0 1a:C60 (blue) and 1:10 1a:C60 (red). b) Plot depicting the corrected emission from 1:0 1a:C60 (blue) and 1:10 1a:C60 (red).

When excited by 620 nm photons, where C60 absorbs only weakly, virtually no change in photoluminescence intensity is observed upon addition of C60. The integrated photoluminescence area agrees to within 2%, and upon correction that difference is again completely eliminated. Neither excitation wavelength provides evidence of fluorescence quenching due to complex formtion with C60, and instead suggests that the observed photoluminescence reduction is entirely due to an inner filter effect.

To investigate whether or not a charge transfer event or complex formation was mediated by the nature of the solvent, the photoluminescence experiments were repeated using

a more polar solvent, dichloromethane (DCM). The steady-state absorption spectra of the two samples in DCM are presented in Figure 6.14. The concentrations of the samples are comparable to those conducted in the photoluminescence experiments conducted in toluene.

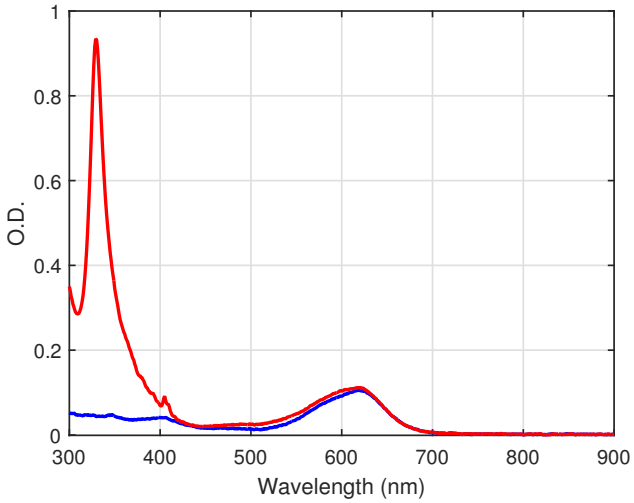

Figure 6.14: A plot of the absorption spectra of neat 1a (blue) and 1a:C60 (1:10 ratio, red) used for PL Quenching experiments in DCM.

The photoluminescence measurements conducted in toluene were repeated in DCM with near identical experimental conditions. The photoluminescence intensity in DCM appears to be reduced by approximately a factor of 5 compared to the measurements conducted in toluene. The raw and corrected fluorescence spectra for 1a and 1a:C60 are plotted for 410 nm photoexcitation (Figure 6.15) and 620 nm photoexcitation (Figure 6.16).

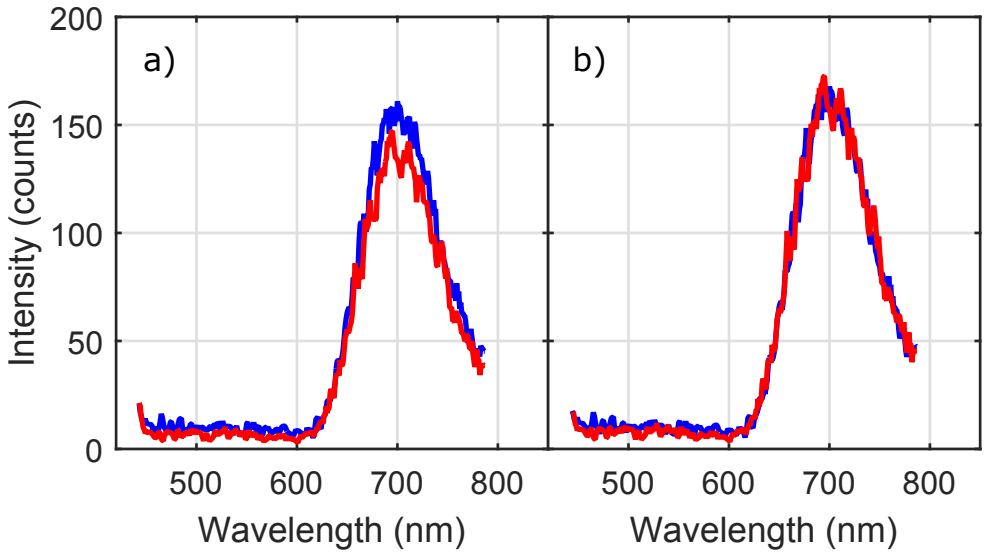

Figure 6.15: Excitation with 410 nm light in DCM. a) Plot depicting the uncorrected emission from 1:0 1a:C60 (blue) and 1:10 1a:C60 (red). b) Plot depicting the corrected emission from 1:0 1a:C60 (blue) and 1:10 1a:C60 (red).

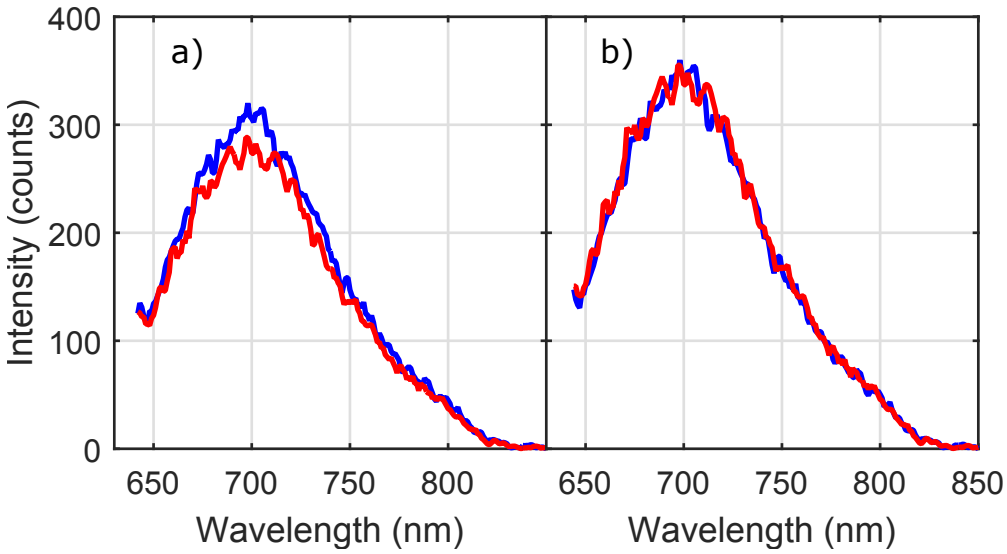

Figure 6.16: Excitation with 620 nm light in DCM. a) Plot depicting the uncorrected emission from 1:0 1a:C60 (blue) and 1:10 1a:C60 (red). b) Plot depicting the corrected emission from 1:0 1a:C60 (blue) and 1:10 1a:C60 (red).

Once again, a slight decrease in the photoluminescence count intensity is observed when a sample is prepared with C60, consistent with that observed in toluene. Again, upon 410 nm photoexcitation the ratio of the integrated photoluminescence areas of the uncorrected spectra comes to approximately 90%, a difference which is eliminated upon proper correction of the emission spectra. A similar effect is observed at 620 nm photoexcitation.

These results indicate that the choice between DCM or toluene as the solvent does not play a strong role in mediating charge transfer between 1a and C60 in solutions. There is no evidence to suggest that 1a fluorescence is quenched due to complex formation with

C60 that would result in charge transfer from 1a to the C60 molecule.

Photoluminescence experiments were also conducted in DCM using BODIPY 1b, which possessed two pyrene functional groups, which might potentially better serve to enclose the C60 and promote the formation of a supramolecular complex. Solutions were prepared for neat 1b and 1b:C60 mixtures in a 1:10 ratio, with both solutions at identical concentrations of 1b. The UV/vis spectra of both the neat and mixed 1b in a 1 mm cuvette are shown below in Figure 6.17.

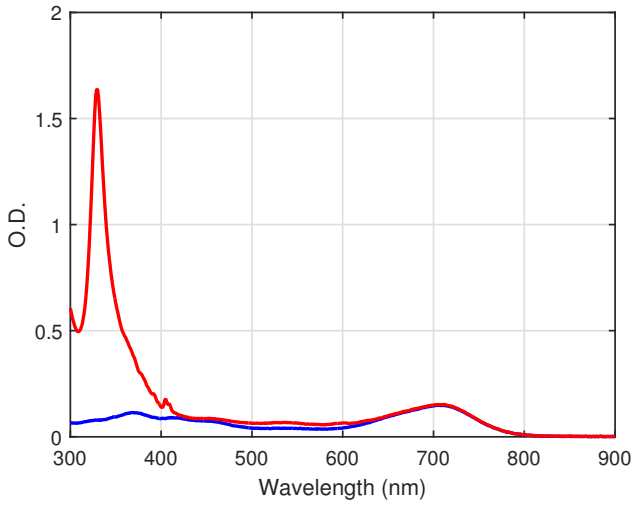

Figure 6.17: The absorption spectra of neat 1b (blue) and 1b:C60 (1:10 ratio, red) used for PL Quenching experiments.

Once again, the spectra are very similar and indicative of similar 1b concentrations. Figures 6.18, 6.20, 6.19 are the measured photoluminescence spectra of 1b and 1b:C60 mixtures excited at 370 nm, 410 nm, and 620 nm, respectively. Portions of the spectra are

omitted where the harmonic of the excitation light bled through (i.e around 740 nm for 370 nm excitation and 820 nm for 410 nm excitation). In this section, all photoluminescence experiments were conducted in a front-face geometry, consistent with the geometry employed in the 1a samples.

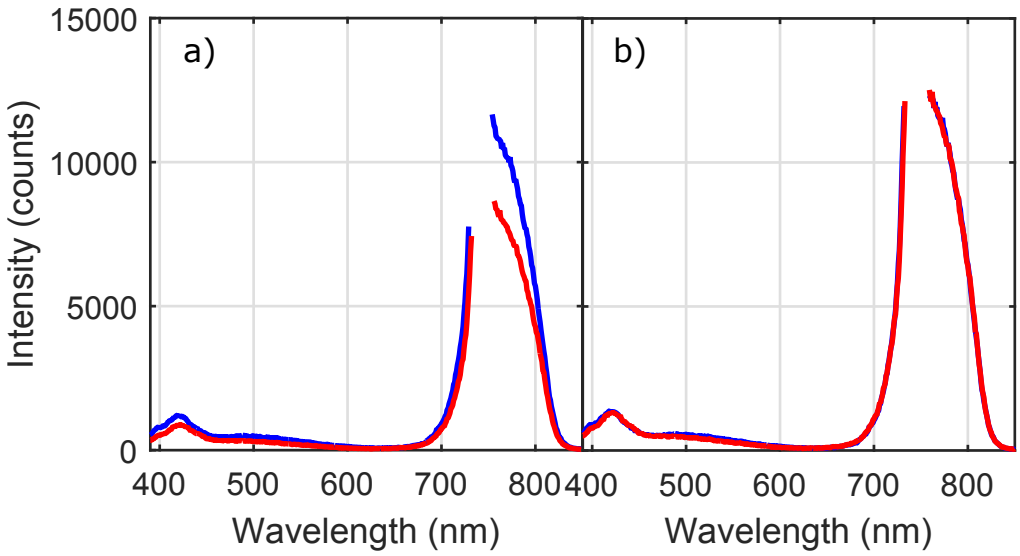

Figure 6.18: The photoluminescence spectra of neat 1b (blue) and 1:10 1b:C60 (red) upon 370 nm excitation. Spectra were collected in a front face geometry in a 1 mm cuvette.

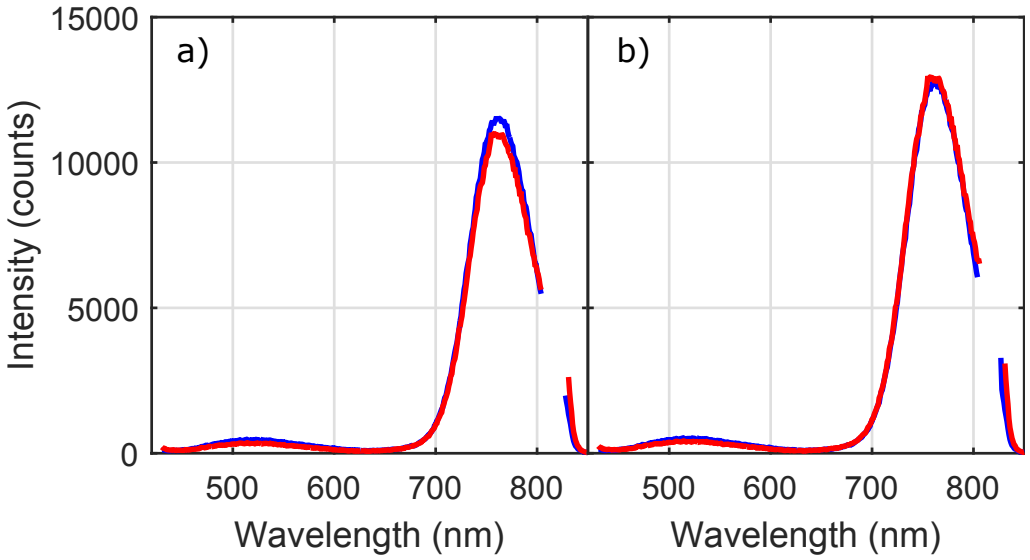

Figure 6.19: The photoluminescence spectra of neat 1b (blue) and 1:10 1b:C60 (red) upon 410 nm excitation. Spectra were collected in a front face geometry in a 1 mm cuvette.

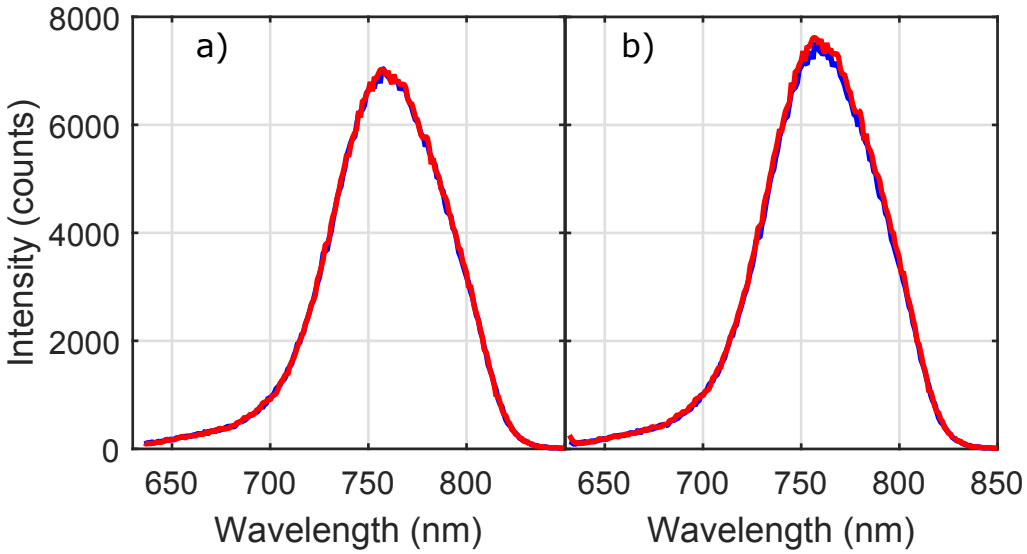

Figure 6.20: The photoluminescence spectra of neat 1b (blue) and 1:10 1b:C60 (red) upon 620 nm excitation. Spectra were collected in a front face geometry in a 1 mm cuvette.

The uncorrected data show a trend of reduced photoluminescence in the 1:10 1b:C60 samples, a difference that is amplified as the photon energy used in excitation is increased. However, as with 1a, the apparent reduction in photoluminescence is entirely eliminated once the primary inner-filter effect is taken into consideration.

We have attributed most of the reduction in fluorescence intensity due to absorption of light by C60. Conducting experiments at a higher optical density and at a right angle geometry would serve to exacerbate these effects. The same solutions used in the previous photoluminescence spectra were taken, on the same day, and placed into a 1 cm cuvette. The absorption spectra are shown below in Figure 6.21. The OD at 700 nm is approximately

1.5, which is ten times higher than that measured in the 1 mm cuvette.

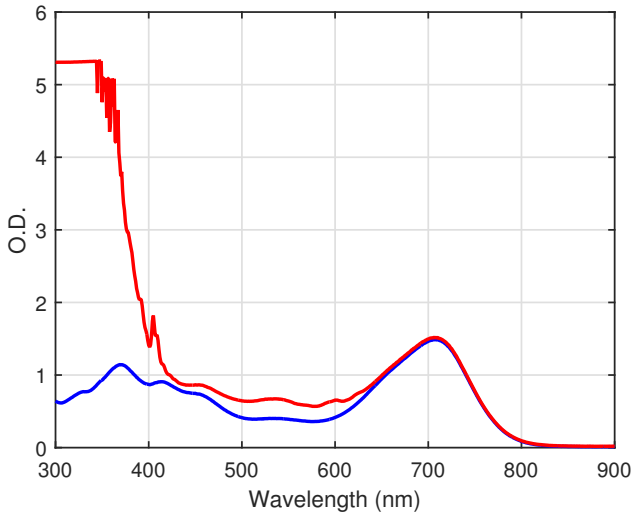

Figure 6.21: A plot of the absorption spectra of neat 1b (blue) and 1b:C60 (1:10 ratio, red) used for PL quenching experiments.

Below approximately 350 nm, the UV/Vis detector does not detect any transmitted light, manifesting in high ODs indicative of near total absorption of incident light by the C60. Note again that our concentrations of 1b and C60 are identical to the experiments conducted in a 1 mm cuvette, and the increased absorption is now due to a longer path length.

To further illustrate the effects of competitive C60 absorption of incident light, we conduct an extreme example. By exciting neat 1b at 329 nm we see photoluminescence of comparable intensity to exciting at other wavelengths. In the 1:10 1b:C60 mixed sample,

excitation at 329 nm, where C60 absorption is strongest, reduces the intensity of photoluminescence to near 0. These spectra are plotted in Figure 6.22.

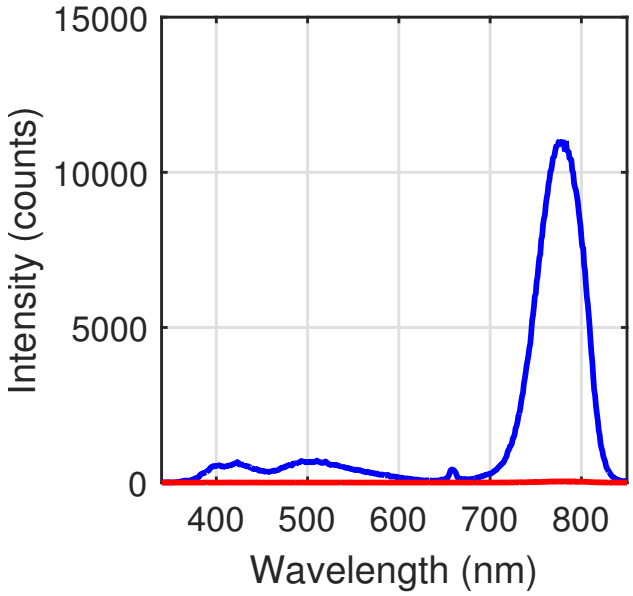

Figure 6.22: A plot of the photoluminescence spectra of neat 1b (blue) and 1:10 1b:C60 (red) upon 329 nm excitation. These measurements were collected in a right angle geometry in a 1 cm cuvette.

A substantial body of literature has emerged around the concept of self-assembled supramolecular donor/acceptor complexes, including those containing phthalocyanines, BODIPYs, and fullerenes. Many of these studies make use of photoluminescence quenching experiments to provide evidence of charge-transfer between a luminescent donor and non-luminescent acceptor, which are assumed to be non-covalently bound.

In a classic paper, D'Souza et al report on a donor/acceptor supramolecular triad allegedly featuring an imidazole-appended fulleropyrolidine non-covalently binding through metal-ligand coordination with a Zn-porphyrin-BODIPY dyad.[179] There, they report fluorescence quenching as indicative of electron transfer to the imidazole appended C60. No mention is made of any corrections which would account of the primary and secondary inner-filter effects. While our results do not disprove the formation of the self-assembled supramolecular complexes in other systems, they do suggest that similar reductions in observed photoluminescence may be attributable to a combination of inner-filter effects, sample dilution upon titration, and other phenomena unrelated to electron transfer.

6.6 Conclusion

First, a preliminary study of the excited state dynamics of three different series of BODIPYS, aza-BODIPYs, and aza-dipyrromethane derivatives was conducted using TCSPC and ultrafast pump-probe spectroscopy.

Second, the formation of supra-molecular aggregates via complexation beteween various BODIPYs and C60 fullerene was investigated. Pump-probe spectroscopy in the visible region provided no statistically significant evidence to support the formation of such complexes. Steady-state fluorescence measurements showed reduced fluorescence intensity when the solution contained C60, however the reductions were entirely attributable to inner-filter effects. The fluorescence could artificially be completely extinguished by using

non-ideal experimental sample conditions: OD>1 and a right-angle detection geometry, experimental conditions which are commonly employed in literature.[179,182] Combined, these experiments suggest that self-assembled supramolecular complexes are not formed by these BODIPYs, and provide a strong cautionary warning for proper interpretation of photoluminescence quenching experiments when ascribing the mechanism to be supramolecular complex formation.

References

[1] Shahriar Shafiee and Erkan Topal. When will fossil fuel reserves be diminished? *Energy Policy*, 37(1):181–189, 2009.

[2] EIA. September 2016 Monthly Energy Review. Technical report, U.S. Energy Information Administration, 2016.

[3] EIA. International Energy Outlook 2016. Technical Report May 2016, U.S. Energy Information Administration, 2016.

[4] Nathan S. Lewis. Powering the Planet. *Materials Research Society Spring Meeting*, 32(10):808–820, 2007.

[5] Henry N. Pollack, Suzanne J. Hurter, and Jeffrey R. Johnson. Heat flow from the Earth's interior: Analysis of the global data set. *Reviews of Geophysics*, 31(3):267–280, 1993.

[6] I.B. Fridleifsson, R Bertani, and E Huenges. The possible role and contribution of

geothermal energy to the mitigation of climate change. *IPCC Scoping Meeting on Renewable Energy Sources*, (January):59–80, 2008.

[7] International Atomic Energy Agency (IAEA). The Fukushima Daiichi Accident Report by the Director General. *Director General*, pages 1–222, 2015.

[8] Janosch Ondraczek, Nadejda Komendantova, and Anthony Patt. WACC the dog: The effect of financing costs on the levelized cost of solar PV power. *Renewable Energy*, 75:888–898, 2015.

[9] Luís Moreira Gonçalves, Verónica de Zea Bermudez, Helena Aguilar Ribeiro, and Adélio Magalhães Mendes. Dye-sensitized solar cells: A safe bet for the future. *Energy & Environmental Science*, 1(6):655, 2008.

[10] Morgan Bazilian, Ijeoma Onyeji, Michael Liebreich, Ian MacGill, Jennifer Chase, Jigar Shah, Dolf Gielen, Doug Arent, Doug Landfear, and Shi Zhengrong. Re-considering the economics of photovoltaic power. *Renewable Energy*, 53:329–338, 2013.

[11] Shelly Hagerman, Paulina Jaramillo, and M. Granger Morgan. Is rooftop solar PV at socket parity without subsidies? *Energy Policy*, 89:84–94, 2016.

[12] NREL. Best Research-Cell Efficiencies, 2016.

[13] William Shockley and Hans J. Queisser. Detailed Balance Limit of Efficiency of p-n Junction Solar Cells. *Journal of Applied Physics*, 32(3):510–519, 1961.

[14] BA Gregg. Excitonic solar cells. *The Journal of Physical Chemistry B*, 107:4688–4698, 2003.

[15] Joseph Kalowekamo and Erin Baker. Estimating the manufacturing cost of purely organic solar cells. *Solar Energy*, 83(8):1224–1231, aug 2009.

[16] Katherine A. Mazzio and Christine K. Luscombe. The future of organic photovoltaics. *Chem. Soc. Rev.*, 44(1):78–90, 2014.

[17] Michael Grätzel. Photoelectrochemical cells. *Nature*, 414:338–344, 2001.

[18] Bernard Kippelen, Jean-Luc Brédas, and Jean-Luc Bredas. Organic photovoltaics. *Energy & Environmental Science*, 2(3):251, 2009.

[19] Brian A. Gregg and Mark C. Hanna. Comparing organic to inorganic photovoltaic cells: Theory, experiment, and simulation. *Journal of Applied Physics*, 93(6):3605–3614, 2003.

[20] Thomas Kietzke. Recent Advances in Organic Solar Cells. *Advances in OptoElectronics*, 2007:1–15, 2007.

[21] Peter Würfel. *Physics of Solar Cells*. Wiley-VCH, 2005.

[22] Mary D Archer and James R Bolton. Requirements for Ideal Performance of Photochemical and Photovoltaic Solar Energy Converters. *The Journal of Physical Chemistry*, 94(21):8028–8036, 1990.

[23] Murad Jehangir Yusuf Tayebjee, Dane Robert McCamey, and Timothy W Schmidt. Beyond Shockley-Queisser: Molecular Approaches to High Efficiency Photovoltaics. *The Journal of Physical Chemistry Letters*, page 150528083027007, 2015.

[24] Sven Rühle. Tabulated values of the Shockley-Queisser limit for single junction solar cells. *Solar Energy*, 130:139–147, 2016.

[25] Cody W. Schlenker and Mark E. Thompson. The molecular nature of photovoltage losses in organic solar cells. *Chemical Communications*, 47(13):3702–3716, 2011.

[26] M. Knupfer. Exciton binding energies in organic semiconductors. *Applied Physics A: Materials Science and Processing*, 77(5):623–626, 2003.

[27] Hans Kuhn, Horst-Dieter Försterling, and David H. Waldeck. *Principles of Physical Chemistry*. John Wiley & Sons, Inc., 2 edition, 2009.

[28] S. Matthew Menke and Russell J. Holmes. Exciton diffusion in organic photovoltaic cells. *Energy & Environmental Science*, 7(2):499–512, 2014.

[29] Daniel C. Harris and Michael D. Bertoluci. *Symmetry and Spectroscopy: An Introduction to Vibrational and Electronic Spectroscopy*. Dover, 1989.

[30] NREL. Reference Solar Spectral Irradiance: Air Mass 1.5, 2017.

[31] A. Einstein. Über die von der molekularkinetschem Theorie der Wärme geforderte

Bewegumg von in ruhenden Flüssigkeiten suspendierten Teilchen. *Annalen der Physik*, 322(8):549–560, 1905.

[32] M. Smoluchowski. Zur kinetischen Theorie der Brownschen Molekularbewegung und der Suspensionen. *Annalen der Physik*, 326(14):756–780, 1906, 9811186.

[33] S. Chandrasekhar. Stochastic Problems in Physics and Astronomy. *Reviews of Modern Physics*, 15(1):1–89, 1943.

[34] Donald A. McQuarrie. *Statistical Mechanics*. University Science Books, 1st edition, 2000.

[35] Dennis G. Zill. *A First Course in Differential Equations with Modeling Applications*. Brooks Cole, 8 edition, 2009.

[36] Claude Cohen-Tannoudji, Bernard Diu, and Franck Laloë. *Quantum Mechanics*. John Wiley & Sons, Inc., 2005.

[37] Th. Förster. Zwischenmolekulare Energiewanderung und Fluoreszenz. *Annalen der Physik*, 437(1-2):55–75, 1948.

[38] E.V. Mielczarek, E.S. Greenbaum, and R.S. Knox. Intermolecular Energy Migration and Fluorescence. In *Biological Physics*, pages 148–160. Springer, 1993.

[39] V.M. Kenkre and R.S. Knox. Generalized-master-equation theory of excitation transfer*. *Physical Review B*, 9(12):5279–5290, 1974.

[40] Donald A. McQuarrie and John D. Simon. *Physical Chemistry: A Molecular Approach*. University Science Books, 1997.

[41] Michael Kasha. Characterization of Electronic Transitions in Complex Molecules. *Discussions of the Faraday Society*, 9:14–19, 1950.

[42] Jeffrey I. Steinfeld, Joseph S. Francisco, and William L. Hase. *Chemical Kinetics and Dynamics*. Prentice-Hall, Inc., 2nd edition, 1999.

[43] V.M. Kenkre. Theory of exciton annihilation in molecular crystals. *Physical Review B*, 22(4):2089–2098, 1980.

[44] V.M. Kenkre. Validity of the Bilinear Rate Equation for Exciton Annihilation and Expressions for the Annihilation Constant*. *Zeitschrift für Physik B - Condensed Matter*, 43:221–227, 1981.

[45] E. Engel, K. Leo, and M. Hoffmann. Ultrafast relaxation and exciton-exciton annihilation in PTCDA thin films at high excitation densities. *Chemical Physics*, 325:170–177, 2006.

[46] A. Suna. Kinematics of Exciton-Exciton Annihilation in Molecular Crystals. *Physical Review B*, 1(4):1716–1739, 1970.

[47] U. Gösele, M. Hauser, U. K A Klein, and R. Frey. Diffusion and long-range energy transfer. *Chemical Physics Letters*, 34(3):519–522, 1975.

[48] Mitio Inokuti and Fumio Hirayama. Influence of Energy Transfer by the Exchange Mechanism on Donor Luminescence. *The Journal of Chemical Physics*, 43(6):1978, 1965.

[49] Henning Marciniak, Xue-Qing Li, Frank Würthner, and Stefan Lochbrunner. One-dimensional exciton diffusion in perylene bisimide aggregates. *Journal of Physical Chemistry A*, 115(5):648–654, 2011.

[50] Thomas J. Pundsack. *Exciton Dynamics in Alternative Solar Cell Materials: Polymers, Nanocrystals, and Small Molecules.* PhD thesis, University of Minnesota, 2014.

[51] Douglas A. Skoog. *Principles of Instrumental Analysis.* 6th edition, 2006.

[52] Daniel C. Harris. *Quantitative Chemical Analysis.* W.H. Freeman and Company, 7th edition, 2007.

[53] David W. Allen. Holmium Oxide Glass Wavelength Standards. *Journal of Research of the National Institute of Standards and Technology*, 112(6):303–306, 2007.

[54] J. A. Gardecki and M. Maroncelli. Set of Secondary Emission Standards for Calibration of the Spectral Responsivity in Emission Spectroscopy. *Applied Spectroscopy*, 52(9):1179–1189, 1998.

[55] C. A. Parker. *Photoluminescence of Solutions.* Elsevier Publishing Company, 1st edition, 1968.

[56] Joseph R. Lakowicz. *Principles of Fluorescence Spectroscopy*. Springer, 3rd edition, 2006.

[57] Claude Rulliére, editor. *Femtosecond Laser Pulses*. 2nd edition, 2003.

[58] Andrew M. Weiner. *Ultrafast Optics*. Wiley, 1st edition, 2009.

[59] Orazio Svelto. *Principles of Lasers*. Springer, 4th edition, 1998.

[60] Frits Zernike and John E. Midwinter. *Applied Nonlinear Optics*. Dover, 2006.

[61] Herman A. Haus. Mode-locking of lasers. *IEEE Journal on Selected Topics in Quantum Electronics*, 6(6):1173–1185, 2000.

[62] Bahaa E. A. Saleh and Malvin Carl Teich. *Fundamentals of Photonics*. John Wiley & Sons, Inc., 2nd edition, 2007.

[63] Ursula Keller. Recent developments in compact ultrafast lasers. *Nature*, 424(6950):831–838, 2003.

[64] P. Weinberger. John Kerr and his effects found in 1877 and 1878. *Philosophical Magazine Letters*, 88(12):897–907, 2008.

[65] Eugene Hecht. *Optics*. Addison Wesley Longman, Inc., 4th edition, 2002.

[66] G. Cerullo and S. De Silvestri. Resonators for Kerr-lens mode-locked femtosecond Ti:sapphire lasers. *Optics Letters*, 19(11):807–809, 1994.

[67] C. Breck Hitz, J. Ewing, and Jeff Hecht. *Introduction to Laser Technology.* John Wiley & Sons, Inc., 4th edition, 2012.

[68] Robert W. Boyd. *Nonlinear Optics.* Elsevier, 3rd edition, 2008.

[69] S Backus, C G Durfee, M M Murnane, and H C Kapteyn. High power ultrafast lasers. *Review Of Scientific Instruments*, 69(3):1207–1223, 1998.

[70] David F. Underwood and David A. Blank. Ultrafast Solvation Dynamics: A View from the Solvent's Perspective Using a Novel Resonant-Pump, Nonresonant-Probe Technique. *The Journal of Physical Chemistry A*, 107(7):956–961, 2003.

[71] Nathan P. Wells, Bryan W. Boudouris, Marc A. Hillmyer, and David A. Blank. Intramolecular Exciton Relaxation and Migration Dynamics in Poly(3-hexylthiophene). *The Journal of Physical Chemistry C*, 111(42):15404–15414, 2007.

[72] Rudi Berera, Rienk van Grondelle, and John T. M. Kennis. Ultrafast transient absorption spectroscopy: principles and application to photosynthetic systems. *Photosynthesis Research*, 101(2-3):105–118, 2009.

[73] Giulio Cerullo and Sandro De Silvestri. Ultrafast optical parametric amplifiers. *Review of Scientific Instruments*, 74(1):1–18, 2003.

[74] E Riedle, M Beutter, S Lochbrunner, J Piel, S Schenkl, S Spörlein, and W Zinth. Generation of 10 to 50 fs pulses tunable through all of the visible and the NIR. *Applied Physics B*, 71(3):457–465, 2000.

[75] N. Aközbek, M. Scalora, C. M. Bowden, and S. L. Chin. White-light continuum generation and filamentation during the propagation of ultra-short laser pulses in air. *Optics Communications*, 191(3-6):353–362, 2001.

[76] A. Couairon and A. Mysyrowicz. Femtosecond filamentation in transparent media. *Physics Reports*, 441(2-4):47–189, 2007.

[77] A. Brodeur and S. L. Chin. Ultrafast white-light continuum generation and self-focusing in transparent condensed media. *Journal of the Optical Society of America B*, 16(4):637, 1999.

[78] John H. Moore, Christopher C. Davis, and Michael A. Coplan. *Building Scientific Apparatus*. Cambridge University Press, 4th edition, 2009.

[79] Volkhard May. Kinetic theory of exciton-exciton annihilation. *Journal of Chemical Physics*, 140(5):054103, 2014.

[80] Christopher A. Werley, Stephanie M. Teo, and Keith A. Nelson. Pulsed laser noise analysis and pump-probe signal detection with a data acquisition card. *Review of Scientific Instruments*, 82(12):123108, 2011.

[81] David M Jonas, Matthew J Lang, Yutaka Nagasawa, Taiha Joo, and Graham R Fleming. PumpProbe Polarization Anisotropy Study of Femtosecond Energy Transfer within the Photosynthetic Reaction Center of Rhodobacter sphaeroides R26. *Journal of Physical Chemistry*, 100(30):12660–12673, 1996.

[82] Yanmin Wang. Research Progress on Improving the Photovoltaic Performance of Polymer Solar Cells. *Journal of Solar Energy Engineering*, 134(1):011017, 2012.

[83] Hui Li, Yong-Fang Li, and Jizheng Wang. Optimizing performance of layer-by-layer processed polymer solar cells. *Applied Physics Letters*, 101:033907, 2012.

[84] Gilles Dennler, Markus C. Scharber, and Christoph J. Brabec. Polymer-Fullerene Bulk-Heterojunction Solar Cells. *Advanced Materials*, 21(13):1323–1338, apr 2009.

[85] Letian Dou, Jingbi You, Jun Yang, Chun-Chao Chen, Youjun He, Seiichiro Murase, Tom Moriarty, Keith Emery, Gang Li, and Yang Yang. Tandem polymer solar cells featuring a spectrally matched low-bandgap polymer. *Nature Photonics*, 6:180–185, 2012.

[86] Bridget Carsten, Jodi M. Szarko, Luyao Lu, Hae Jung Son, Feng He, Youssry Y. Botros, Lin X. Chen, and Luping Yu. Mediating Solar Cell Performance by Controlling the Internal Dipole Change in Organic Photovoltaic Polymers. *Macromolecules*, 45(16):6390–6395, 2012.

[87] Stephen A. Miller, Andrew C. Stuart, Jordan M. Womick, Huaxing Zhou, Wei You, and Andrew M. Moran. Excited-State Photophysics in a Low Band Gap Polymer with High Photovoltaic Efficiency. *The Journal of Physical Chemistry C*, 115(5):2371–2380, feb 2011.

[88] Natalie Banerji, Eric Gagnon, Pierre-Yves Morgantini, Sebastian Valouch, Ali Reza

Mohebbi, Jung Hwa Seo, Mario Leclerc, and Alan J. Heeger. Breaking Down the Problem: Optical Transitions, Electronic Structure and Photoconductivity in Conjugated Polymer PCDTBT and in Its Separate Building Blocks. *The Journal of Physical Chemistry C*, 116(21):11456–11469, 2012.

[89] Karan Aryanpour, Tirthankar Dutta, Uyen N V Huynh, Zeev Valy Vardeny, and Sumit Mazumdar. Theory of Primary Photoexcitations in Donor-Acceptor Copolymers. *Physical Review Letters*, 115(26):1–5, 2015, 1508.00071.

[90] In Sik Kim, Soo Young Jang, Terry Park, Cheol Jo, Dong Yu Kim, and Do Kyeong Ko. Femtosecond transient absorption dynamics in low bandgap polymer solar cell materials including poly(thienylenevinylene) derivative and benzothiadiazole moiety. *Chemical Physics*, 461:29–33, 2015.

[91] Joshua C. Speros, Bryan D. Paulsen, Bradley S. Slowinski, C. Daniel Frisbie, and Marc A. Hillmyer. Band Gap and HOMO Level Control in Poly(thienylene vinylene)s Prepared by ADMET Polymerization. *ACS Macro Letters*, 1(8):986–990, 2012.

[92] Joshua C. Speros, Bryan D. Paulsen, Scott P. White, Yanfei Wu, Elizabeth A. Jackson, Bradley S. Slowinski, C. Daniel Frisbie, and Marc A. Hillmyer. An ADMET Route to Low-Band-Gap Poly(3-hexadecylthienylene vinylene): A Systematic Study of Molecular Weight on Photovoltaic Performance. *Macromolecules*, 45(5):2190–2199, 2012.

[93] Yen-Ju Cheng, Sheng-Hsiung Yang, and Chain-Shu Hsu. Synthesis of Conjugated Polymers for Organic Solar Cell Applications. *Chem. Rev. (Washington, DC, U. S.)*, 109(11):5868–5923, 2009.

[94] Jia Du, Andria Fortney, Katherine E. Washington, Chandima Bulumulla, Peishen Huang, Dushanthi Dissanayake, Michael C. Biewer, Tomasz Kowalewski, and Mihaela C. Stefan. Systematic Investigation of Benzodithiophene-Benzothiadiazole Isomers for Organic Photovoltaics. *ACS Applied Materials & Interfaces*, 8(48):33025–33033, 2016.

[95] Antoine Mirloup, Nicolas Leclerc, Sandra Rihn, Thomas Bura, Rony Bechara, Anne Hebraud, Patrick Leveque, Thomas Heiser, and Raymond Ziessel. A deep-purple-grey thiophene-benzothiadiazole-thiophene BODIPY dye for solution-processed solar cells. *New J. Chem.*, 6(Scheme 1):3644–3653, 2014.

[96] Jianing Pei, Shanpeng Wen, Yinhua Zhou, Qingfeng Dong, and Zhaoyang Liu. A low band gap donor acceptor copolymer containing fluorene and benzothiadiazole units : synthesis and photovoltaic properties. *New Journal of Chemistry*, 35:385–393, 2011.

[97] Abdulaziz a. B. Alghamdi, Darren C. Watters, Hunan Yi, Solyman Al-Faifi, Mohammed S. Almeataq, David Coles, James Kingsley, David G. Lidzey, and Ahmed Iraqi. Selenophene vs. thiophene in benzothiadiazole-based low energy gap donoracceptor polymers for photovoltaic applications. *Journal of Materials Chemistry A*, 1(16):5165, 2013.

[98] Adam P. Smith, Rachel R. Smith, Barney E. Taylor, and Michael F. Durstock. An Investigation of Poly(thienylene vinylene) in Organic Photovoltaic Devices. *Chemistry of Materials*, 16(23):4687–4692, 2004.

[99] Youjun He, Guangjin Zhao, Jie Min, Maojie Zhang, and Yongfang Li. Poly(thienylene-benzothiadiazole-thienylene-vinylene): A narrow bandgap polymer with broad absorption from visible to infrared region. *Polymer*, 50(21):5055–5058, oct 2009.

[100] Prashant Sonar, Evan L. Williams, Samarendra P. Singh, and Ananth Dodabalapur. Thiophenebenzothiadiazolethiophene (DAD) based polymers: effect of donor/acceptor moieties adjacent to DAD segment on photophysical and photovoltaic properties. *Journal of Materials Chemistry*, 21(28):10532–10541, 2011.

[101] Paul E. Shaw, Arvydas Ruseckas, and Ifor D. W. Samuel. Exciton Diffusion Measurements in Poly(3-hexylthiophene). *Advanced Materials*, 20(18):3516–3520, jul 2008.

[102] Paul C. Hiemenz and Timothy P. Lodge. *Polymer Chemistry*. CRC Press, 2nd edition, 2007.

[103] Andrew J. Musser, Mohammed Al-Hashimi, Margherita Maiuri, Daniele Brida, Martin Heeney, Giulio Cerullo, Richard H. Friend, and Jenny Clark. Activated Singlet

Exciton Fission in a Semiconducting Polymer. *Journal of the American Chemical Society*, 135:12747–12754, 2013.

[104] E. Olejnik, B. Pandit, T. Basel, E. Lafalce, C. Sheng, C. Zhang, X. Jiang, and Z. V. Vardeny. Ultrafast optical studies of ordered poly (3-thienylene-vinylene) films. *Physical Review B*, 85:235201, 2012.

[105] A. V. Gavrilenko, T. D. Matos, C. E. Bonner, S.-S. Sun, C. Zhang, and V. I. Gavrilenko. Optical Absorption of Poly(thienylene vinylene)-Conjugated Polymers: Experiment and First Principle Theory. *The Journal of Physical Chemistry C*, 112:7908–7912, 2008.

[106] Cheng Zhang, Jianyuan Sun, Rui Li, Sam-Shajing Sun, Evan Lafalce, and Xiaomei Jiang. Poly(3-dodecylthienylenevinylene)s: Regioregularity and Crystallinity. *Macromolecules*, 44(16):6389–6396, 2011.

[107] Shehzad Jeeva, Olena Lukoyanova, Athan Karas, Afshin Dadvand, Federico Rosei, and Dmitrii F. Perepichka. Highly Emissive and Electrochemically Stable Thienylene Vinylene Oligomers and Copolymers: An Unusual Effect of Alkylsulfanyl Substituents. *Advanced Functional Materials*, 20(10):1661–1669, may 2010.

[108] Graham Williams and David C. Watts. Non-Symmetrical Dielectric Relaxation Behaviour Arising From a Simple Empirical Decay Function. *Transactions of the Faraday Society*, 66(1):80–85, 1970.

[109] J.C. Phillips. Stretched exponential relaxation in molecular and electronic glasses. *Reports on Progress in Physics*, 59(9):1133–1207, 1996.

[110] Roger C. Welch, John R. Smith, Marcel Potuzak, Xiaoju Guo, Bradley F. Bowden, T. J. Kiczenski, Douglas C. Allan, Ellyn A. King, Adam J. Ellison, and John C. Mauro. Dynamics of Glass Relaxation at Room Temperature. *Physical Review Letters*, 110(26):265901, 2013.

[111] George D. J. Phillies and Pavel Peczak. The Ubiquity of Stretched-Exponential Forms in Polymer Dynamics. *Macromolecules*, 21(1):214–220, 1988.

[112] Reuven Chen. Apparent stretched-exponential luminescence decay in crystalline solids. *Journal of Luminescence*, 102-103:510–518, may 2003.

[113] K. C. Benny Lee, J. Siegel, S. E. Webb, S. Lévêque-Fort, M. J. Cole, R. Jones, K. Dowling, M. J. Lever, and P. M. French. Application of the Stretched Exponential Function to Fluorescence Lifetime Imaging. *Biophysical Journal*, 81(3):1265–1274, 2001.

[114] Mário N. Berberan-Santos. A luminescence decay function encompassing the stretched exponential and the compressed hyperbola. *Chemical Physics Letters*, 460(1-3):146–150, jul 2008.

[115] D.L. Huber. Two-state model for sub-exponential fluorescence. *Journal of Luminescence*, 86:95–99, 2000.

[116] M. Nisoli, A. Cybo-Ottone, S. De Silvestri, V. Magni, R. Tubino, C. Botta, and A. Musco. Femtosecond transient absorption saturation in poly(alkyl-thiophene-vinylene)s. *Physical Review B*, 47(16):881–884, 1993.

[117] J. Trzmiel, K. Weron, J. Janczura, and E. Placzek-Popko. Properties of the relaxation time distribution underlying the Kohlrausch-Williams-Watts photoionization of the DX centers in Cd(1-x)Mn(x)Te mixed crystals. *Journal of Physics: Condensed Matter*, 21(34):345801, 2009.

[118] C. P. Lindsey and G. D. Patterson. Detailed comparison of the WilliamsWatts and ColeDavidson functions. *The Journal of Chemical Physics*, 73(7):3348–3357, 1980.

[119] Richard S. Lepkowicz, Claudiu M. Cirloganu, Olga V. Przhonska, David J. Hagan, Eric W. Van Stryland, Mikhail V. Bondar, Yuriy L. Slominsky, Alexei D. Kachkovski, and Elena I. Mayboroda. Absorption anisotropy studies of polymethine dyes. *Chemical Physics*, 306(1-3):171–183, 2004.

[120] Bradley Keller, Alan McLean, Bong-Gi Kim, Kyeongwoon Chung, Jinsang Kim, and Theodore Goodson. Ultrafast Spectroscopic Study of DonorAcceptor Benzodithiophene Light Harvesting Organic Conjugated Polymers. *The Journal of Physical Chemistry C*, page acs.jpcc.6b01727, 2016.

[121] Natalie Banerji, Sarah Cowan, Eric Vauthey, and Alan J Heeger. Ultrafast Relaxation of the Poly (3-hexylthiophene) Emission Spectrum. *The Journal of Physical*

Chemistry C, 115(19):9726–9739, 2011.

[122] A. Ruseckas, P. Wood, I. D. W. Samuel, G. R. Webster, W. J. Mitchell, P. L. Burn, and V. Sundström. Ultrafast depolarization of the fluorescence in a conjugated polymer. *Physical Review B*, 72(11):115214, sep 2005.

[123] Mitsuhiro Ikuta, Yoshiharu Yuasa, Tatsumi Kimura, Hiroo Matsuda, and Takayoshi Kobayashi. Phase analysis of vibrational wave packets in the ground and excited states in polydiacetylene. *Physical Review B*, 70(21):214301, 2004.

[124] Andrew T. Healy, Bryan W. Boudouris, C. Daniel Frisbie, Marc A. Hillmyer, and David A. Blank. Intramolecular exciton diffusion in poly(3-hexylthiophene). *Journal of Physical Chemistry Letters*, 4(20):3445–3449, 2013.

[125] Erik Busby, Jianlong Xia, Qin Wu, Jonathan Z Low, Rui Song, John R Miller, X-y Zhu, Luis M Campos, and Matthew Y Sfeir. A design strategy for intramolecular singlet fission mediated by charge-transfer states in donor-acceptor organic materials. *Nature Materials*, 14(4):426–33, 2015.

[126] Franziska Fennel and Stefan Lochbrunner. Exciton-exciton annihilation in a disordered molecular system by direct and multistep Förster transfer. *Physical Review B*, 92(14):140301, 2015.

[127] Ying-Zhong Ma, Kai Xiao, and Robert W. Shaw. Exciton-Exciton Annihilation in

Copper-phthalocyanine Single-Crystal Nanowires. *The Journal of Physical Chemistry C*, 116:21588–21593, 2012.

[128] Jorge Piris, Tieneke E. Dykstra, Artem A. Bakulin, Paul H. M. van Loosdrecht, Walter Knulst, M. Tuan Trinh, Juleon M. Schins, and Laurens D. A. Siebbeles. Photogeneration and Ultrafast Dynamics of Excitons and Charges in P3HT/PCBM Blends. *The Journal of Physical Chemistry C*, 113(32):14500–14506, 2009.

[129] S. Matthew Menke, Wade A. Luhman, and Russell J. Holmes. Tailored exciton diffusion in organic photovoltaic cells for enhanced power conversion efficiency. *Nature Materials*, 12(2):152–157, 2013.

[130] Jonathan a. Hinke, Tom J. Pundsack, Wade a. Luhman, Russell J. Holmes, and David a. Blank. Communication: Trapping upconverted energy in neat platinum porphyrin films via an unexpected fusion mechanism. *Journal of Chemical Physics*, 139(10), 2013.

[131] Sebastian Albert-Seifried and Richard H. Friend. Measurement of thermal modulation of optical absorption in pump-probe spectroscopy of semiconducting polymers. *Applied Physics Letters*, 98(22):98–101, 2011.

[132] Paul Heremans, David Cheyns, and Barry P. Rand. Strategies for increasing the efficiency of heterojunction organic solar cells: material selection and device architecture. *Accounts of Chemical Research*, 42(11):1740–1747, 2009.

[133] Zhicai He, Chengmei Zhong, Shijian Su, Miao Xu, Hongbin Wu, Yong Cao, Aung Ko Ko AKK Kyaw, DH Dong Hwan Wang, Vinay Gupta, Jie Zhang, Suresh Chand, Guillermo C Bazan, and Alan J Heeger. Enhanced power-conversion efficiency in polymer solar cells using an inverted device structure. *Nature Photonics*, 25(17):593–597, 2013.

[134] Weiran Cao and Jiangeng Xue. Recent progress in organic photovoltaics: device architecture and optical design. *Energy & Environmental Science*, 7(7):2123–2144, 2014.

[135] Hyojung Cha, Dae Sung Chung, Suk Young Bae, Min Jung Lee, Tae Kyu An, Jihun Hwang, Kyung Hwan Kim, Yun Hi Kim, Dong Hoon Choi, and Chan Eon Park. Complementary absorbing star-shaped small molecules for the preparation of ternary cascade energy structures in organic photovoltaic cells. *Advanced Functional Materials*, 23(12):1556–1565, 2013.

[136] Chris Groves. Suppression of geminate charge recombination in organic photovoltaic devices with a cascaded energy heterojunction. *Energy & Environmental Science*, 6(5):1546, 2013.

[137] M. C. Chen, D. J. Liaw, Y. C. Huang, H. Y. Wu, and Y. Tai. Improving the efficiency of organic solar cell with a novel ambipolar polymer to form ternary cascade structure. *Solar Energy Materials and Solar Cells*, 95(9):2621–2627, 2011.

[138] Kjell Cnops, Barry P. Rand, David Cheyns, and Paul Heremans. Enhanced photocurrent and open-circuit voltage in a 3-layer cascade organic solar cell. *Applied Physics Letters*, 101(14):1–5, 2012.

[139] Adam Barito, Matthew E. Sykes, Bingyuan Huang, David Bilby, Bradley Frieberg, Jinsang Kim, Peter F. Green, and Max Shtein. Universal design principles for cascade heterojunction solar cells with high fill factors and internal quantum efficiencies approaching 100%. *Advanced Energy Materials*, 4(13):1–10, 2014.

[140] Kjell Cnops, Barry P. Rand, David Cheyns, Bregt Verreet, Max A. Empl, and Paul Heremans. 8.4% efficient fullerene-free organic solar cells exploiting long-range exciton energy transfer. *Nature Communications*, 5:3406, jan 2014.

[141] Musubu Ichikawa, Daiki Takekawa, Hyeon-Gu Jeon, and Gilles D R Banoukepa. Cascade-type excitation energy relay in organic thin-film solar cells. *Organic Electronics*, 14(3):814–820, 2013.

[142] Olga L. Griffith and Stephen R. Forrest. Exciton management in organic photovoltaic multidonor energy cascades. *Nano Letters*, 14(5):2353–2358, 2014.

[143] C W Schlenker, V S Barlier, S W Chin, M T Whited, R E McAnally, S R Forrest, and M E Thompson. Cascade Organic Solar Cells. *Chemistry of Materials*, 23:4132–4140, 2011.

[144] S. Matthew Menke and Russell J. Holmes. Energy-cascade organic photovoltaic devices incorporating a host-guest architecture. *ACS Applied Materials and Interfaces*, 7(4):2912–2918, 2015.

[145] Santi Nonell, Noemí Rubio, Belén del Rey, and Tomás Torres. Synthesis, optical absorption and photophysical properties of cone-shaped subnaphthalocyanine. *Journal of the Chemical Society, Perkin Transactions 2*, (6):1091–1094, 2000.

[146] Bregt Verreet, Sarah Schols, David Cheyns, Barry P. Rand, Hans Gommans, Tom Aernouts, Paul Heremans, and Jan Genoe. The characterization of chloroboron (iii) subnaphthalocyanine thin films and their application as a donor material for organic solar cells. *Journal of Materials Chemistry*, 19(30):5295–5297, 2009.

[147] Biwu Ma, Claire H Woo, Yoshikazu Miyamoto, and Jean M J Fre. Solution Processing of a Small Molecule, Subnaphthalocyanine, for Efficient Organic Photovoltaic Cells. *Chem. Mater.*, (10):1413–1417, 2009.

[148] Guo Chen, Hisahiro Sasabe, Takeshi Sano, Xiao-Feng Wang, Ziruo Hong, Junji Kido, and Yang Yang. Chloroboron (III) subnaphthalocyanine as an electron donor in bulk heterojunction photovoltaic cells. *Nanotechnology*, 24(48):484007, dec 2013.

[149] C. Rimington. Spectral-Absorption Coefficients of some Porphyrins in the Soret-Band Region. *The Biochemical Journal*, 75(1955):620–623, 1960.

[150] Nagao Kobayashi and Takeo Ishizaki. Synthesis, Spectroscopy, and Molecular Orbital Calculations of Subazaporphyrins, Subphthalocyanines, Subnaphthalocyanines, and Compounds Derived Therefrom. *Journal of the American Chemical Society*, 121:9096–9110, 1999.

[151] Christian G. Claessens, David González-Rodríguez, M. Salomé Rodríguez-Morgade, Anaïs Medina, and Tomás Torres. Subphthalocyanines, subporphyrazines, and subporphyrins: singular nonplanar aromatic systems. *Chemical Reviews*, 114(4):2192–2277, feb 2014.

[152] V Bulović, R Deshpande, M.E Thompson, and S.R Forrest. Tuning the color emission of thin film molecular organic light emitting devices by the solid state solvation effect. *Chemical Physics Letters*, 308(3-4):317–322, 1999.

[153] Conor F Madigan and Vladimir Bulović. Solid state solvation in amorphous organic thin films. *Physical Review Letters*, 91(24):247403, 2003.

[154] Jeremy D. Dang, David S. Josey, Alan J. Lough, Yiying Li, Alaa Sifate, Zheng-Hong Lu, and Timothy P. Bender. The mixed alloyed chemical composition of chloro-(chloro)n-boron subnaphthalocyanines dictates their physical properties and performance in organic photovoltaic devices. *Journal of Materials Chemistry A*, 4(24):9566–9577, 2016.

[155] Hannah M. Rhoda, Mathew P. Kayser, Yefeng Wang, Alexander Y. Nazarenko, Rodion V. Belosludov, Paul Kiprof, David A. Blank, and Victor N. Nemykin. Tuning Up an Electronic Structure of the Subphthalocyanine Derivatives toward Electron-Transfer Process in Noncovalent Complexes with C60 and C70 Fullerenes: Experimental and Theoretical Studies. *Inorganic Chemistry*, 55(19):9549–9563, 2016.

[156] Herbert van Amerongen, Leonas Valkunas, and Rienk van Grondelle. *Photosynthetic Excitons*. World Scientific, 2000.

[157] A. K. Sheridan, A. R. Buckley, A. M. Fox, A. Bacher, D. D C Bradley, and I. D W Samuel. Efficient energy transfer in organic thin films - Implications for organic lasers. *Journal of Applied Physics*, 92(11):6367–6371, 2002.

[158] Jorge Bañuelos. BODIPY Dye, the Most Versatile Fluorophore Ever? *The Chemical Record*, 16(1):335–348, 2016.

[159] Aurore Loudet and Kevin Burgess. BODIPY Dyes and Their Derivatives: Syntheses and Spectroscopic Properties. *Chemical Reviews*, 107(11):4891–4932, 2007.

[160] Raymond Ziessel, Gilles Ulrich, and Anthony Harriman. The chemistry of Bodipy: A new El Dorado for fluorescence tools. *New Journal of Chemistry*, 31(4):496–501, 2007.

[161] Hiroshi Imahori, Hiroyuki Norieda, Hiroko Yamada, Yoshinobu Nishimura, Iwao Yamazaki, Yoshiteru Sakata, and Shunichi Fukuzumi. Light-Harvesting and Photocurrent Generation by Gold Electrodes Modified with Mixed Self-Assembled Monolayers of Boron - Dipyrrin and Ferrocene - Porphyrin - Fullerene Triad. *Journal of the American Chemical Society*, 123:100–110, 2001.

[162] Safacan Kolemen, Yusuf Cakmak, Sule Erten-Ela, Yigit Altay, Johannes Brendel, Mukundan Thelakkat, and Engin U. Akkaya. Solid-state dye-sensitized solar cells using red and near-IR absorbing bodipy sensitizers. *Organic Letters*, 12(17):3812–3815, 2010.

[163] Mao Mao, Xiao Lin Zhang, Xia Qin Fang, Gua Hua Wu, Yong Ding, Xiu Lin Liu, Song Yuan Dai, and Qin Hua Song. 2,6-Conjugated Bodipy sensitizers for high-performance dye-sensitized solar cells. *Organic Electronics: physics, materials, applications*, 15(9):2079–2090, 2014.

[164] Samantha J. Dammer, Pavlo V. Solntsev, Jared R. Sabin, and Victor N. Nemykin. Synthesis, characterization, and electron-transfer processes in indium ferrocenyl-containing porphyrins and their fullerene adducts. *Inorganic Chemistry*, 52(16):9496–9510, 2013.

[165] Seenichamy Jeyaprakash Narayanan, Sundararaman Venkatraman, Suhash Ranjan Dey, Bashyam Sridevi, Venkataramana Rao G Anand, and Tavarekere K Chandrashekar. Synthesis of meso ferrocenyl porphyrins. *Synlett*, 2000(12):1834–1836, 2000.

[166] Minoru Kubo, Yukie Mori, Masana Otani, Masataka Murakami, Yukihide Ishibashi, Masakazu Yasuda, Kohei Hosomizu, Hiroshi Miyasaka, Hiroshi Imahori, and Satoru Nakashima. Ultrafast Photoinduced Electron Transfer in Directly Linked PorphyrinFerrocene Dyads. *The Journal of Physical Chemistry A*, 111(24):5136–5143, 2007.

[167] Bregt Verreet, Barry P. Rand, David Cheyns, Afshin Hadipour, Tom Aernouts, Paul Heremans, Anaïs Medina, Christian G. Claessens, and Tomas Torres. A 4% efficient organic solar cell using a fluorinated fused subphthalocyanine dimer as an electron acceptor. *Advanced Energy Materials*, 1(4):565–568, 2011.

[168] O. Galangau, I. Fabre-Francke, S. Munteanu, C. Dumas-Verdes, G. Clavier, R. Méallet-Renault, R. B. Pansu, F. Hartl, and F. Miomandre. Electrochromic and electrofluorochromic properties of a new boron dipyrromethene-ferrocene conjugate. *Electrochimica Acta*, 87:809–815, 2013.

[169] Xiaodong Yin, Yongjun Li, Yulan Zhu, Xiao Jing, Yuliang Li, and Daoben Zhu. A highly sensitive viscosity probe based on ferrocene-BODIPY dyads. *Dalton transactions (Cambridge, England : 2003)*, 39(41):9929–9935, 2010.

[170] Tamanna K. Khan, Raghuvir R.S. Pissurlenkar, Mushtaque S. Shaikh, and M. Ravikanth. Synthesis and studies of covalently linked meso-furyl boron-dipyrromethene-ferrocene conjugates. *Journal of Organometallic Chemistry*, 697(1):65–73, 2012.

[171] Yuriy V. Zatsikha, Eranda Maligaspe, Anatolii A. Purchel, Natalia O. Didukh, Yefeng

Wang, Yuriy P. Kovtun, David A. Blank, and Victor N. Nemykin. Tuning Electronic Structure, Redox, and Photophysical Properties in Asymmetric NIR-Absorbing Organometallic BODIPYs. *Inorganic Chemistry*, 54(16):7915–7928, 2015.

[172] Keisuke Matsumoto, Mamoru Fujitsuka, Tadatake Sato, Shinji Onodera, and Osamu Ito. Photoinduced Electron Transfer from Oligothiophenes / Polythiophene to Fullerenes (C 60 / C 70) in Solution : Comprehensive Study by Nanosecond Laser Flash Photolysis Method. *Journal of Physical Chemistry B*, 104:11632–11638, 2000.

[173] Chandra B. Kc, Gary N. Lim, Paul A. Karr, and Francis D'Souza. Supramolecular tetrad featuring covalently linked bis(porphyrin)- phthalocyanine coordinated to fullerene: Construction and photochemical studies. *Chemistry - A European Journal*, 20(25):7725–7735, 2014.

[174] B. K C Chandra and Francis D'Souza. Design and photochemical study of supramolecular donor-acceptor systems assembled via metal-ligand axial coordination. *Coordination Chemistry Reviews*, 322:104–141, 2016.

[175] Venugopal Bandi, Mohamed E. El-Khouly, Kei Ohkubo, Vladimir N. Nesterov, Melvin E. Zandler, Shunichi Fukuzumi, and Francis D'Souza. Excitation-wavelength-dependent, ultrafast photoinduced electron transfer in bisferrocene/BF2-chelated-azadipyrromethene/fullerene tetrads. *Chemistry - A European Journal*, 19(22):7221–7230, 2013.

[176] Venugopal Bandi, Mohamed E. El-Khouly, Vladimir N. Nesterov, Paul A. Karr, Shunichi Fukuzumi, and Francis D'Souza. Self-assembled via metal-ligand coordination AzaBODIPY-zinc phthalocyanine and AzaBODIPY-zinc naphthalocyanine conjugates: Synthesis, structure, and photoinduced electron transfer. *Journal of Physical Chemistry C*, 117(11):5638–5649, 2013.

[177] Anamika Ray, Ajoy Bauri, and Sumanta Bhattacharya. Absorption spectrophotometric, fluorescence and quantum chemical investigations on non-covalent interaction between PC70BM and designed diporphyrin in solution. *Spectrochimica Acta - Part A: Molecular and Biomolecular Spectroscopy*, 134:566–573, 2015.

[178] Francis D'Souza, Anu N. Amin, Mohamed E. El-Khouly, Navaneetha K. Subbaiyan, Melvin E. Zandler, and Shunichi Fukuzumi. Control over photoinduced energy and electron transfer in supramolecular polyads of covalently linked azaBODIPY-bisporphyrin 'Molecular Clip' hosting fullerene. *Journal of the American Chemical Society*, 134(1):654–664, 2012.

[179] Francis D'Souza, Phillip M. Smith, Melvin E. Zandler, Amy L. McCarty, Mitsunari Itou, Yasuyaki Araki, and Osamu Ito. Energy Transfer followed by Electron Transfer in a supramolecular Triad Composed of Boron-Dipyrrin, Zinc Porphyrin and Fullerene. *Journal of the American Chemical Society*, 126:7898–7907, 2004.

[180] Francis D'Souza, Raghu Chitta, Suresh Gadde, Lisa M. Rogers, Paul A. Karr, Melvin E. Zandler, Atula S D Sandanayaka, Yasuyaki Araki, and Osamu Ito. Photosynthetic reaction center mimicry of a "special pair" dimer linked to electron acceptors by a supramolecular approach: Self-assembled cofacial zinc porphyrin dimer complexed with fullerene(s). *Chemistry - A European Journal*, 13(3):916–922, 2007.

[181] Francis D'Souza and Osamu Ito. Supramolecular donor-acceptor hybrids of porphyrins/phthalocyanines with fullerenes/carbon nanotubes: electron transfer, sensing, switching, and catalytic applications. *Chemical communications (Cambridge, England)*, (33):4913–4928, 2009.

[182] Francis D'Souza, M. A. Collini, M. J. Thomas, V. Bandi, and P. A. Karr. Directly Attached Bisdonor-BF2 Chelated Azadipyrromethene-Fullerene Tetrads for Promoting Ground and Excited State Charge Transfer. *Chemistry - A European Journal*, 2017.

[183] Guilford Jones II, William R. Jackson, and Arthur M. Halpern. Medium effects on fluorescence quantum yields and lifetimes for coumarin laser dyes. *Chemical Physics Letters*, 72(2):391–395, 1980.

[184] C. A. Parker and W. J. Barnes. Some Experiments with Spectrofluorimeters and Filter Fluorimeters. *The Analyst*, 82(978):606–618, 1957.

[185] Alexander V. Fonin, Anna I. Sulatskaya, Irina M. Kuznetsova, and Konstantin K.

Turoverov. Fluorescence of dyes in solutions with high absorbance. Inner filter effect correction. *PLoS ONE*, 9(7), 2014.

[186] Iouri E. Borissevitch. More about the inner filter effect: Corrections of Stern-Volmer fluorescence quenching constants are necessary at very low optical absorption of the quencher. *Journal of Luminescence*, 81(3):219–224, 1999.

[187] Suzanne Fery-Forgues and Dominique Lavabre. Are Fluorescence Quantum Yields So Tricky to Measure? A Demonstration Using Familiar Stationery Products. *Journal of Chemical Education*, 76(9):1260, 1999.

[188] Hans-Peter Lutz and Pier Luigi Luisi. Correction for Inner Filter Effects in Fluorescence Spectroscopy. *Helvetica Chimica Acta*, 66(7):1929–1935, 1983.

[189] Nam Sun Wang and Michael B. Simmons. Fluorescence modeling in a multicomponent system. *Biotechnology and Bioengineering*, 38(8):907–922, 1991.

[190] Mikael Kubista, Robert Sjoeback, Svante Eriksson, and Bo Albinsson. Experimental correction for the inner-filter effect in fluorescence spectra. *The Analyst*, 119(3):417, 1994, PN26895.

[191] Tobias Larsson, Margareta Wedborg, and David Turner. Correction of inner-filter effect in fluorescence excitation-emission matrix spectrometry using Raman scatter. *Analytica Chimica Acta*, 583(2):357–363, 2007.

[192] Richard A Leese and E L Wehry. Corrections for inner-filter effects in fluorescence quenching measurements via right-angle and front-surface illumination. *Analytical Chemistry*, 50(8):1193–1197, 1978.

[193] Sheryl A. Tucker, Vicki L. Amszi, and William E. Acree. Primary and secondary inner filtering. Effect of K2Cr2O7 on fluorescence emission intensities of quinine sulfate. *J. Chem. Educ.*, 69(1):A8, 1992.

[194] Thomas D Gauthier, Edward C Sham, Wllllam F Guerln, W Rudolf Seltz, and Clarence L Grant. Fluorescence Quenching Method for Determining Equilibrium Constants for Polycyclic Aromatic Hydrocarbons Binding to Dissolved Humic Materialst. *Environmental Science & Technology*, 20(11):1162–1166, 1986.

[195] Ana Mendonça, Ana C. Rocha, Armando C. Duarte, and Eduarda B H Santos. The inner filter effects and their correction in fluorescence spectra of salt marsh humic matter. *Analytica Chimica Acta*, 788:99–107, 2013.

[196] Marina L. Mertens and Jeremias H R Kägi. A graphical correction procedure for inner filter effect in fluorescence quenching titrations. *Analytical Biochemistry*, 96(2):448–455, 1979.

[197] Alberto Credi and Luca Prodi. From observed to corrected luminescence intensity

of solution systems: an easy-to-apply correction method for standard spectrofluorimeters. *Spectrochimica Acta Part A: Molecular and Biomolecular Spectroscopy*, 54(1):159–170, 1998.

[198] C. A. Parker and W. T. Rees. Correction of fluorescence spectra and measurement of fluorescence quantum efficiency. *The Analyst*, 85(1013):587, 1960.

[199] Berry Birdsall, Rodney W. King, Miriam R. Wheeler, Charles A. Lewis, Scott R. Goode, R. Bruce Dunlap, and Gordon C K Roberts. Correction for light absorption in fluorescence studies of protein-ligand interactions. *Analytical Biochemistry*, 132(2):353–361, 1983.

[200] M. M. Puchalski, M. J. Morra, and R. von Wandruszka. Assessment of inner filter effect corrections in fluorimetry. *Fresenius' Journal of Analytical Chemistry*, 340(6):341–344, 1991.

Appendix A

Coding Examples

This appendix contains examples of code used throughout this thesis. MATLAB code is presented in plain-text.

A.1 Distributions from Inverse Laplace Transform

This section contains the code which was used to generate the rate distribution functions $g(k)$ in the semiconducting polymers.

```
%%
xmin=0.0001;
xmax=10;
```

```
taunum=200000;

a=6; ns=20; nd=19;

beta=[0.73 0.46 0.43 0.41 0.44 0.34];

taus=[1.42 1.84 5.89 8.87 16.2 1.54];

figure();

for i=1:length(beta)

    [x1,ft1]=INVLAP(['exp(-' num2str((1/taus(i).^(beta(i)))) '*s^'...

         num2str(beta(i)) ')'],xmin,xmax,taunum,a,ns,nd);

    A{i}=[x1',ft1'];

    temp=A{i};

    %temp(:,1)=temp(:,1)./taus(i);

    %temp(:,2)=taus(i).*temp(:,2);

    m=max(temp(:,2));

    temp(:,2)=temp(:,2)/m;

    B{i}=temp;

    tempplot=plot(temp(:,1),temp(:,2));

    set(tempplot,'color',WhatColor(length(beta)+1,i+1)); hold on;

end

leg=legend('5','21','37','59','78','100','Location','best');


% INVLAP  Numerical Inversion of Laplace Transforms
```

```
function [radt,ft]=INVLAP(Fs,tini,tend,nnt,a,ns,nd);
% Fs is formula for F(s) as a string
% tini, tend are limits of the solution interval
% nnt is total number of time instants
% a, ns, nd are parameters of the method
% if not given, the method uses implicit values a=6, ns=20, nd=19
% it is recommended to preserve a=6
% increasing ns and nd leads to lower error
% an example of function calling
% [t,ft]=INVLAP('s/(s^2+4*pi^2)',0,10,1001);
% to plot the graph of results write plot(t,ft), grid on, zoom on
FF=strrep(strrep(strrep(Fs,'*','.*'),'/','./'),'^','.^');
if nargin==4
  a=6; ns=20; nd=19;  end;    % implicit parameters
radt=linspace(tini,tend,nnt); % time vector
if tini==0  radt=radt(2:1:nnt);  end;  % t=0 is not allowed
tic % measure the CPU time
for n=1:ns+1+nd               % prepare necessary coefficients
   alfa(n)=a+(n-1)*pi*j;
   beta(n)=-exp(a)*(-1)^n;
end;
```

```
n=1:nd;

bdif=fliplr(cumsum(gamma(nd+1)./gamma(nd+2-n)./gamma(n)))./2^nd;

beta(ns+2:ns+1+nd)=beta(ns+2:ns+1+nd).*bdif;

beta(1)=beta(1)/2;

for kt=1:nnt                  % cycle for time t

   tt=radt(kt);

   s=alfa/tt;                 % complex frequency s

   bt=beta/tt;

   btF=bt.*eval(FF);          % functional value F(s)

   ft(kt)=sum(real(btF));     % original f(tt)

end;

toc
```

A.2 Fitting Full Frequency Spectra with Linear Combination

This section contains the code that performed the spectral deconvolutions on the SubPc Pump Probe spectra in order to removal the thermal component. The code consists of three scripts necessary to perform the fitting. The first, fflincombmacro.m, loads up the raw data and input spectra to be used as components for the fits. It is generally the only script that needs to be edited. The second, fflincombopt.m, is the function that actually runs the optimization for each time point. The third, fflincombresid.m, contains the code for calculating the residual for each step in the optimization.

```
% Linear combination of full frequency spectra. This macro is used in
% conjuction with the functions fflincombopt and fflincombresid.


%% Start Inputs


% Initial guess for the weighting coefficients.
ig = [2 2];


% Data to be fitted. A typical full frequency data set with time axis in
% first column and wavelength/eV axis in first row.
data = load('full_frequency_sample_dod.dat');
```

```
% Fitting Component file names (include .dat). These files can be either
% 1) two rows (wavelength in first row, dOD in second) or
% 2) full frequency spectra (must be the same number of
%    time points as data)
Afilename = 'componentA_spectrum_dod.dat';
Bfilename = 'componentB_spectrum_dod.dat';


% Interpolate to data? 1==yes, all else == no;
% CAUTION: This interpolates the component files onto the data file axis.
% You must ensure that the component file energy/wavelength axes range
% encompasses all of the data file energy/wavelength range or else the
% interpolation will not work.
interp_switch = 0;


%% End Inputs
%% Start Code


% Just some bookkeeping, prelim set up. Should be pretty obvious what is
% happening.
```

```
% Gets the number of time points

ntp=length(data(:,1));


%Makes sure x-axis will be in ascending order

data=sortrows(data',1)';

%Length of x-axis

ldata=length(data(1,:));


Afile=load(Afilename);

Bfile=load(Bfilename);


Aspeclength=length(Afile(:,1));

Bspeclength=length(Bfile(:,1));

AspecX=[];

BspecX=[];


% Runs through the optimization for each time point in the input file.

for i=2:ntp

    inputfile(1,:)=data(1,2:ldata);

    inputfile(2,:)=data(i,2:ldata);
```

```
% This code checks if you are using time dependent components (e.g. if
% you are using a separate full frequency set as a fitting
if Aspeclength>2
    AspecX(1,:)=Afile(1,2:ldata);
    AspecX(2,:)=Afile(i,2:ldata);
else
    AspecX=Afile;
end
if Bspeclength>2
    BspecX(1,:)=Bfile(1,2:ldata);
    BspecX(2,:)=Bfile(i,2:ldata);
else
    BspecX=Bfile;
end


% This code will check if you want to interpolate your fitting
% components onto the raw data axis.
if interp_switch == 1
    Aspec(1,:)=inputfile(1,:);
    Aspec(2,:)=interp1(AspecX(1,:),AspecX(2,:),Aspec(1,:));
    Bspec(1,:)=inputfile(1,:);
```

```
        Bspec(2,:)=interp1(BspecX(1,:),BspecX(2,:),Bspec(1,:));
    else
        Aspec=AspecX;
        Bspec=BspecX;
    end

    % This code runs the optimization
    [a,b]=fflincombopt(inputfile,ig,Aspec,Bspec);

    % Puts the coefficients and residual into an array to be read later.
    WeightA(i-1,1)=data(i,1)/1000;
    WeightA(i-1,2)=a(1,1);
    WeightB(i-1,1)=data(i,1)/1000;
    WeightB(i-1,2)=a(1,2);
    resid(i-1,1)=data(i,1)/1000;
    resid(i-1,2)=b;
end

% Plots up the coefficients as a function of delay time.
scplot(WeightA,WeightB,10,-3);
scplot(resid,10,-3);
```

```
%% fflincombopt

function [igout,residout]=fflincombopt(inputfile,ig,Aspec,Bspec)


optevsfms=1000;

cfitsw=1;


options = optimset('Display','final','MaxIter',...

          optevsfms,'MaxFunEvals',optevsfms,'TolFun',1e-40,'TolX',1e-40);


[igout,residout]=fminsearch(@(x)fflincombresid(inputfile,x,0,...

                                                Aspec,Bspec),ig,options);


fflincombresid(inputfile,igout,1,Aspec,Bspec);

%% fflincombresid

%Fitting ultrafast data with two components (initial state A and final

%state B)


function resid=fflincombresid(inputfile,ig,plotswt,Aspec,Bspec);
```

```
%% Start Code

% Normalize fitting components? no=0, yes=1

normswitch = 0; %Just leave this to 0 usually


% Sort rows of input file

inputfile=sortrows(inputfile',1)';


% Set up initial guess

Aweight=ig(1);

Bweight=ig(2);


% Normalize spectral components if called for.


Aspectrum=Aspec;

if normswitch == 1

    Aspectrum(2,:)=Aspectrum(2,:)/max(abs(Aspectrum(2,:)));

end

Aspectrum=sortrows(Aspectrum')';


Bspectrum=Bspec;

if normswitch == 1
```

```
    Bspectrum(2,:)=Bspectrum(2,:)/max(abs(Bspectrum(2,:)));
end
Bspectrum=sortrows(Bspectrum')';

% Adjust components for fitting by multiplying by coefficient.
AspectrumW=Aspectrum;
AspectrumW(2,:)=Aspectrum(2,:)*Aweight;

BspectrumW=Bspectrum;
BspectrumW(2,:)=Bspectrum(2,:)*Bweight;

% Make total spectrum for fit

totalspectrum(1,:)=AspectrumW(1,:);
totalspectrum(2,:)=AspectrumW(2,:)+BspectrumW(2,:);

% Calculate residual
diff(1,:)=inputfile(1,:);
diff(2,:)=inputfile(2,:)-totalspectrum(2,:);

resid=sum(diff(2,:).^2);
```

```
% Plots up the optimized fit for each time point.
if plotswt==1
    figure(); hold on;
    plot(inputfile(1,:),inputfile(2,:));
    plot(AspectrumW(1,:),AspectrumW(2,:),':');
    plot(BspectrumW(1,:),BspectrumW(2,:),':');
    plot(totalspectrum(1,:),totalspectrum(2,:),'--');
    legend('Raw','A Component','B Component', 'Fit'); hold off;
end


end


%% End Code
```

A.3 Annihilation Model Fitting

This section contains the code used to fit transient decay data to the 3D-diffusion limited annihilation model. A similar function is used when fitting transient decay data to other functional forms, such as 1D-diffusion limited annihilation, single-step Förster-type annihilation, and others.

```
function [f t output] = annihil3Ddiff(datatemp,fitpartemp);


% Inputs


% datatemp should contain time-axis in ps in column 1

% and dOD signal in column 2

X = datatemp(:,1);

Y = datatemp(:,2);

Y = Y./max(Y);

W = 1*ones(size(Y));



ROI = [0.2 900]; % optimization region

%ROI_IDXS = [28 65];

%ROI_IDXS(1,1)=nearestvaluei(X',ROI(1,1));
```

```
%ROI_IDXS(1,2)=nearestvaluei(X',ROI(1,2));

ROI_IDXS = find(X>=ROI(1) & X<=ROI(2));


% fitpartemp is an array with the following values

 R = fitpartemp(1); % critical annihilation radius

 rho = fitpartemp(2); % molecular density

 N0 = fitpartemp(3); % initial exciton densitiy

 tau = fitpartemp(4); % unimolecular exciton lifetime

 n0 = N_0/rho;



exp1 = @(D,c,c2,x) c2+c*exp(-(1./tau)*x)./...

    (1+N0*4*pi()*R*(D.*(1E-12*tau))*(1-exp(-(1./tau)*x))+...

    N0*2^(1.5)*pi()*(R.^2)*(D.*(1E-12*tau))^(0.5)*...

        erf(((1./tau).*x).^(0.5));


exp1_UB = [1 1000 0.5];

exp1_LB = [0 0.5 0.0];

exp1_SP = [2E-3 10 0.1];
```

```
[f t output] = fit(X(ROI_IDXS),Y(ROI_IDXS),...

    exp1,...

    'Lower', exp1_LB,...

    'Upper', exp1_UB,...

    'StartPoint', exp1_SP,...

    'Weights',W(ROI_IDXS),...

    'DiffMinChange',1e-40,...

    'TolFun',1e-40,...

    'TolX',1e-40);


% Plot Results


figure

subplot(2,1,1);

hold on;

plot(X,Y,'-o')

plot(X(ROI_IDXS),exp1(f.D, f.c, f.c2, X(ROI_IDXS)), 'r--')


title(['D=' num2str(f.D) '  c=' num2str(f.c) '  c2=' num2str(f.c2)]);

subplot(2,1,2)

plot(X(ROI_IDXS),Y(ROI_IDXS)-exp1(f.D, f.c, f.c2, X(ROI_IDXS)), '-o')
```

```
f

t.rmse

end
```